Doctor Dissertation

Study on Wavy Leading Edge Phenomena
～Effect of Wing Shape and Aspect Ratio～
(波状前縁翼に関する研究
～翼形状とアスペクト比の影響～)

September, 2020

Department of Transportation and Environmental Systems
Graduate School of Engineering
Hiroshima University

Iis Rohmawati

CONTENTS

ABSTRACT i

CONTENTS iii

NOMENCLATURES v

CHAPTER 1 INTRODUCTION 1

1.1 Research Background……..……... 1

1.2 Previous Research……..…... 1

1.3 Aims and Objectives of the Research…….……... 23

1.4 Structure of the Research…..……..... 23

1.5 Summary……... 24

CHAPTER 2 METHODOLOGY AND GOVERNING EQUATION

2.1 Wing Scheme……. 25

2.2 Experimental Method…… 30

2.3 Numerical Method……. 31

2.4 Summary……... 39

CHAPTER 3 WAVY LEADING-EDGE PERFORMANCE ON THE RECTANGLE WING 41

3.1 Experimental Results……. 41

3.2 Validity with Experimental Data……... 50

3.3 Numerical Results……. 52

3.3.1 Steady Case…….. 52

3.3.2 Unsteady Case……. 53

3.4 Summary……... 73

CHAPTER 4 EFFECT OF WAVY LEADING EDGE WITH VARIOUS ASPECT RATIOS IN STEADY CASE 75

4.1 Validation with Experimental Data……... 76

4.2 Various Aspect Ratios…… 78

4.3 Effectiveness of WLE…… 80

4.4 Aspect Ratio Effect…… 88

4.5 Summary…… 94

CHAPTER 5 UNSTEADY ANALYSIS OF WAVY LEADING-EDGE EFFECT ON THE RECTANGULAR WING WITH ASPECT RATIO SERIES 95

5.1 Unsteady analysis of rectangular wings…… 95

5.2 Summary…… 104

CHAPTER 6 A COMPARISON OF RECTANGLE WING AND TAPERED WING USING WAVY LEADING EDGE 105

6.1 Validation with Experimental Data……... 105

6.2 Taper Ratio Variation in Steady Case…… 107

6.3 Unsteady Taper Ratio Analysis…….. 111

6.4 Summary…… 115

CHAPTER 7 CONCLUSION 117

REFERENCE 121

LIST OF FIGURES 127

NOMENCLATURES

α	Angle of attack
α_a	Amplitude of angles
α_c	Center of angle
λ	Wavelength
Φ	Dissipation function
δ	Distance from the wall
ρ	Density
μ	viscosity
τ_ω	Wall shear stress
ω	Rotational speed
c	Chord length
c_{root}	Root chord length
$c_{wing\text{-}tip}$	Wing tip chord length
Cl	Lift coefficient (Cl = L / (½ ρ U_0^2 s c))
Cd	Drag coefficient (Cd = D / (½ ρ U_0^2 s c))
Cp	Pressure specific heat
D	Drag force
d	Height, depth
f	Frequency (Hz)
g	Gravitational acceleration
h	Amplitude
I	Global coordinate direction
k	Reduced frequency

K	Turbulent kinetic energy
L	Lift force
p	pressure
r	Distance from the axis rotation
Re	Reynolds number
s	Span length
t	Time (s)
T_0	Non dimensional time
TI	Turbulent intensity
TR	Taper ratio
U_0	Free stream velocity (m/s)
u	Velocity in u-direction
v	Velocity in v-direction
w	Velocity in w-direction
υ	Kinematic viscosity
y^+	Layer thickness

学 位 論 文 概 要

題　目: Study on Wavy Leading Edge Phenomena ~ Effect of Wing Shape and Aspect Ratio ~

（波状前縁翼に関する研究 ～翼形状とアスペクト比の影響～）

氏　名 IIS ROHMAWATI

Learning from nature-inspired by a humpback whale flipper is capable of capturing their prey ingeniously. The humpback whale has the flipper with wavy leading edges (WLE), which has an improvement of hydrodynamic performance. This flipper plays a part in enhancing efficiency on the hydrodynamic. Their flipper morphology makes increase the hydrodynamic performance by increasing the lift force and reducing the drag one. This study focuses on the hydrodynamic performance of WLE with several wing shapes based on NACA0018: rectangular and taper wings, and their aspect ratio in steady and unsteady motions at Reynolds number 1.4 x 10^5. The main results can be summarized as follows:

1. This research employed the numerical approach using Computational Fluid Dynamics, CFD, to investigate the flow mechanism on the WLE wing. There are three types of reduced frequencies during unsteady conditions. The numerical work in unsteady conditions was conducted at aspect ratio 1.6 to find out the effect of WLE on the wing. The upstroke motion has higher hydrodynamic performance at the aspect ratio of 1.6 than the downstroke motion. The stronger vortical flow was observed during the upstroke motion concerning the streamline analysis around the WLE. This vortical flow could contribute to the separation control
2. The different aspect ratios on the rectangular wing were compared and examined to survey the maximum performance of the WLE. The steady case analysis was also investigated to determine the suitable aspect ratio of the rectangular wing with the WLE. The best performance was observed at the aspect ratio of 7.9 after the stall region with separation. The effect of the WLE is remarkable in the area between mid-span and the wing tip direction, comparing the area between the symmetry plane and the mid-span.
3. The several aspect ratios: 3.9, 5.1, and 7.9, were compared during the unsteady motion to investigate the effect of the WLE on the rectangular wing. This study focused on the range of the angles at the post-stall condition: $25° \leq \alpha \leq 35°$. The similar results with the aspect ratio of 1.6 were found at the aspect ratios of 3.9 and 5.1, where the WLE wing has the best performance. The WLE wing has a higher lift force comparing with that of the baseline wing during the upstroke motion. However, the tendency at the aspect ratio of 7.9 was inconsistent with that of AR 1.6. This difference was an important fact to observe the characteristics of the flow phenomenon caused by the WLE. Therefore, the shape of the rectangular wing was appropriately improved into the form of the taper wing because a taper wing shape could be very similar to the flipper shape of the humpback whale.
4. The humpback whale flipper has an aspect ratio of around 7.7. An approach to the design of the humpback whale flipper was rendered using the three types of taper ratios: 0.1, 0.3, and 0.5. This study in the steady motion was performed on three forms of taper ratios to find out the best performance. The position of the WLEs between mid-span and the wing tip direction has a higher effect in controlling the flow separation.
5. Both the taper wing and the rectangular one were compared to find out the optimal wing shape; The rectangular wing with the aspect ratio of 7.9 and the taper wing with the taper ratio of 0.3 were investigated in the unsteady motion with the reduced frequency $k = 0.25$ at the attach angles $25° \leq \alpha \leq 35°$ in the post-stall region. The taper wing with the WLE has a good performance in both upstroke and downstroke motions. The flow phenomena, including the separation around the WLE, are considerably different in both wings. The straight streamlines were found on the TR 0.3 wing in the mid-span to the direction of the wing tip. Because the flow filed around the taper wing with the WLE is relatively smooth than that around the rectangular wing.

CHAPTER 1
INTRODUCTION

1. 1 Research Background

Learning from nature, the humpback whales have the ingenious ability to catch their prey. Its morphology plays an important role in improving hydrodynamic performance. Their flipper has the form streamlined, blunt, and rounded leading edge. The shape of the flipper is expected to increase the lift and reduce the drag coefficient. It is interesting to be applied for various purposes, such as stabilizers on the ships, axial fans, or other aircraft. These applications could be operated with frequently facing the stall condition. Therefore, an improvement should be necessary to ensure good performance. In general, an improvement of hydrodynamic performance could be made by using the flow control device. The following sections provide a classification of flow control based on the energy expenditure of the device. If the device requires the energy to control fluid flow, it is classified as an active control. Otherwise, it is classified as a passive control. In this research, the passive control of fluid flow is the main focus.

One of the passive controls by fluid flow is using wavy leading edge by attaching it on the leading edge of the wing. As explained before, the flipper on the humpback whale flipper has an important role in improving the hydrodynamic performance. The flipper shape could be approached by using the wavy leading edge. More benefits could be obtained by using the wavy leading edge if this shape can be applied in more various wing shapes such as rectangular wing and tapered wing. This research, carried out the benefit of the wavy leading edge on both wing shapes and clarified the comparison of them.

1.2 Previous Research

The following paragraph below describes some research that is related to the fluid flow using passive control, such as adding a wavy leading edge of a wing and turbulent generator. There have been many studies inspired by the humpback whale flipper. Frank E. Fish et al. [1] stated that the morphology of the humpback whale flipper is adapted for high maneuverability associated with the whales unique feeding behavior. It has been seen that tubercles on the humpback whale flipper have functioned as passive control devices, shown in Figure 1.1. The humpback whale flipper had a cross-sectional design typical of manufactured aerodynamic foils for lift generation. Foil NACA 634-021 is similar to cross-sections from the whale flipper.

Figure 1.1 Humpback Whale with tubercles on flipper leading edge (http://oceanwideimages.com)

Another research was employed by Fish et al [2] about application of Bio-inspired technology. Experimental analysis of finite wing models has demonstrated that the presence of tubercles produces a delay in the angle of attack until stall. The tubercle on the leading edge like humpback whale flipper can produce a delay stall, increasing maximum lift and decreasing drag. Humpback whales' flipper cross section closely resembles the 21% thick, low drag, similar with NACA 634-021 airfoil. In their research [3] about engineering opportunities from nature was mentioned that there a few other passive means of altering fluid flow around a wing-like structure that can delay stall and both increase lift and reduce drag simultaneously. As result the application of leading edge tubercles for passive flow control has potential in the design of control surfaces, wings, fans and wind turbines.

On a wing, very high pressure in front of the leading edge causes a lot of drag. In that area, the leading-edge vortex stays a few moments before it expands to the suction side and pressure side. It will be separate from the wing and then stalls. It conditions abrupt decrease the lift force and increases the drag force. After stall condition, the wing unable to acquire the higher lift force. It is important to improve the stall characteristics of the wing event after the stall condition. This improvement could be applied in some practical application which has the unsteady motion such as fin stabilizer, wind turbine, or other aircraft.

There are many methods to maintain the lift force, such as using a vortex generator or wavy leading edge. Vortex generator (VG) is the small wedge placed on a wing. It has benefit in reducing separated flow and delaying the stall point as it is shown in Figure 1.2. In general, the VG could be defined as vortex devices to maintain the flow at low speeds and delay stall, by creating a vortex to re-energize the boundary layer close to the wing. But the VG creates additional drag at all speeds. Bak et al. [4] studied the VG and its benefit with wind tunnel tests

of NACA 63-415 profile. The VG is able to increase the maximum lift coefficient, but it is unable to acquire the lift coefficient after the stall condition. Besides that, the VG increases the drag coefficient for low angles of attack until 12°. Figure 1.3 represents the force characteristics for NACA 63-415 profile with adding the VGs on suction side measurements compared with the smooth flow. At the angle of attack $10° \leq \alpha \leq 20°$, the wing with VGs able to increase the lift coefficient (*Cl*), but at the angle of attack higher than 20° no significant differences with the smooth wing.

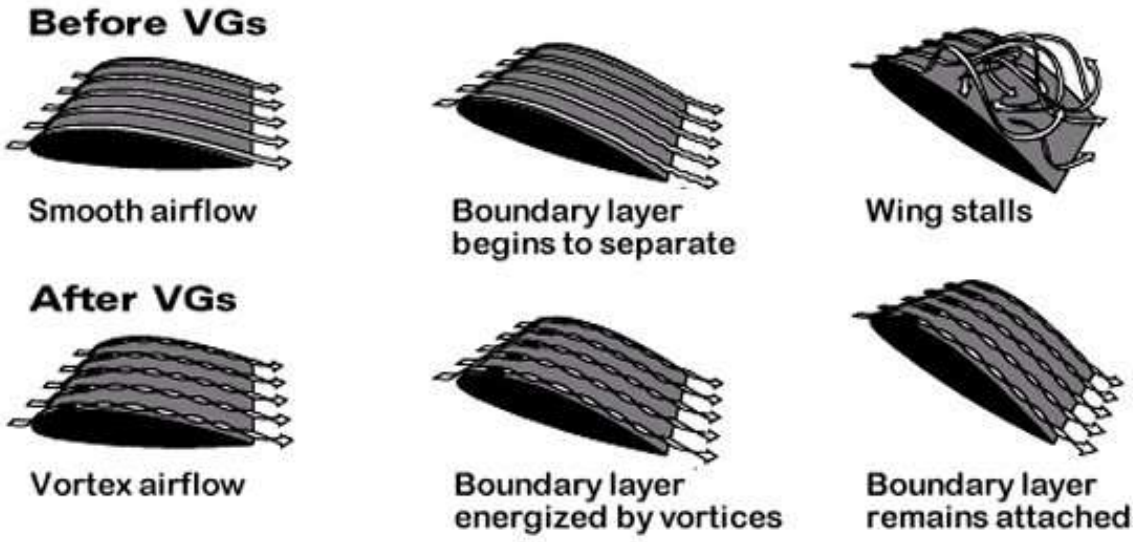

Figure 1.2 Benefits of vortex generator
(http://www.aerospaceweb.org/question/aerodynamics/q0255.shtml)

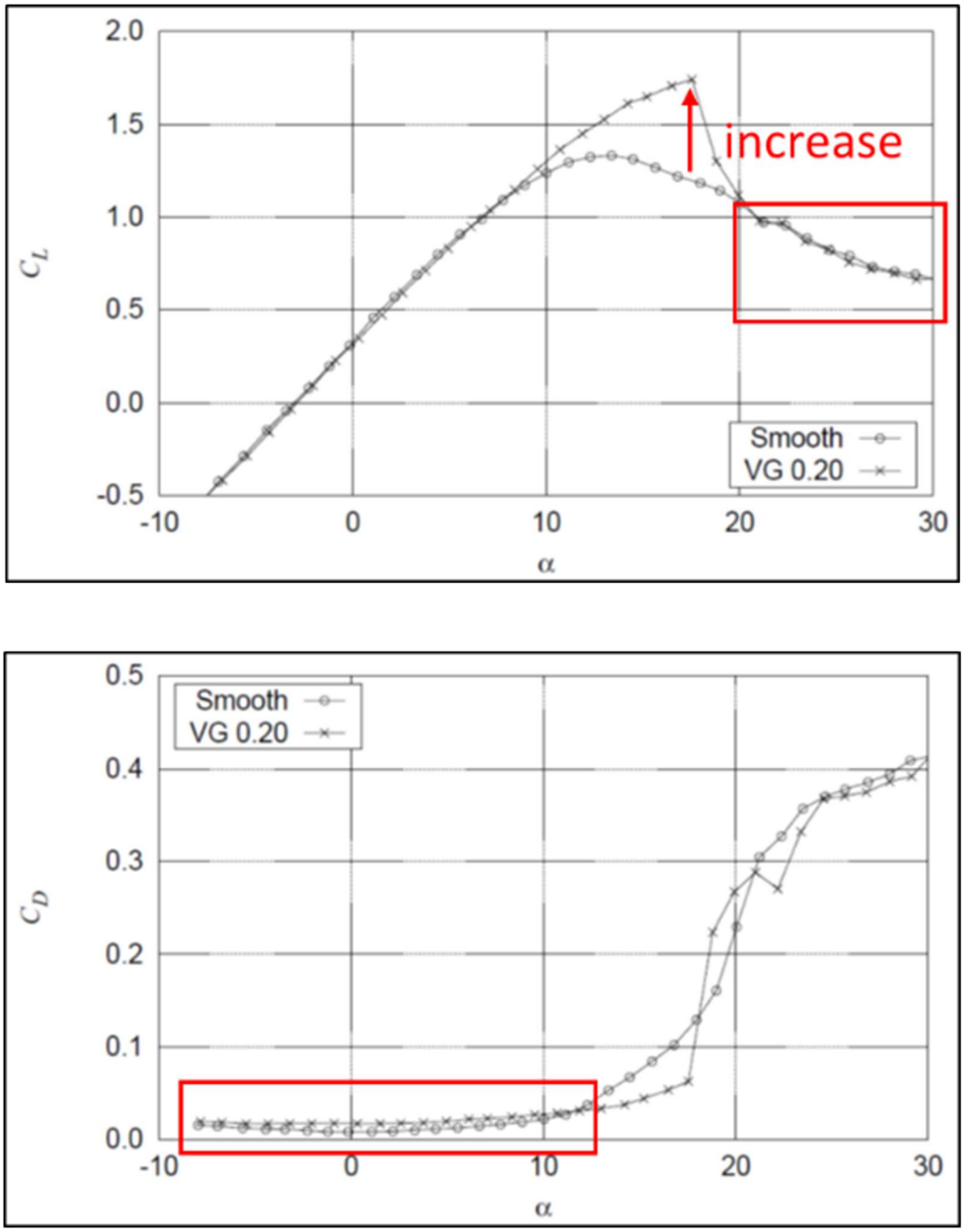

Figure 1.3 Lift coefficient (*Cl*) and drag coefficient (*Cd*) for NACA 63-415 profile with VGs on the suction side measurements [4]

a)

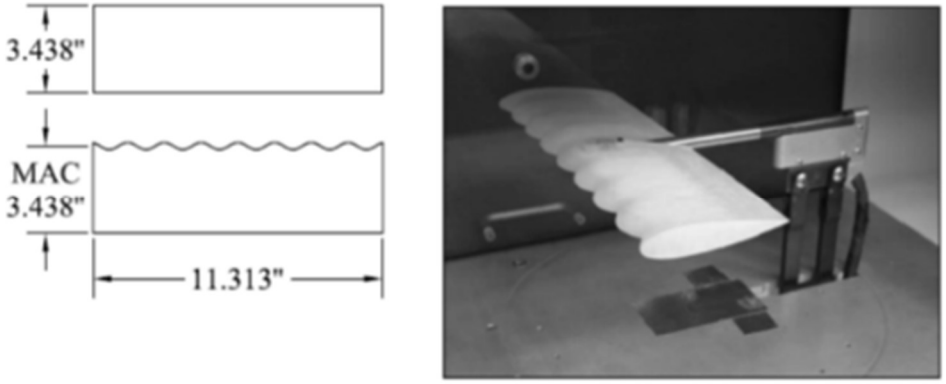

b)

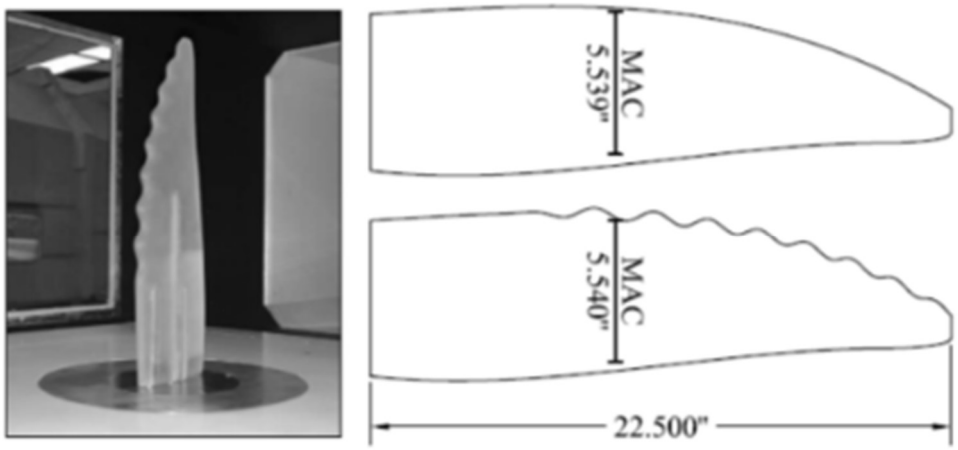

Figure 1.4 Experimental model a) Full span model, b) Semi-span model [5]

Another research conducted by Miklosovic et al. [5], [6] resulted that a scalloped flipper is able to delay stall and increase the lift force. They also stated that the humpback whale flipper could delay stall approximately 40%. The aim of their research is to determine the sectional characteristics of the wing using tubercles. Figure 1.4 represents their experimental model. Figure 1.4 a) indicates the full span model (quasi 2D) or rectangle wing with wavy leading edge and b) indicates the semi-span model or fin type model (baseline flipper) and adding the wavy leading-edge wing (scallop flipper). Their results are described in Figure 1.5. Figure 1.5 a) shows the full span model results. Before the stall condition, the scallop flipper has lower *Cl* value than the baseline flipper. But after the stall condition, the lift coefficient has higher value than the baseline. The flipper model result is shown in Figure 1.5 b), the scallop flipper has the same manner with the baseline flipper before stall condition, but it has higher maximum lift coefficient than the baseline flipper at the critical angle before the stall was occur. It means that the scallop flipper has an impressive performance to delay the stall. The scalloped flipper

showed better performance than a full span model. However, the mechanism of delaying the stall in their research is remaining unclear.

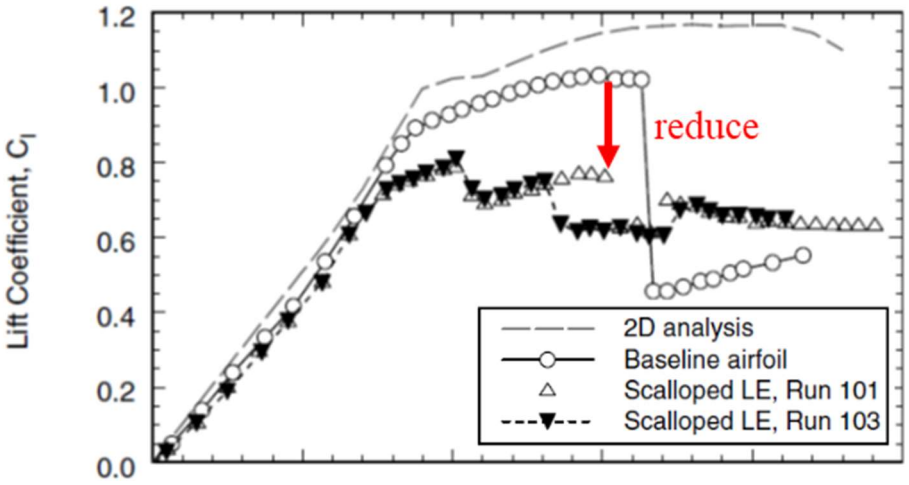

a) Full span quasi 2D

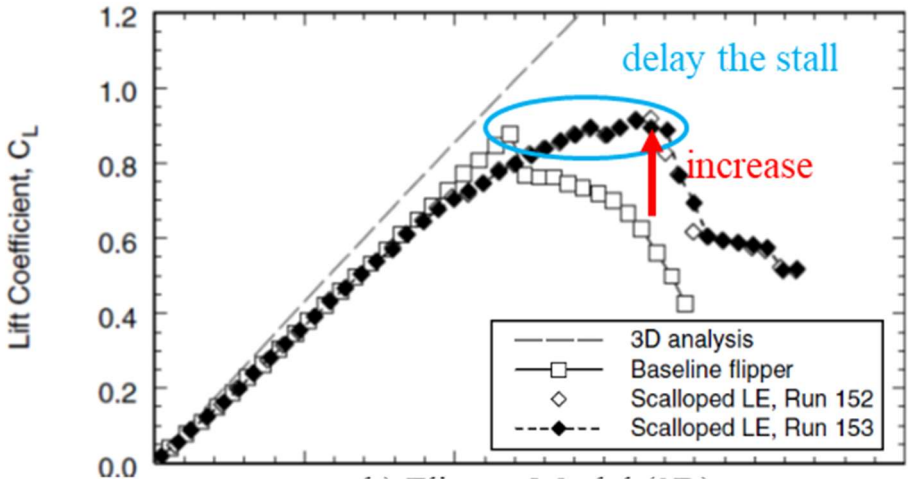

b) Flipper Model (3D)

Figure 1.5 Aerodynamic characteristics of scallop flipper [5]

Pedro et al. [7] employed the experimental research of comparison the scallop flipper and smooth flipper as well as the CFD simulation on Reynolds number 5 x 10^5. RANS turbulence model Spalart – Allmaras was used in their computation research. This comparison is obtained how to improve the aerodynamic performance of the wings. Separation on the flipper will affect its performance. In Figure 1.6**,** the separation on smooth flipper grows rapidly in the root direction. They concluded that scallop flipper resists to separation more efficiently than the smooth flipper. Figure 1.7 shows the vorticity magnitude of Pedro et al. research. The tubercles work as the vortex generator. The root and the tip flipper produce similar vortex structures. The

large stream-wise vortex structures around for scallop flipper has much more momentum which delays the separation, it described in Figure 1.7 a). This study only focused on the steady case. Meanwhile the low Reynolds number has been chosen in this case.

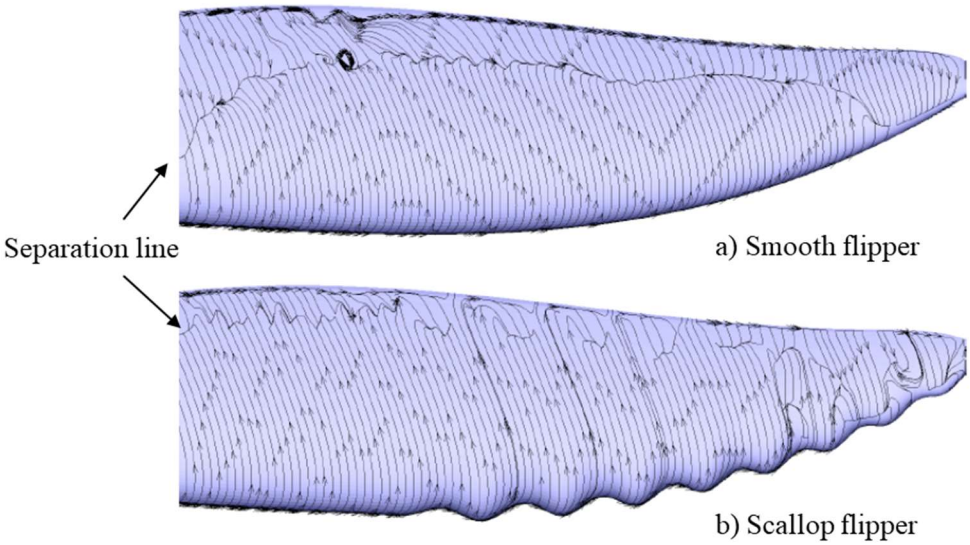

Figure 1.6 Averaged shear stress streak-lines for $\alpha = 12.5°$ [7]

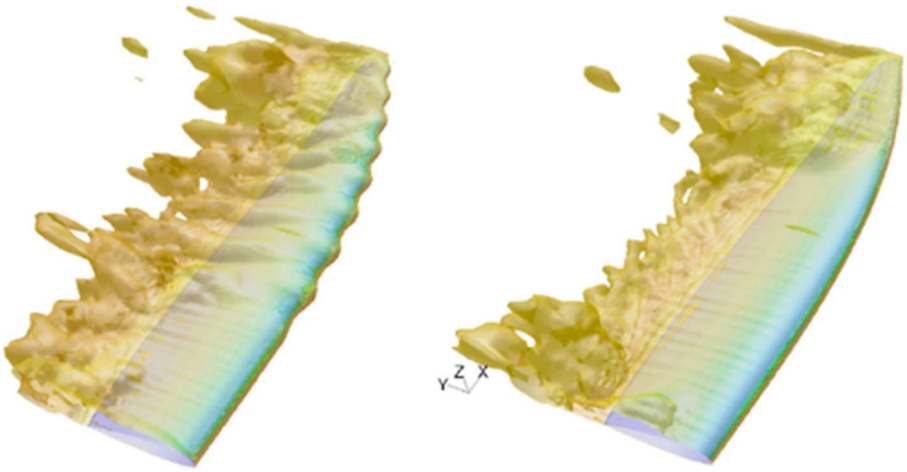

Figure 1.7 Vorticity magnitude distribution [7]

An experimental and numerical research of bio-inspired sinusoidal leading edge on NACA 0020 profile has been employed by Post et. al. [8] with scallop flipper shape. Steady case only was performed in their research at the range angle is $-2° \leq \alpha \leq 24°$. They were concluded that the mechanism by which the leading-edge modifications alter the flow

characteristics is likely due to the spanwise momentum gradients. The sinusoidal leading-edge modifications act to remove much of the unsteadiness from the flow.

Table 1.1 summaries the tubercles effect on the scallop flipper shape discussed above.

Table 1.1 Summaries of previous research using scallop flipper model

Researcher	Model	Result
Miklosovic et. al. [5], [6]	Scallop flipper NACA 0020 with and without tubercles	• The flipper of humpack whale cross sectional is similar with NACA 0020 profile. • The scallop flipper with tubercles can delay stall approximately 40%. • The lift of the scallop model has higher lift at higher incidence angles. • However, the mechanism of delaying the stall in their research is remaining unclear.
Pedro et. al. [7]	Scallop flipper with and without tubercles	• The large stream-wise vortex structures around for scallop flipper has much more momentum which delays the separation. • Only focused on steady case using low Reynolds number
Post et. al. [8]	Scallop flipper with NACA 0020 profile with tubercles	• The leading-edge modifications alter the flow characteristics is likely due to the spanwise momentum gradients • Steady case only at the range angle $-2° \leq \alpha \leq 24°$.

Johari et al. [9] explored the lift, drag, and pitching moments of airfoils with leading-edge sinusoidal protuberances in a water tunnel and compared them with a baseline 634-021 airfoil. They investigated the effect of the shape of WLE on end-plated rectangular wings. The shape of WLE in their research was sinusoidal protuberance, which is put on the leading edge of the wing. The foils with the leading-edge protuberances did not stall in the same manner as the baseline foil with the smooth leading edge. In the post-stall regime, the airfoils with protuberances had higher lift coefficients by as much as 50% over the baseline foil. The amplitude of the protuberances had a distinct effect on the performance of the airfoils, whereas the wavelength had little. Their research only conducted in steady case. Beside that the flow pattern mechanism was not observed.

Hansen et. al. [9], [11], [12], [13] has been explored the effect of tubercles on the lift and drag forces, flow behavior, and noise generation in her thesis using tubercles on NACA0021 and NACA 65-021 profile. Tubercle effectiveness increased with smallest amplitude and wavelength (A2λ7.5 and A4λ30). Consideration of an optimal amplitude to wavelength (A/λ) ratio is the important thing because its effected to flow pattern on the wings. Figure 1.8 described the lift coefficient against the angle of attack for the full-span model and semi-span model. In this case, the wavy leading-edge wing which has smallest amplitude and wavelength has the highest value among the other modified wing. The smallest amplitude and wavelength tubercles have the best performance. The whole modified wing using wavy leading edge unable to acquire the higher lift coefficient. Besides that, the maximum lift coefficient has a lower value than the baseline wing. Meanwhile, after stall condition, several modified wings have a higher lift coefficient than the baseline wing. It means that the wing using wavy leading edge is capable to recover the forces. Figure 1.8 b) shows 3D case results, but the tendency is similar to 2D case results. The effectiveness of tubercles depends on the Reynolds number than the 3D effects. Counter-rotating vortex was found in the tubercles. The evolution of streamwise vortices were observed in steady flow only.

Arai et al. [14], [15] employed research using a circular water channel with NACA0018 profile to explore the mechanism of stall delay. It was conducted with numerical simulation also with LES turbulence model. The predicted lift and drag coefficient of pre-stall and post-stall conditions are in a good agreement with the experimental results. The shorter wavelength of the protuberance is better for producing large lift force at the post-stall angles of attack on the rectangular wing. Arai et al. also performed the experimental method. From these studies, the wing using a wavy leading edge has a lower maximum lift value compared to the baseline wing with the pre-stall angle of attack. But the wing with a wavy leading edge is resist to separation at the post-stall condition. Figure 1.9 shows the velocity magnitude distributions in their research. The separation point in the Figure 1.9 b) occurred later compare with the baseline in Figure 1.9 a). They conclude that the wavy leading edge can restrain flow separation and delay stall. Their research only focused on steady case only at aspect ratio 1.6.

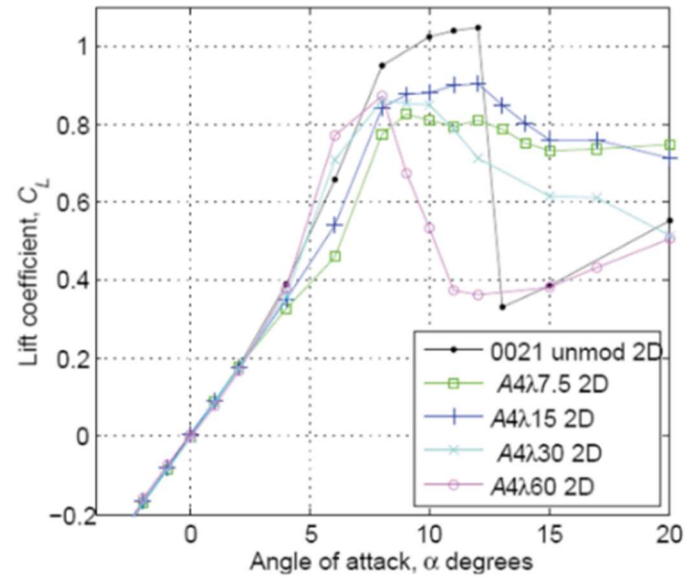

a) Full Span model (2D)

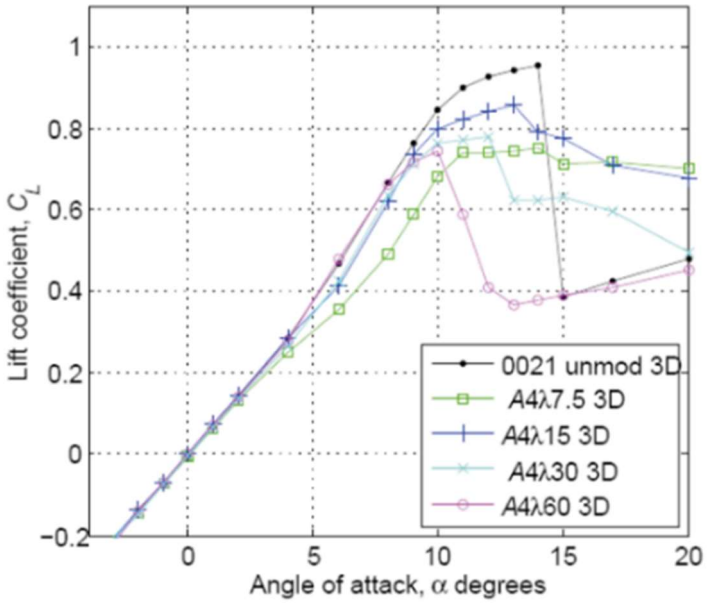

b) Semi Span model (3D)

Figure 1.8 Lift coefficient plotted against the angle of attack [9]

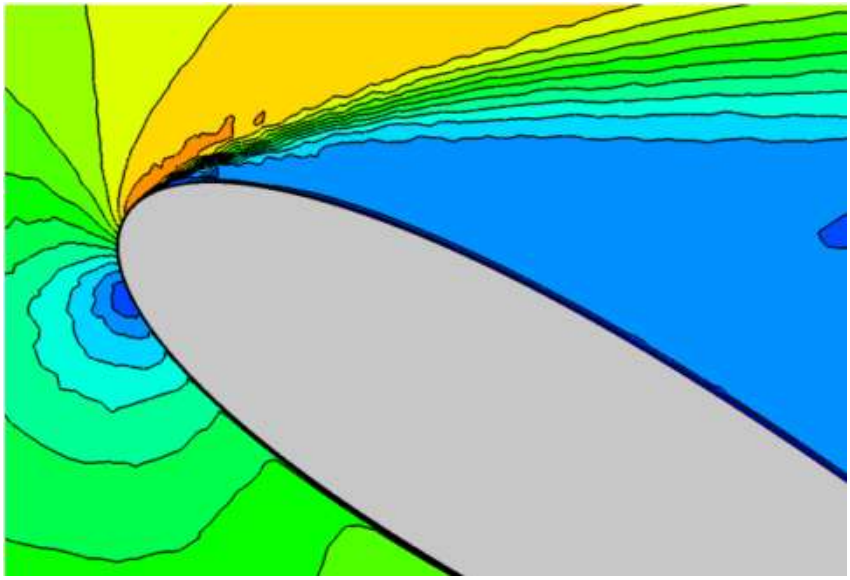

a) Baseline NACA 0018

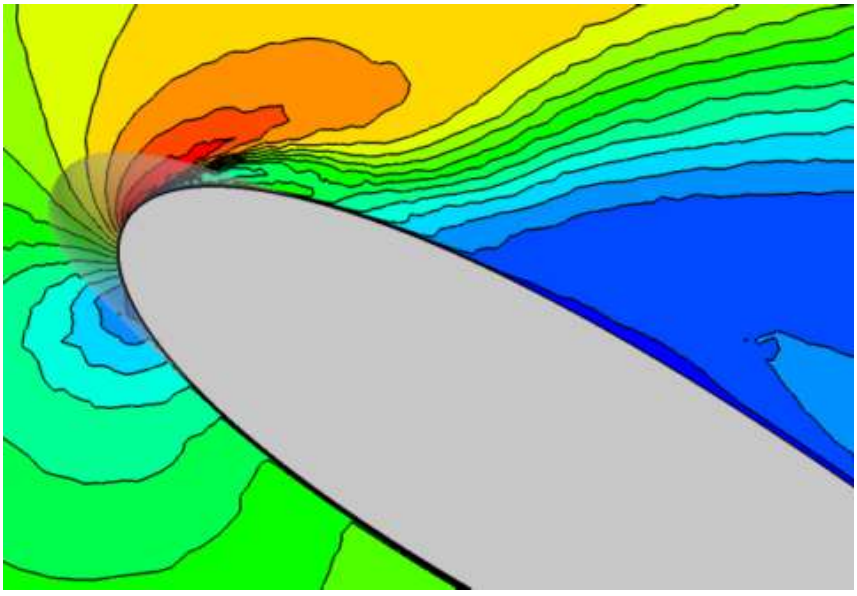

b) Wavy leading edge (WLE) wing type 2

Figure 1.9 Velocity magnitude distributions around the leading edge [15]

Lohry et al. [16] conducted research to find out the characteristics and design of the tubercle leading edge on the NACA 0020 wing using Reynolds number at (0.62-5) x10^5. The CFD analysis using RANS closed by a Menter SST k-ω turbulence model reproduces experimental measurements and trends with reasonable accuracy, even at a Reynolds numbers lower than the one encountered in most envisioned practical applications. A comparison with the results obtained for the baseline wing with a Spalart-Allmaras and Menter SST indicates that the SST model reproduces more closely the experimental curves, and therefore was selected for the remainder of this study.

A research about separation control on the hydrofoils with leading edge tubercles at Reynolds number 1.4 x 10^4 is conducted by Wei et al. [17]. The variations are amplitude and wavelengths of the hydrofoil 634-021 profile. Larger wave amplitudes and smaller wavelengths tend to perform significantly better in flow separation control. Streamwise counter rotating vortex pairs (CVPs) was explored. Leading edge tubercles create very regular CVPs and evolution of these CVPs greatly affects the flow separation behavior. Under very low Re number, the flow can separate rather easily from the baseline hydrofoil surface. They state that under very low Reynolds number, the flow could separate rather easily from the baseline hydrofoil surface.

Serson et al. [18] were studied about numerical simulation on the NACA 0012 wing with wavy leading edge and wavy trailing edge. The experiment was conducted with 9 variations of wavelength (λ) and amplitude (h) in leading edge and trailing edge. The shortest wavelength has no significant effect on the result. For $\lambda/c = 0,5$ and $\lambda/c = 1$ there is a reduction of the lift to drag ratio. This reduction is accompanied by a suppression in the lift coefficient fluctuations. Steady case was observed in their study at the angle of attack 0° to 20°. The flow pattern remains unclear, only the skin friction was shown to find out the formation of separation. A similar research also conducted by Maksoud et al [19] about the effect of leading and trailing edge protuberances on aerofoil performance. Protuberances on both the LE and TE of an aerofoil is more beneficial at larger angle of attack, delaying stall and having a higher L/D.

Favier et al [20] also conducted numerical study about separation control on the wing using wavy leading edge. Performed on a NACA0020 wing profile at Re = 800, deep stall configuration ($\alpha = 20°$) with and without wavy leading edge. The aim is to obtain an insight of the underlying physical mechanism responsible of the hydrodynamic performance enhancements in the absence of transitional effects, based on the free stream velocity and the

chord length. They stated that the shedding regime disappears, the flow is dominated by streamwise structures generated by the bumps and the boundary layer is partially attached to the wall in correspondence with the crest positions.

Aftab et al [21] studied about mimicking the humpback whale in an aerodynamic perspective. In their research, a comprehensive review of the work on tubercles in the past decade was observed. Their research on the Tubercle Leading Edge (TLE) concept has helped to clarify aerodynamic issues such as flow separation, tonal noise and dynamic stall. TLE has produced a significant reduction in the tonal noise, the broad band noise and cavitation. Tubercles help the airfoil in achieving a gradual stall in the post stall region, thus maintaining stability. Numerical predictions carried out using S–A, k–ϵ, SST k–ω, DNS, LES, DES and DDES turbulence models are reported. DDES results are in better agreement with the experimental values.

Skillen et al. [22], [23] conducted research about the undulating leading edge effect on the wing. LES simulation using open FOAM package was conducted with NACA0021 profile. The leading edge modified with undulations amplitude 1.5%c and wavelength 21%c. Reynolds number 120.000 and angle of attack 20° is considered. The study explores the flow physics and the mechanism by which the post-stall aerodynamics benefit. Results show that 36% increase in mean lift and 25% decrease in mean drag. The undulations induce a strong spanwise pressure gradient due to the fact that the bulk of the oncoming flow is redirected behind the chord minima.

Huang et al. [24] conducted experimental research in a subsonic low speed wind tunnel using a SD8000 airfoil profile. The aim of their research is explored the effect of leading edge protuberances at the stall region of Horizontal Axis Wind Turbines (HAWT). From their research, the static model is better performance with smaller amplitudes. The presence of leading-edge protuberances would effectively delay the stall.

Similar research found in Torro et al. [25] research. A numerical simulation was employed in their research using NACA 0021 profile and WLE at Reynolds number 1.2×10^5. They clarified that the structure of a pair counter-rotating stream-wise vortices generated around the wavy leading edge. These stream-wise vortices prevented the separation flow.

A recent study was studied by Wei et. al. [26] about flow structures of moderate aspect ratio (AR = 4) on the leading-edge tubercle wings. A NACA634-021 profile with tubercles LE in finite and infinite wing was used in their study with variation of amplitude and wavelength on the tubercle leading-edge. They concluded that larger tubercle amplitude A leads to gentler

stall and smaller tubercle wavelength λ improve maximum lift. The larger flow recirculating bubbles and comparatively inboard spanwise flows associated with the tip vortex flow separation.

To make clearly understanding, Table 1.2 shows the summaries of previous research that conducted using rectangular wing as mentioned above.

Table 1.2 Summaries of previous research using rectangular wing model

Researcher	Model	Result
Johari et al. [9]	NACA 634-021 airfoil with an endplate, the sinusoidal protuberances on the leading edge	• In the post-stall regime, the airfoils with protuberances had higher lift coefficients by as much as 50% over the baseline foil. • The flow pattern mechanism was not observed.
Hansen et. al. [10], [11], [12] and [13]	tubercles airfoil, NACA0021 and NACA 65-021	• Tubercle effectiveness increased with smallest amplitude and wavelength. • Counter-rotating vortex was found in the tubercles. • The evolution of streamwise vortices were observed in steady flow only.
Arai et. al. [14] and [15]	NACA 0018, wavy leading edge	• The shorter wavelength of the protuberance is better for producing large lift force at the post-stall angles • The wing with a wavy leading edge is resist to separation at the post-stall condition. • The research only focused on steady case only at aspect ratio 1.6.
Lohry et. al. [16]	NACA 0020, Menter SST k-ω turbulence model	• a Menter SST turbulence model reproduces experimental measurements and trends with reasonable accuracy.
Wei et. al. [17], [26]	PIV experiment with NACA634-021 profile at Re = 1,4 x 10^4	• Leading edge tubercles create very regular counter rotating vortex pairs greatly affects the flow separation behavior. • Larger tubercle amplitude A leads to gentler stall and smaller tubercle wavelength λ improve maximum lift.

Researcher	Model	Result
Serson et. al. [18], Maksoud et. al. [19]	Tubercles/protuberances on the leading edge and trailing edge	• The flow pattern remains unclear, only the skin friction was shown to find out the formation of separation. • Protuberances on both the LE and TE of an aerofoil is more beneficial at larger angle of attack, delaying stall and having a higher L/D.
Favier et. al. [20]	NACA 0020 profile at Re = 800,	• The flow is dominated by streamwise structures generated by the bumps
Aftab et. al. [21]	A review of previous research with various wing profile	• TLE shows increased lift by delaying and restricting spanwise separation. • Tubercles help the airfoil in achieving a gradual stall in the post stall region, thus maintaining stability.
Skillen et. al. [22], [23]	NACA 0021 at Reynolds number 1.2 x 10^5	• Results show that 36% increase in mean lift and 25% decrease in mean drag. • The undulations induce a strong spanwise pressure gradient
Huang et. al. [24]	SD8000 profile Reynolds number 1 x 10^5	• The presence of leading-edge protuberances would effectively delay the stall.
Torro et. al. [25]	NACA 0021 profile at Reynolds number 1.2 x 10^5	• Counter-rotating stream-wise vortices generated around the wavy leading edge that prevented the separation flow.

An interesting study of comparison between rectangular and tapered wing has been conducted by Javaid et. al. [27] by using towink tank experiment and CFD analysis. They conducted a research hydrodynamic characteristics and dynamic stability of an underwater glider on NACA 0016 profile. The underwater glider layout is provided in the Figure 1.10. To find out the effectiveness of glider shape, the stability on the wings has been compared. The important results of their research are even though tapered wing has lower lift force but it can improve the dynamic stability.

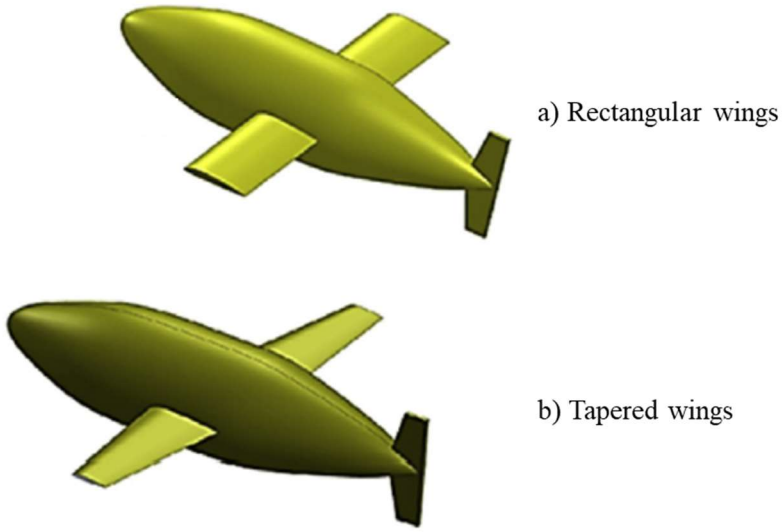

Figure 1.10 Underwater glider of rectangular and tapered wings [27]

Another flow control method has been conducted by Choudry et al. [28]. Their research purpose is controlling the dynamic stall for wind turbine applications. NACA 0012 profile and variations angle of attack has been chosen experimentally with the wind tunnel. They use 3 methods, i.e. Vortex Generators (VGs), Elevated Wire (EW) and cavity. The schematic illustration is shown in Figure 1.11**.** Only VG and EW able to improve the post-stall characteristics of the airfoil. Stall angle occurs at the angles 20° and 23° for baseline profile and VG, respectively. The vortex generators and the elevated wire concept are equally effective for dynamic stall control. The cavity acted as a reservoir to store the reverse flow, and therefore an approximate constant delay in the onset of flow separation was observed. The vortex generators and the elevated wire concept are equally effective for dynamic stall control. The cavity acted as a reservoir to store the reverse flow and therefore an approximate constant delay in the onset of flow separation was observed. The cavity leads to a consistent delay in the dynamic stall onset, but no beneficial effects were observed during the post-stall. The VG produces counter-rotating vortex. VG able to delay stall angle on NACA 0012 (about 23°) but it inefficient to improve the lift forces at the post-stall region.

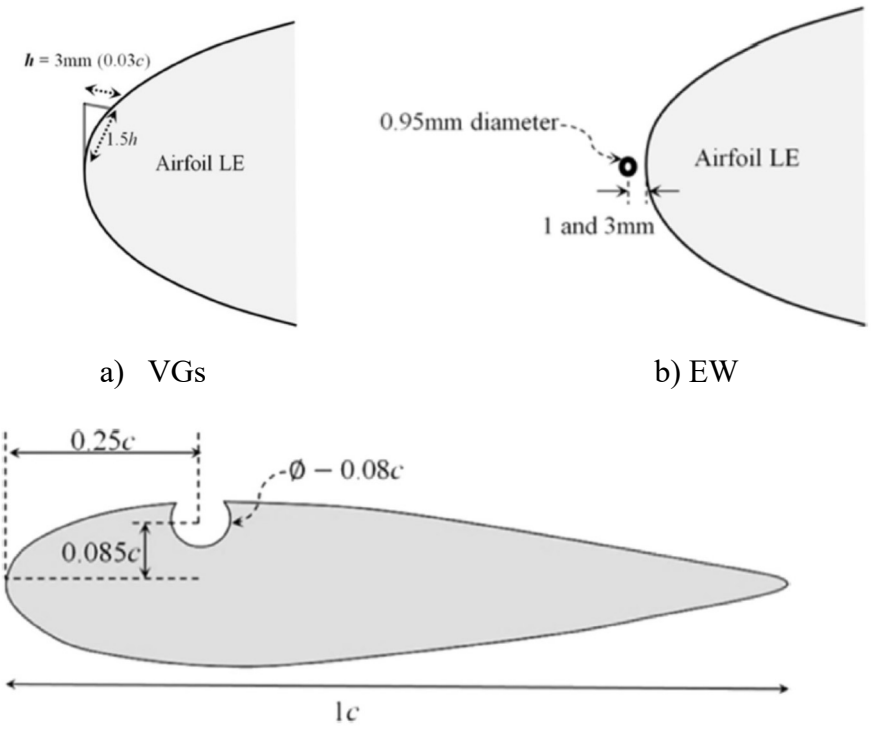

Figure 1.11 Schematic illustration of (a) VGs, (b) EW and (c) cavity [28]

The following section will explain tapered wing shape for comparison. A rectangle wing is widely used as a fin stabilizer on the ships. Based on the separation theory, the fluid flow will be through separation on its surface. If the wing attached to a body such as on a plane, the separation will occur in the area around the body junction. Furthermore, there is a wing tip vortex damages fluid flow. Wing tip vortex on the rectangle wing can affect the fluid flow it. There are several ways that can be done to reduce the wing tip vortex, such as a modified form of the rectangle wing into the tapered wing. Inspired by the humpback whale flipper or fin of the fish, the rectangle wing as a fin stabilizer on the ships will be modified into a tapered wing. The tapered wing is expected has more effectively performed than a rectangle wing ($Cl/Cd > 0$).

There are some examples of wing planform as Talay et al. [29] mentions in his book. The airfoil section shape, planform shape of the wing and placement of the wing on the fuselage depend upon the airplane mission and the best compromise necessary in the overall airplane design. The wing planform is adapted to the application. Besides that, the aspect ratio must also be considered. Both of these factors can affect the lift coefficient it produces. According to

Hiong et al. research [30] about the effect aspect ratio on rectangular wing planform, increasing aspect ratio will decrease the stall angle. In general, the expected stall angle is not too low. If the wing has a low stall angle, it means that the wing will stall at a low angle of attack.

A research with tubercles on the SD7032 profile with tapered swept back wing has been performed by Wei et. al. [31] The aim of this work is used to underwater glider application and focused on the angle 20° only. The flow separation mitigation possibly enhances the hydrodynamic performance for the present tapered swept-back wing, and hopefully leads to a longer cruise range for the underwater gliders.

Ogura [32] studied the wavy leading edge on the tapered wing using a water channel. His research compared with the rectangular wing. NACA 0020 profile was selected. The tapered wing model is shown in Figure 1.12 The tapered wing with wavy leading edge has lower lift coefficient (*Cl*) value than the baseline at the angle of attack 12°. But at the post-stall region, the tapered wing with wavy leading edge able to acquire the lift coefficient. Ogura also studied about the comparison of the tapered wing and rectangle wing. Figure 1.13 shows the comparison between the rectangle wing and tapered wing. The tapered wing has higher increase rate of *Cl* (δ_{Cl}) about 39% at angle of attack 20°. Meanwhile, the rectangle wing has the maximum increase rate of *Cl* (δ_{Cl}) about 31% at angle of attack 26°, as shown in Figure 1.14. The wavy leading edge has suppression effect on tapered wing. The future work from his research is increasing the maximum lift coefficient and delaying the stall on the tapered wing with wavy leading edge. It may be done with the wavy leading edge only placed around the mid-span to the wing tip.

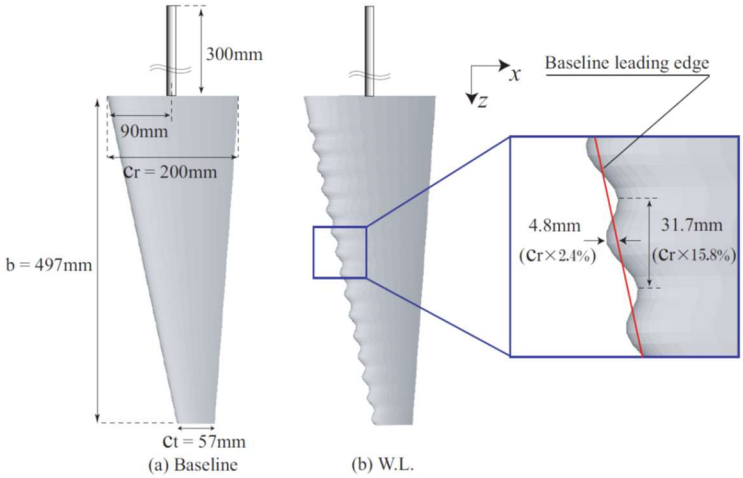

Figure 1.12 Wavy leading edge on tapered wing models [32]

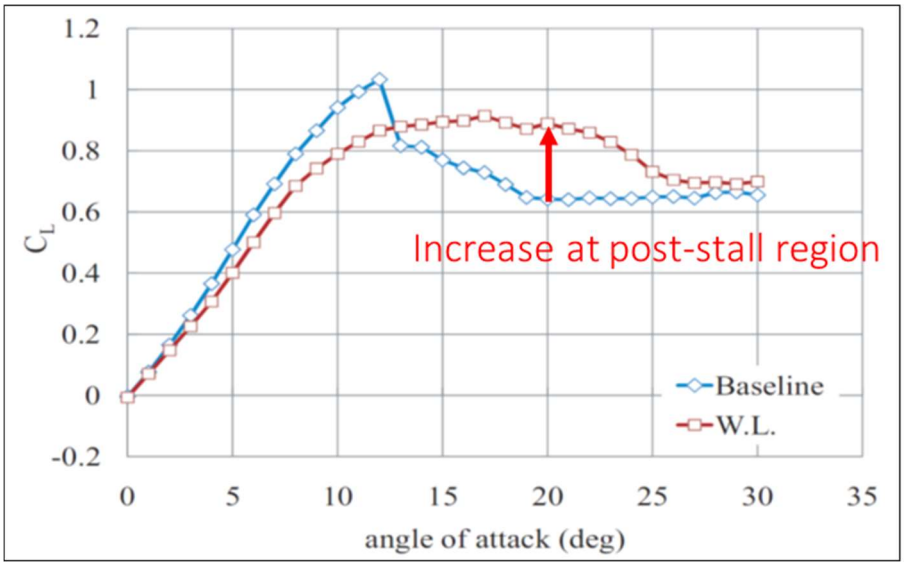

Figure 1.13 Lift coefficient characteristics for tapered wing [32]

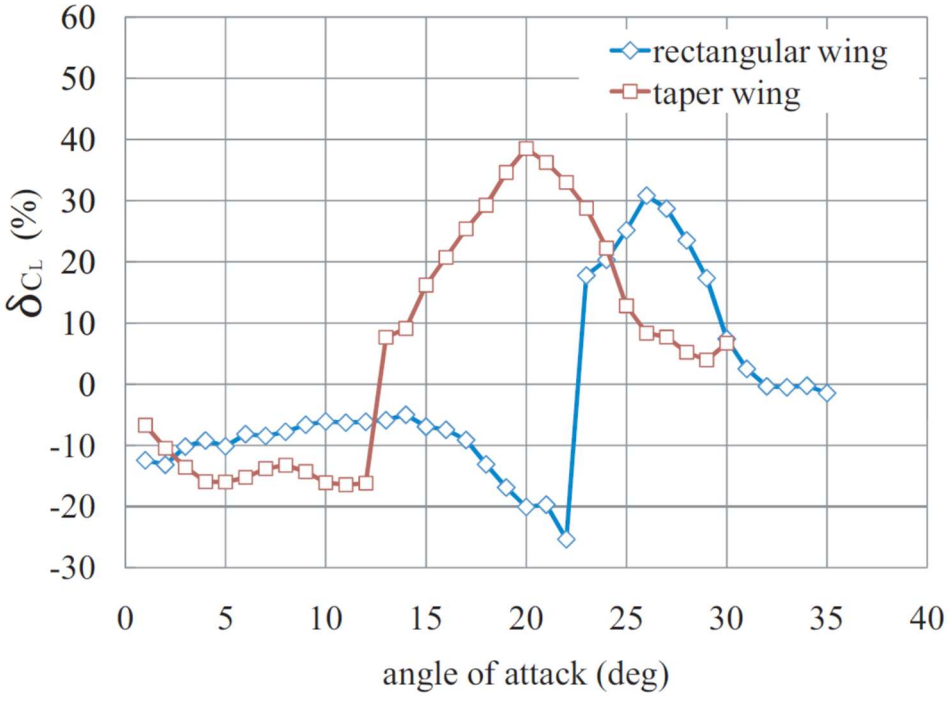

Figure 1.14 Increase rate of lift coefficient on tapered wing [32]

A similar research was performed by Nagaoka [33] to find out the WLE effect on the tapered wing with NACA 0018 profile. The effect of suppressing stall by the leading edge adduct was obtained. The WLE on tapered wing can delay the tip stall.

In this dissertation, to find out the WLE effect regarding various aspect ratios and taper ratio of the wing will be discussed. All previous studies mentioned above were only conducted to find out the wavy leading-edge effect in one aspect ratio on the rectangle wing or tapered

wing. In the next section, the effect of wavy leading edge was investigated correlated to various aspect ratios and the wing shapes. Numerical investigations were carried out to understand effect of wavy leading edge on delaying the stall in steady and unsteady case. Next section, briefly explanations of previous researches in unsteady case are given.

A numerical research about leading edge protuberances on a static wing and pitching wing were employed by Wang et. al. [34] on NACA 0010 profile. In turbulent flow, the leading-edge protuberances act in a manner similar to vortex generators, enhancing the momentum exchange within the boundary layer. Streamwise vortices do contribute to the delay of the stall occurrence. For a pitching wing in turbulent flow, the leading-edge protuberances have limited effect under the condition of their computation. the thrust jet and the vortices in the vortices in the wake are not changed by the leading-edge protuberances.

Another unsteady case research was conducted by Torro [35] in his thesis report. The unsteady numerical simulations over a wavy leading edge on NACA0021 wing has been done with the wavelength and amplitude of the WLE is 11% and 3% of the mean chord, respectively. For unsteady case simulations, WLE wing has weaker trailing edge vortices compared to the straight leading-edge wing.

Gaillarde [36], [37] performed the research about the dynamic stall on the fin stabilizer. An experimental study using SMB (Seakeeping and Manuvering Basin) was conducted by him to investigate dynamics behavior and characteristic of lift and drag on the dynamic behaviour with NACA 65-02 profile at AR 1.95. Above 10° angles of attack, the effect of cavitation is clearly present with a lift degradation of about 15%. But the disadvantage of his research is the behavior of the fins under large angles of attack and high speed, including stall is not evaluated.

Lin et. al. [38] employed the numerical study on the application of Vertical Axis Wind Turbine (VAWT) with SST k-ω turbulence model. They use the NACA 0015 profile with modified wing wavy leading-edge and wavy trailing-edge. They were concluded that the wavy leading-edge able to increase the thrust force than the wavy trailing-edge. Unfortunately, in their study the mechanism increasing the thrust is remain unclear.

A research by using NACA 0018 profile with serration of leading edge was performed by Wang et. al. [39] on the vertical axis wind turbine (VAWT) with the rotating motion. Their schematic of the turbine blade as shown in the Figure 1.15. The serration leading edge has the amplitude 0.12 and wavelength 0.25 of the chord length. From their results, the flow separations and torque fluctuations are significantly suppressed due to the passive flow control strategies

implemented in the optimized VAWT model. The vorticity distribution results show that the flow separation is significantly suppressed due to the existence of leading-edge serration design and helical blade configuration.

An application by using undulated leading edge on the tidal turbines has been done by Shi et. al. [40] with S814 section profile. The undulation shape of their work has height and amplitude 0.1 and 0.5 of the chord length, respectively. The test results revealed that the leading-edge undulated turbine has a stable hydrodynamic performance over a combined range of current speeds and waves.

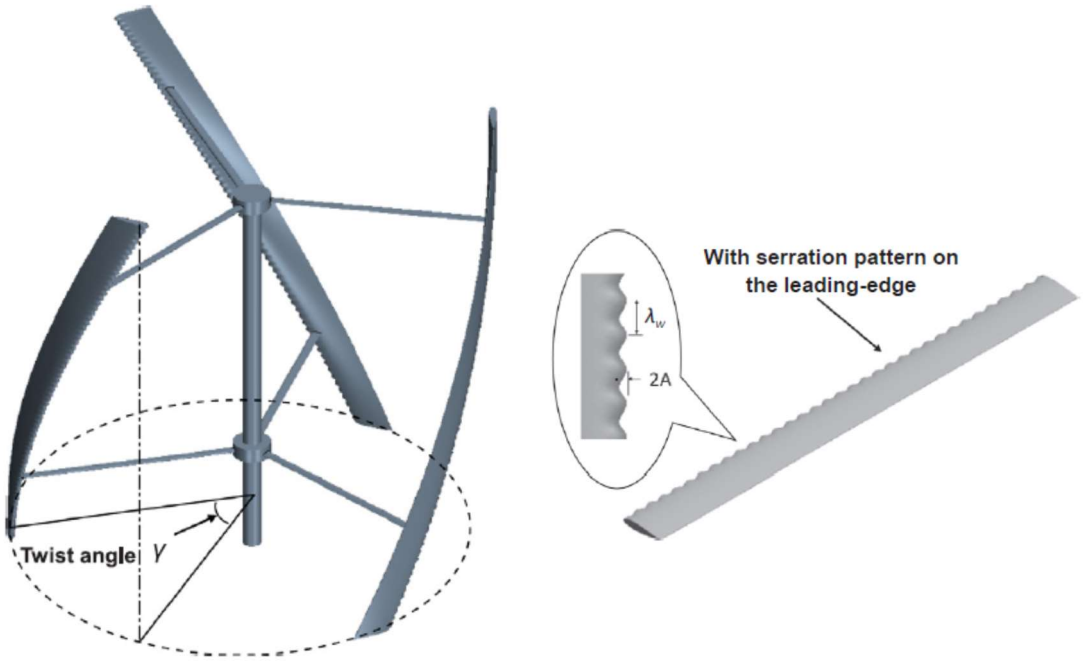

Fig. 5. Helical design.

Figure 1.15 Schematic view of turbine blade [40]

To understand the previous study in unsteady case, the summary of them is given in the Table 1.3.

Table 1.3 Summaries of previous research in unsteady case

Researcher	Model	Result
Wang et. al. [34]	NACA 0010 profile on static and pitching wing	• The leading-edge protuberances act in a manner similar to vortex generators • For a pitching wing in turbulent flow, the leading-edge protuberances have limited effect under the condition of their computation.
Torro [35]	NACA 0021 profile	• For unsteady case simulations, WLE wing has weaker trailing edge vortices compared to the straight leading-edge wing.
Gaillarde [36], [37]	NACA 65-02 profile at AR 1.95	• The effect of cavitation is clearly present with a lift degradation of about 15%. • the behavior of the fins under large angles of attack and high speed, including stall is not evaluated. • The wavy leading edge as vortex generator is not explored.
Lien et. al. [38]	NACA 0015 with wavy on the leading and trailing edge	• the wavy leading-edge able to increase the thrust force than the wavy trailing-edge. • the mechanism increasing the thrust is remain unclear.
Wang et. al. [39]	NACA 0018 with serration leading edge A=0.12*c* and α=0.25*c*	• The flow separation is significantly suppressed due to the existence of leading-edge serration design. • The flow mechanism on the serration leading edge remains unclear
Shi et. al. [40]	S814 profile with undulation shape A=0.1*c* and α=0.5*c*	• the leading-edge undulated turbine has a stable hydrodynamic performance over a combined range of current speeds and waves.

From previous studies were mentioned in the above, there are not many researches investigating WLE effect on the tapered wing and so on in the unsteady case. Commonly, the previous researches in unsteady case have been done in rotating motion only. This only used in wind turbine, or helicopter blade only. Another unsteady motion is needed to be explored such as in pitching motion. So, the benefit of WLE effect on the wing could be applied for fin stabilizers also. Besides that, the various wing shape is necessary to be explored to find out the maximum utilities by using the WLE application.

1.3 Aims and Objectives of the Research

There is not much researches study about the wavy leading edge for unsteady case. However, several utilities could use the progress of the research about the wavy leading edge on the flipper wing such as fin stabilizer, and horizontal axis wind turbines. It is important to conduct the research with unsteady condition for some applications. The aspect ratio of the wing is an important thing to find out the effect of WLE with various aspect ratios. It is an interesting to apply this benefit for fin stabilizer on the ship, wind turbine or other aircraft. This research has been done not only in steady case, but also in unsteady case. The aim of this research is to investigate the performance of the wing with a wavy leading-edge regarding the wing aspect ratio. The improved performance intended are increased lift and reduced drag with various aspect ratios. In the beginning, the rectangle wing was chosen to approach the humpback whale flipper which is the background of this research that is inspired by its flipper. For comparison, studies that modify model rectangle wing and tapered wing were also discussed. There are three types of tapered ratio used to find out the close shape of humpback whale flipper. The mechanism of stall delay by wavy leading edge was explored to get a clear explanation.

1.4 Structure of the Research

The dissertation is structured as follows. Chapter 1 introduce and explain the background, previous studies, and the aims of this research. Hereafter, the author explained chapter 2 about the methods in experimental (as references) and numerical and also the governing equations. In chapter 3, the wavy leading-edge effect on rectangle wing with aspect ratio 1.6 has been discussed in unsteady motion with three reduced frequencies i.e., k = 0.09, 0.12, and 0.25. Then in chapter 4, various aspect ratios effect are investigated in the wavy leading-edge wing i.e.,

aspect ratio 1.6, 3.9, 5.1, 7.9, and 9.6. In chapter 5, a comparison of unsteady case in various aspect ratios was employed. Next, in chapter 6, a comparison of rectangle wing and tapered wing discussed related to the wavy leading-edge effect regarding the wing shape. Finally, in the chapter 7 is conclusion of all the work of this dissertation and briefly explanation of the future work.

1.5 Summary

By learning of morphology on the humpback whale flipper, it has benefits to improve the hydrodynamics performances. This benefit able to be applied in many utilities such as fin stabilizer, wind turbine, or other turbo-machineries. To find out the maximum application, it is necessary to employ the research in a steady case and unsteady case. Meanwhile, the wing shape is needed to approach the humpback whale shape flipper. This could be done by modified the rectangular wing into the tapered wing.

CHAPTER 2

METHODOLOGY AND GOVERNING EQUATION

In this chapter, methodology and governing equation were described into three sections, i.e. wing scheme; the experimental method, and numerical method. In the first section, wing scheme and its shape was described. Then, experimental method carried out to observe the flow characteristics of the wing with a circular water channel in Hiroshima University, Japan. The numerical approaches by CFD (Computational Fluid Dynamics) Autodesk. By using CFD, the parameters were explored are pressure distribution on the wing, streamlines, and the forces of the wing.

2.1 Wing Scheme

As mentioned above in the chapter 1, this research is inspired from the humpback whale flipper. The NACA 0018 profile with rectangular and tapered shape are chosen to approach its flipper. The following Figure 2.1 below is the coordinate systems was employed in the wing. Original coordinate (*O-xyz*) was located on the leading edge of the wing. Dimension of the rectangular wings used are based on the aspect ratio (AR) of the wing. For the information, five aspect ratios were used, i.e. AR 1.6, 3.9, 5.1, 7.9, and 9.6. All the wings have the chord length I 125 mm, except the wing with 1.6 aspect ratio, it has the chord length 250 mm. Span of the wing is adjusted to the aspect ratio of the wing. Figure 2.2 shows the plane view of the wing in various aspect ratio. The Reynolds number 1.4 x 10^5 was used in this research.

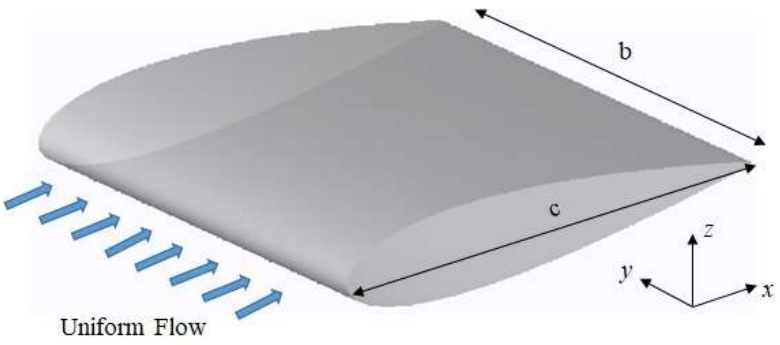

Figure 2.1 Coordinate system

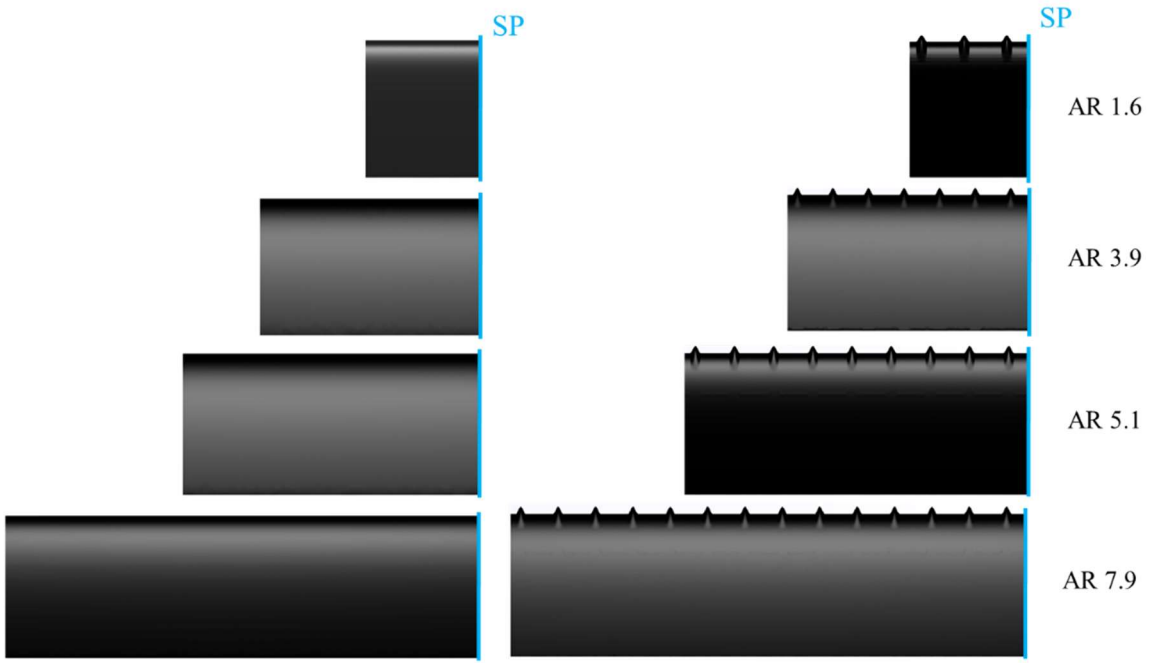

(a) (b)

Figure 2.2 Plane view of the rectangular wings: (a) Baseline; (b) WLE

This study using modified of the wing by attaching the wavy leading edge on the wing. The schematic view of wavy leading edge is given in the Figure 2.3.

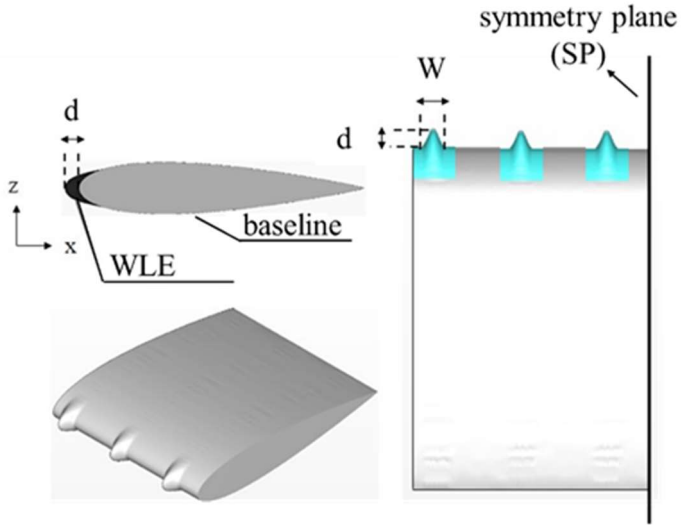

Figure 2.3 Schematic view of wavy leading edge

The wavy leading edge is determined based on the following formula:

$$x_{WLE\,(y)} = x_{LE} - [\frac{d}{2}\sin\left\{\frac{2\pi}{W}\left(y - \frac{W}{4}\right)\right\} + \frac{d}{2}] \quad (2.1)$$

Where X_{LE} is x-coordinate of baseline wing, X_{WLE} is x-coordinate for wavy leading edge, W and d is width and height of wavy leading edge, respectively. In this study, d = 5% and W = 8% of the chord length were used. This study was conducted on steady and unsteady case. For unsteady case, the wing motion regarding the following equation:

$$\alpha\,(T_0) = \alpha_c + \alpha_a \cos\,(k\,T_0) \tag{2.2}$$

, where α is angle of attack, α_c is center angle, α_a is amplitude.

The T_0 is non dimensional time with reduced frequency k. Three types of k are used in this research (k = 0.09, 0.12 and 0.25) regarding the fin stabilizer motion of the RORO ship. The T_0 and k equations are described as follow:

$$T_0 = t\,\frac{U_0}{c} \tag{2.3}$$

$$k = \frac{2\pi f c}{U_0} \tag{2.4}$$

, where t is time (s), c is the wing chord length, f is frequency (Hz), and U_0 is free steam velocity (m/s).

The wing motion is pitching motion up and down described as in the Figure 2.4 with the pivot point located at ¼ of the chord length c.

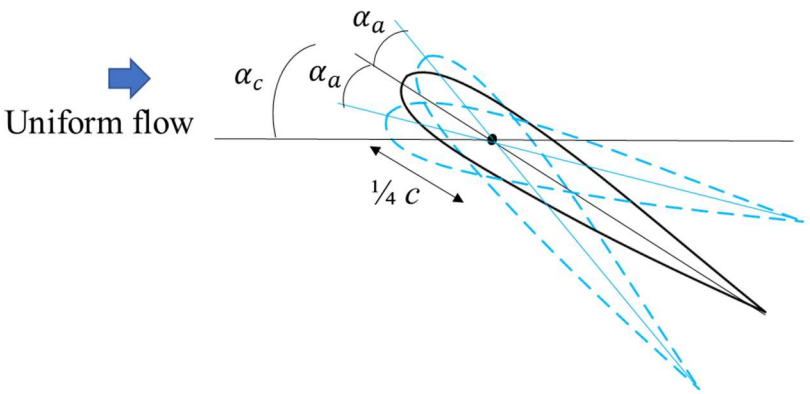

Figure 2.4 Pitching motion on the wing

Similar method with wavy leading edge, the vortex generator (VG) were used to improve the wing performance. As a comparison, Figure 2.5 shows the wing with vortex generator (VG) which is located at the leading edge. The VGs have counter-rotating vanes of height 0.016c, length 0.048c. Where the angles relative to the chord-wise direction are ±20°.

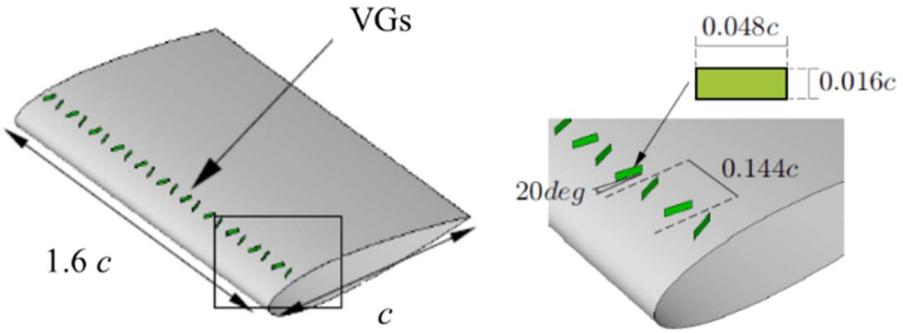

Figure 2.5 Schematic view of VG

The lift coefficient (C_L) and the drag coefficient (C_D) defined as follows:

$$C_L = \frac{L}{\frac{1}{2}\rho\,|U_0|^2 s\,c} \quad (2.5)$$

$$C_D = \frac{D}{\frac{1}{2}\rho\,|U_0|^2 s\,c} \quad (2.6)$$

, where L : lift force, D : drag force, s : span, c : chord length, ρ : fluid density, U_0 : free-stream velocity (m/s).

In this dissertation, not only rectangle wing shape was used but the taper wing also used to find out the effectiveness of the WLE regarding the wing shape. The taper wing in this case un-swept wing type. Figure 2.6 shows the plane view of the taper wing. As comparison these wings has AR about 7.9. There are 3 types of taper ratio i.e. TR 0.1, 0.3 and 0.5. The wing chord is adjusted using general equation of taper ratio (TR) as follow:

$$\text{TR} = \frac{c_{wing\ tip}}{c_{root}} \quad (2.7)$$

with $c_{\text{wing tip}}$ indicates wing tip chord length (m) and c_{root} as root chord length of the wing (m). The average wing chord ($\bar{c}$) in all TR wing types were adjusted similar to the rectangular wing, i.e. 125 mm.

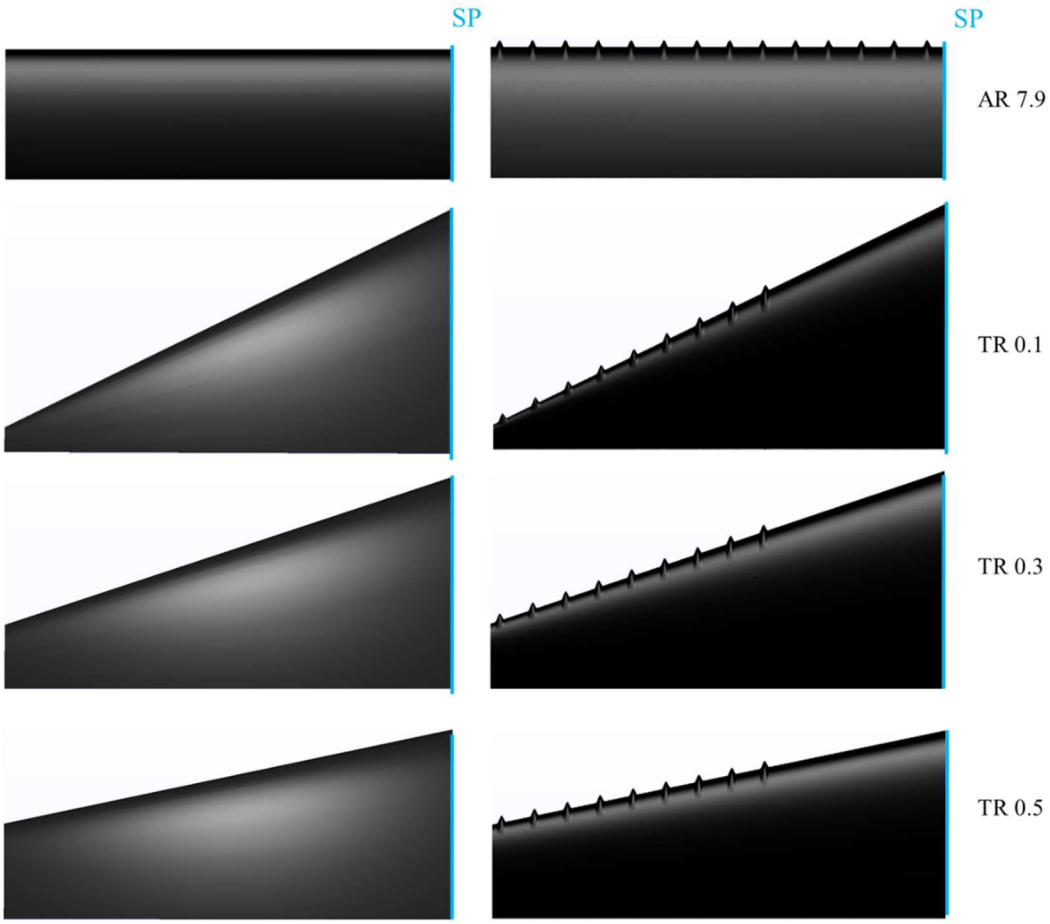

Figure 2.6 Plane view of the tapered wings

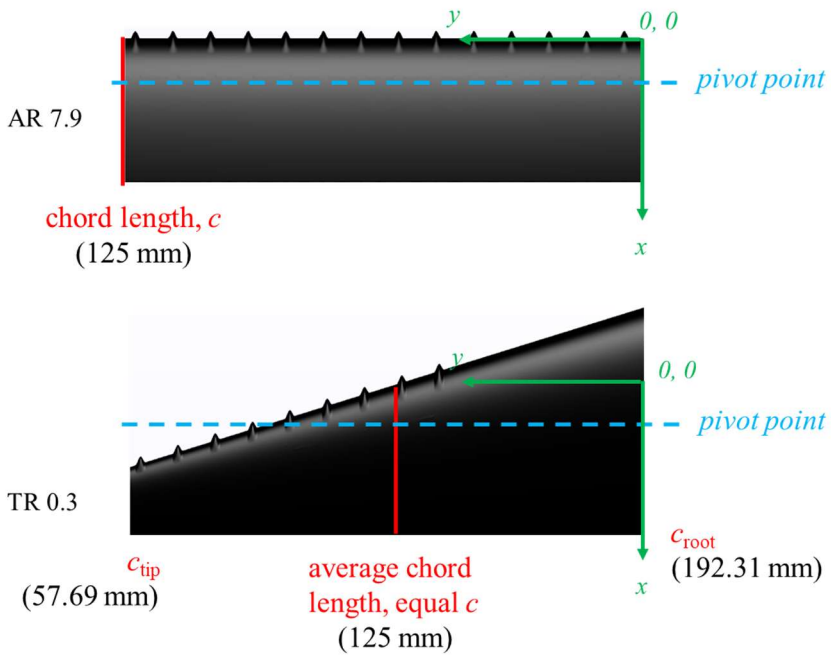

Figure 2.7 Pivot point of rectangular wing AR 7.9 and tapered wing TR 0.3

During unsteady case condition, the pivot point located at ¼ of the average chord length $\bar{c}$. Figure 2.7 describes the pivot point location for the rectangular wing with AR 7.9 and tapered wing TR 0.3.

2.2 Experimental Method

The experiments were conducted in the circular water channel at Hiroshima University, Japan. It has width 1.4 m, height 1.0 m with 3.3 m long measure cross-section. The experimental set-up shown in the Figure 2.8 specially at AR 1.6. In this research, experiments were carried out in steady and unsteady case. The depth of circular water channel is 0.9 m with the wing is located at 0.9 m from uniform flow and 0.15 m from the upper surface as shown in the Figure 2.8. Due to the limitations of the circular water channel dimension, the experiments were performed only at AR 1.6, 3.9 and 5.1. To keep the distance between wing and the bottom of circular water channel has the same ratio, the chord length of the wing was adjusted for AR 3.9 and 5.1 with c = 0.125 m. This ratio is called as the blockage ratio. The blockage ratio between the wing and the outer boundary was 8% for various aspect ratios except 1.6 aspect ratio. The blockage ratio is defined as:

$$\text{Blockage ratio} = \frac{AR\ c^2}{d} \qquad (2.9)$$

, where AR is aspect ratio of the wing, c is chord length (m), and d is depth of outer boundary (m).

In general, the details of the experiments were described in Table 2.1. The NACA 0018 profile was used with Reynolds number about 1.4 x 10^5. In unsteady case, the wing is in pitching motion at the angles $25° \leq \alpha \leq 35°$. The wing is moving up and down in accordance with the amplitude angle. Three reduced frequencies were selected based on the motion of fin stabilizer of a RORO ship. The pivot point of the wing is ¼ of the chord length.

Table 2.1 Details of experiments

Wing section	NACA 0018
Aspect Ratio	1.6, 3.9, and 5.1
Reynolds Number, *Re*	1.4 x 10^5
Reduced Frequency, *k*	0.09, 0.12 and 0.25
Mean angle of pitch motion, α_c	20° and 30°
Amplitude of pitch motion, α_a	5°

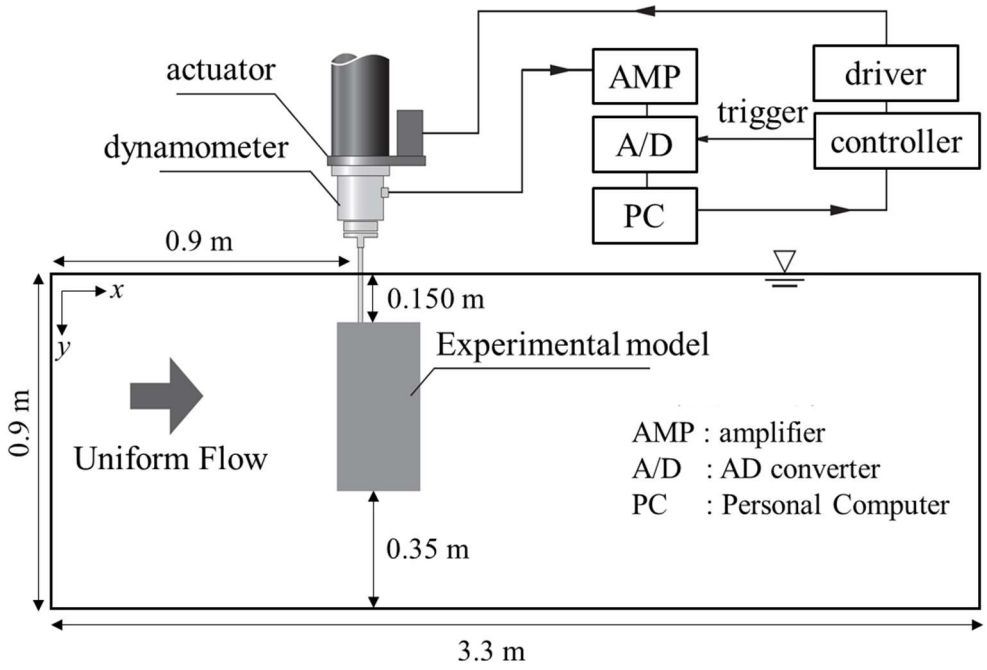

Figure 2.8 Experimental set-up at AR 1.6

2.3 Numerical Method

In general, a CFD (Computational Fluid Dynamic) package is defined as a simple method of differential partial equation including the continuity equation (conservation of mass), momentum equation and energy equation into the algebraic equations. By using the CFD, we can observe the fluid flow with virtual modeling. In this dissertation, the numerical method was performed by using Autodesk® CFD. The discretization method of Autodesk® CFD is FEM (Finite Element Method) [41]. The FEM is used to reduce the governing partial differential equations (PDES) to a set of algebraic equations. The discretization method of Autodesk® CFD is effect to stability of its computation. In the following section, the general equations were mentioned in the above as follow:

a. *Continuity equation (conservation of mass)*

This governing equation describes the transport of some quantity through the solution domain. The governing equation take the form:

$$\frac{\rho\, U\, \partial\phi}{\partial x} + \frac{\rho\, V\, \partial\phi}{\partial y} + \frac{\rho\, W\, \partial\phi}{\partial z} = \frac{\partial}{\partial x}\left(\Gamma_\phi\, \frac{\partial\phi}{\partial x}\right) + \frac{\partial}{\partial y}\left(\Gamma_\phi\, \frac{\partial\phi}{\partial y}\right) + \frac{\partial}{\partial z}\left(\Gamma_\phi\, \frac{\partial\phi}{\partial z}\right) + S_\phi \quad (2.10)$$

b. *Momentum equation*

The momentum equation is called as Navier-stoke equation where it has complex form to solve. In general, the momentum equation is defined as *x-y-z* direction as follows:

X – momentum equation:

$$\frac{\rho\, \partial u}{\partial t} + \frac{\rho\, u\, \partial u}{\partial x} + \frac{\rho\, v\, \partial u}{\partial y} + \frac{\rho\, w\, \partial u}{\partial z} = \rho\, g_x - \frac{\partial p}{\partial x} + \frac{\partial}{\partial x}\left[2\,\mu\, \frac{\partial u}{\partial x}\right] + \frac{\partial}{\partial y}\left[\mu\, \left(\frac{\partial u}{\partial y} + \frac{\partial v}{\partial x}\right)\right] + \frac{\partial}{\partial z}\left[\mu\, \left(\frac{\partial u}{\partial z} + \frac{\partial w}{\partial x}\right)\right] + S_\omega + S_{DR} \quad (2.11)$$

Y – momentum equation:

$$\frac{\rho\, \partial v}{\partial t} + \frac{\rho\, u\, \partial v}{\partial x} + \frac{\rho\, v\, \partial v}{\partial y} + \frac{\rho\, w\, \partial v}{\partial z} = \rho\, g_y - \frac{\partial p}{\partial y} + \frac{\partial}{\partial y}\left[\mu\, \left(\frac{\partial u}{\partial y} + \frac{\partial v}{\partial x}\right)\right] + \frac{\partial}{\partial y}\left[2\,\mu\, \frac{\partial v}{\partial y}\right] + \frac{\partial}{\partial z}\left[\mu\, \left(\frac{\partial v}{\partial z} + \frac{\partial w}{\partial y}\right)\right] + S_\omega + S_{DR} \quad (2.12)$$

Z – momentum equation:

$$\frac{\rho\, \partial w}{\partial t} + \frac{\rho\, u\, \partial w}{\partial x} + \frac{\rho\, v\, \partial w}{\partial y} + \frac{\rho\, w\, \partial w}{\partial z} = \rho\, g_z - \frac{\partial p}{\partial z} + \frac{\partial}{\partial x}\left[\mu\, \left(\frac{\partial u}{\partial z} + \frac{\partial w}{\partial x}\right)\right] + \frac{\partial}{\partial y}\left[\mu\, \left(\frac{\partial v}{\partial z} + \frac{\partial w}{\partial y}\right)\right] + \frac{\partial}{\partial z}\left[2\,\mu\, \frac{\partial w}{\partial z}\right] + S_\omega + S_{DR} \quad (2.13)$$

, where $S_\omega is$ rotating flow, S_{DR} is distributed resistance term

$$S_{DR} = -\left(K_i + \frac{f}{D_H}\right) \frac{\rho\, {V_i}^2}{2} - C\, \mu\, V_i \quad (2.14)$$

$$S_\omega = -2\, \rho\, \omega_i \times V_i - \rho\, \omega_i \times \omega_i \times r_i \quad (2.15)$$

c. *Energy equation*

For compressible flow, the energy equation is written in terms of total temperature:

$$\rho C_p \left(\frac{\partial T_0}{\partial t}\right) + \rho C_p V_i \left(\frac{\partial T_0}{\partial X_i}\right) = \frac{\partial}{\partial X_i}\left[k \frac{\partial T_0}{\partial X_i}\right] + q_V + \mu V_i \left[\frac{\partial^2 V_i}{\partial X_j . \partial X_j} + \frac{\partial}{\partial X_j}\frac{\partial V_j}{\partial X_j}\right] + \frac{1}{2C_p}\frac{\partial}{\partial X_j}\left[k \frac{\partial}{\partial X_i}\left(V_j V_j\right)\right] + \Phi \quad (2.16)$$

, where *I* refers to the global coordinate direction (*u, v, w* momentum equation), ω is the rotational speed and *r* is the distance from the axis of rotation, *K* is *K*-factor, Φ is the dissipation function, *Cp* is constant pressure specific heat, $g_{x,y,z}$ is gravitational acceleration in *x, y, z* directions, *T* is temperature, *t* is time, μ is viscosity and ρ is density.

Next, the procedure to proceed the Autodesk® CFD computation is following the step below:

1. Construction of the model
2. Definition of the model type
3. Initialize the boundary condition of the model
4. Define the model into small parts (meshing)
5. Solve the computation in steady or unsteady case
6. Analysis and visualization of the results

For transient analysis, the transient terms are discretized using an implicit or backward difference method. This implies that the value at the current time is dependent on the neighboring values at the current time. An implicit formulation is unconditionally stable numeric, it will yield a solution regardless of the size of the time step. However, it requires an iterative solution within each time step.

The solution method used in the Autodesk® CFD is segregated solver. It means the governing equations such as the continuity equation, momentum equation, energy equation or species transport equation will be solved sequentially. All cases in this study were using the unsteady Reynolds averaged Navier-Stokes (URANS) equations with turbulence model SST *k-ω*. This turbulence model is capable to capture the flow of dynamic stall as claimed by Wang et al. [42] URANS with advanced turbulence models, such as the SST k-ω model as evaluated in their research are useful for the fast design or research intension for low Reynolds number airfoils and VAWTs. Because they are capable of capturing the experimental data in a significant part of the flow dynamics. Another references [43], [44], [45], [46], [47] were

employed the numerical studies using SST k- ω turbulence model in unsteady motion. The results show that the forces and flow structures were agreed well with the experiments.

In the Autodesk® CFD guide, the turbulence model SST *k-ω* is recommended used for external aerodynamics, separated or detached flows with adverse pressure gradients. The SST models are a hybrid of the Wilcox *k-ω* and a *k-ε* model variant. The benefits of this model exhibit less sensitivity to free stream conditions (flow outside the boundary layer) than many other turbulence models. The control parameter solution in the Autodesk® CFD is SIMPLE method to approach the pressure velocity coupling. In the following section is the SST *k-ω* governing equations:

Turbulent Kinetic Energy

$$\frac{\partial k}{\partial t} + U_j \frac{\partial k}{\partial x_j} = P_k - \beta^* k \omega + \frac{\partial k}{\partial x_j}\left[(v + \sigma_k v_T)\frac{\partial k}{\partial x_j}\right] \quad (2.17)$$

Specific Dissipation Rate

$$\frac{\partial \omega}{\partial t} + U_j \frac{\partial \omega}{\partial x_j} = \alpha S^2 - \beta \omega^2 + \frac{\partial}{\partial x_j}\left[(v + \sigma_\omega v_T)\frac{\partial \omega}{\partial x_j}\right] + 2(1 - F_1)\sigma_{\omega 2}\frac{1}{\omega}\frac{\partial k}{\partial x_i}\frac{\partial \omega}{\partial x_i} \quad (2.18)$$

The finite element method described above is used directly on the diffusion and source terms. However, for numerical stability, the advection terms are treated with upwind methods along with the weighted integral method. The ADV-5 (Modified Petrov-Galerkin) scheme is chosen in the simulation. The ADV-5 is recommended for compressible flows. Beside that it has advantages such as typically produces more conservative results, ideal for recirculating and secondary flows, accurate pressure drop prediction, and has rotating and motion accuracy and stability.

The unstructured meshing was applied. Trapezoidal mesh shape was chosen in this numerical method. Close to the wing surface, 10 layers were applied to catch the flow pattern more precisely. In the following section, the mesh configuration of baseline wing was given in the Figures 2.7-2.8. The layer thickness shown in that figure has the $y^+ < 3$ for all cases. In general, the y^+ is defined as normalized distance to the wall. In the Autodesk® CFD, y^+ is defined as:

$$y^+ = \frac{\delta\sqrt{\frac{\tau_w}{\rho}}}{\upsilon} \quad (2.19)$$

, where τ_ω is the wall shear stress, ρ is the density, δ is the distance from the wall and υ is the kinematic viscosity.

To analyze the CFD results, it can be interpreted as Turbulent Intensity (TI). In the Autodesk® CFD, TI is defined as the ratio of the temporal fluctuation to the average local velocity. The TI factor controls the amount of turbulent kinetic energy in the inlet stream. Its default value is 0.05 and should rarely exceed 0.5. The expression used to calculate turbulent kinetic energy at the inlet. The turbulent kinetic energy (K) is defined as:

$$K = \frac{1}{2}\left(u^2 + v^2 + w^2\right) \tag{2.20}$$

The TI is defined as:

$$TI = \frac{u}{U} = \frac{v}{V} = \frac{w}{W} \tag{2.21}$$

, where u, v, and w are velocity components.

The growth ratio of the mesh is about 1.05 to refine the mesh generation in the outer boundary of the wing. There is a little bit differences of meshing configuration between steady and unsteady case. In the Figure 2.9 is described for steady case, but in unsteady case there is a rotational region where around this region the mesh system was set to the uniform mesh by using additional mesh region. The number of the mesh is about 10 million. Similar mesh set-up was applied on the WLE wing simulation using 10 layers. The y^+ less than 3 is keeping in all cases. Figures 2.9-2.12 show the mesh configuration on the WLE wing.

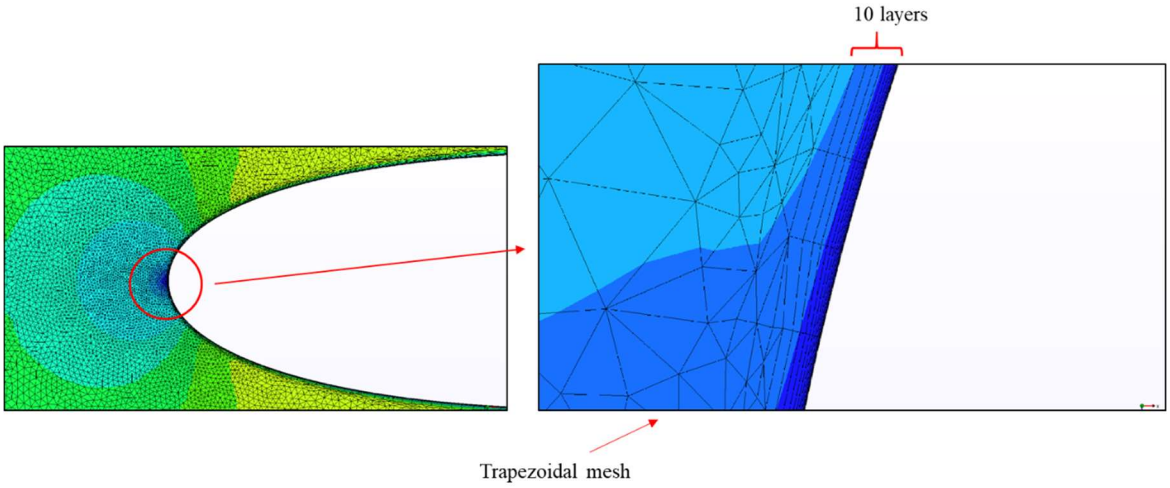

Figure 2.9 Layer thickness around the leading edge of the baseline wing

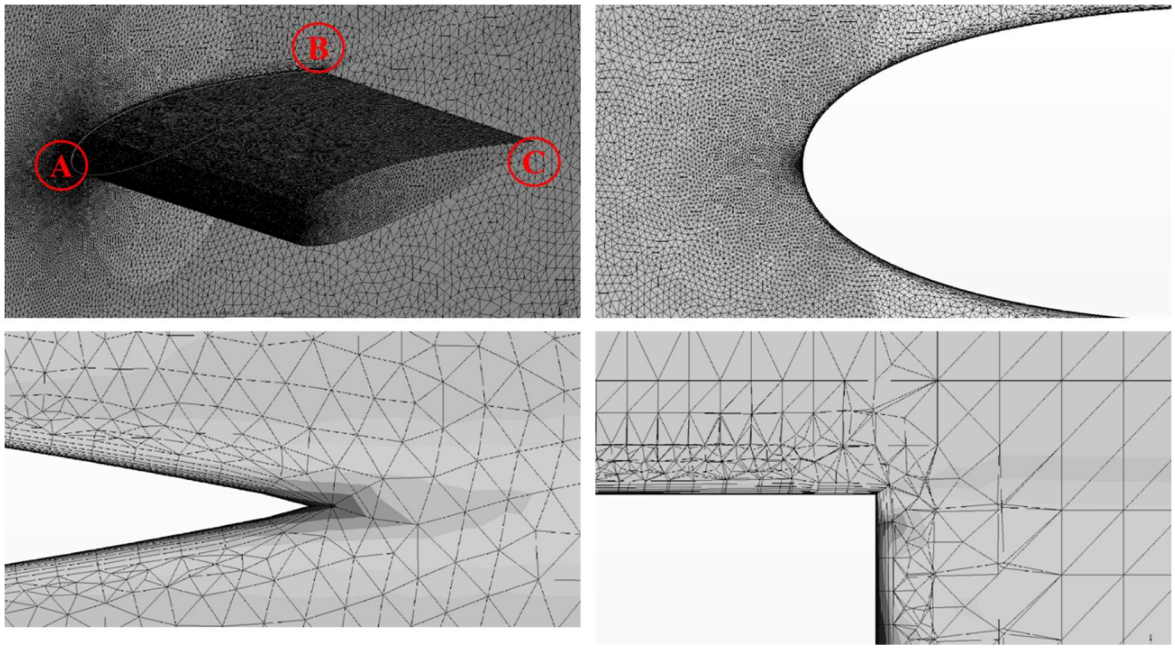

Figure 2.10 Meshing configuration for baseline wing

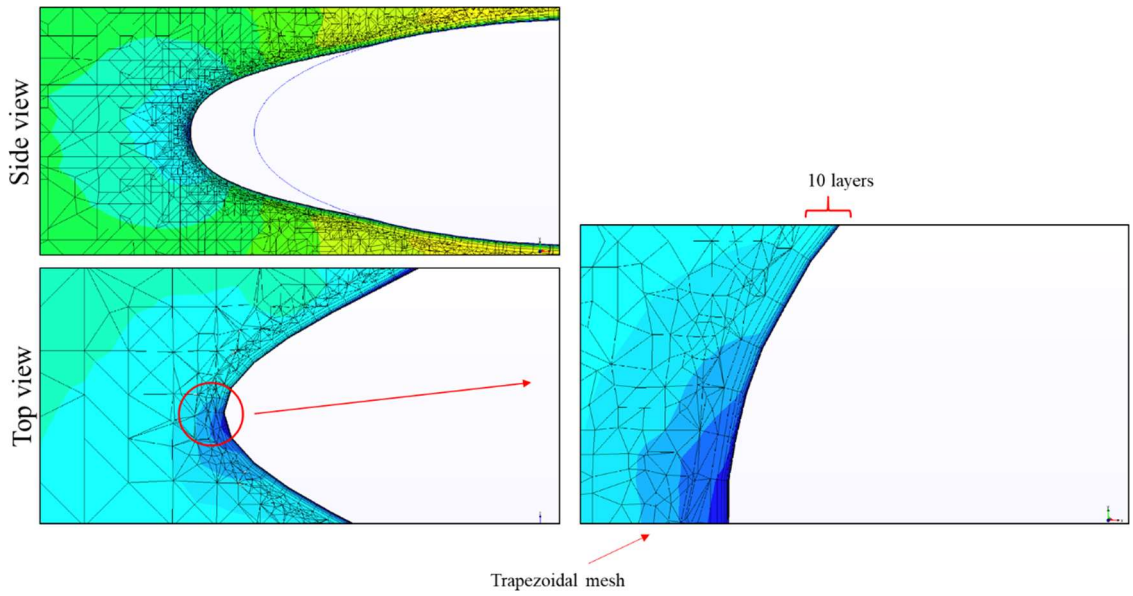

Figure 2.11 Layer thickness around the leading edge of the WLE wing

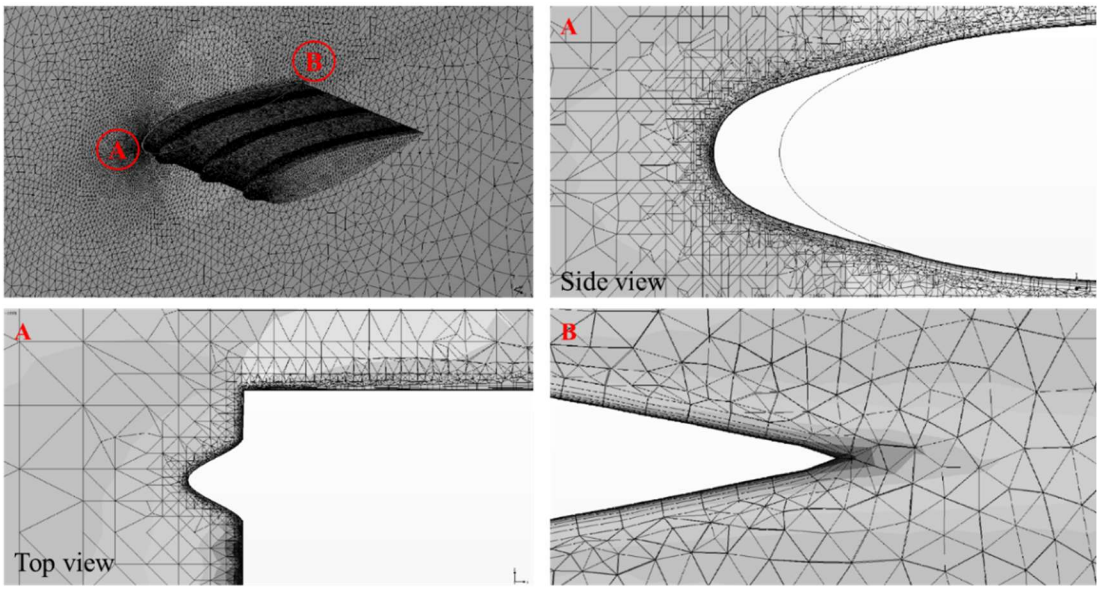

Figure 2.12 Meshing configuration for WLE wing

In the following figure was the domain simulations steady and unsteady case of aspect ratio 3.9 are given in the Figures 2.13-2.14. The dimension of the outer boundary of AR 7.9 and 9.6 are adjusted, then the blockage effect is identical. The inlet boundary condition is set as uniform velocity inlet, the outlet at the down-stream is imposed as a pressure, the other boundary conditions are imposed as the symmetry. In unsteady case, there is a rotating region which is the motion is regarding the reduced frequency i.e. $k = 0.09$, $k = 0.12$ and $k = 0.25$.

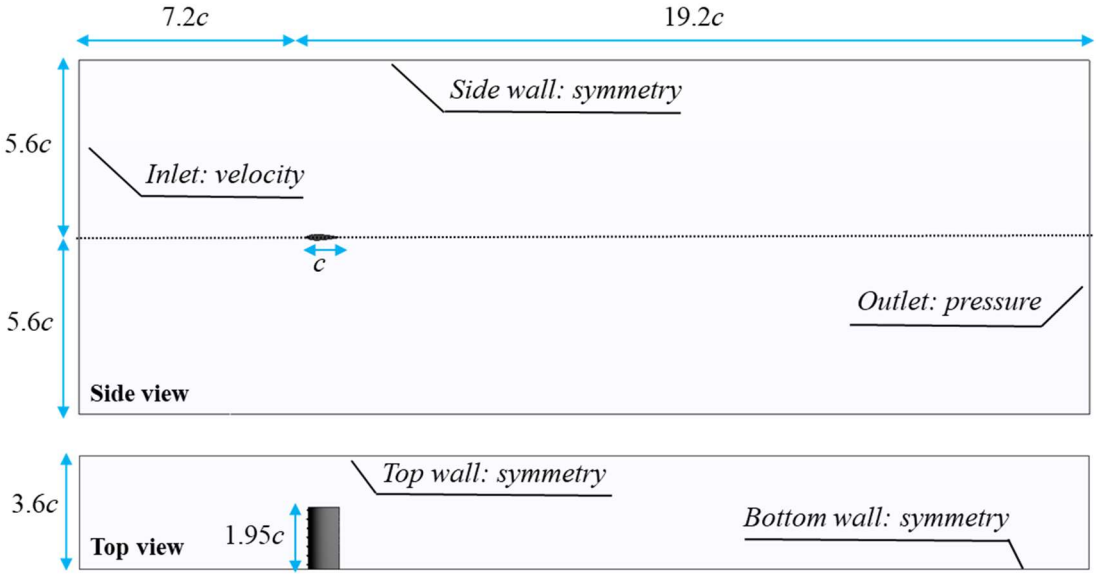

Figure 2.13 Domain simulations steady case and its boundary condition (AR 3.9)

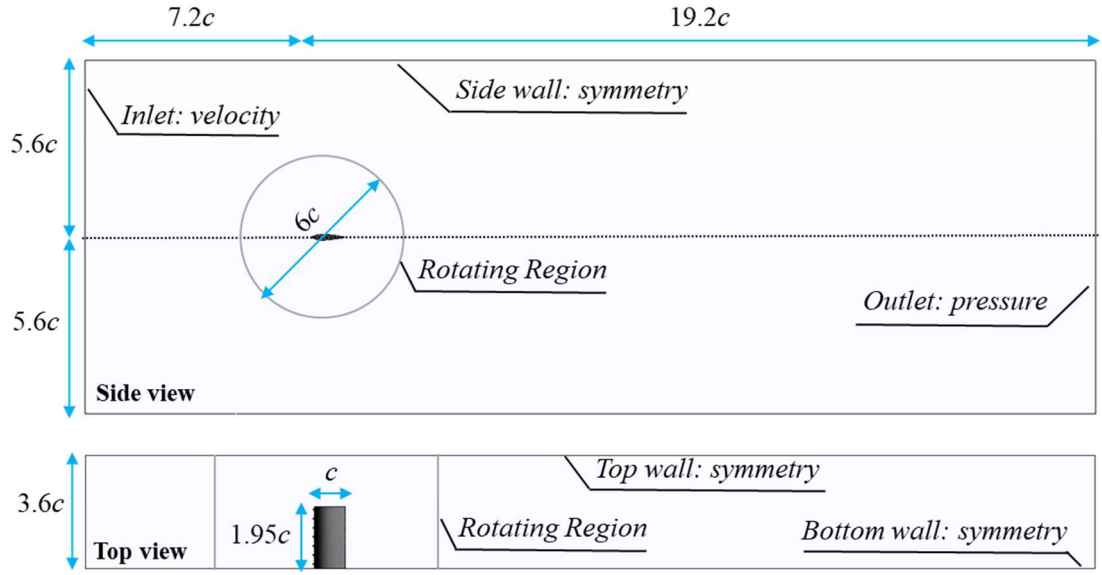

Figure 2.14 Domain simulations unsteady case and its boundary condition (AR 3.9)

The input calculation of numerical method during unsteady case is given in the next section. The calculation based on the reduced frequency was used i.e. $k = 0.09$, $k = 0.12$ and $k = 0.25$. A non-dimensional time T_0 and frequency f was calculated following the equations 2.3 and 2.4. The time step size is defined by the CFD Autodesk package with the equation as follows:

$$\text{Total travel time} = \frac{c}{v} \tag{2.22}$$

$$\text{Time step size} = \frac{1}{20} \text{ of total travel time} \tag{2.23}$$

$$\text{Number of iterations} = \frac{\text{time movement}}{\text{time step size}} \tag{2.24}$$

, where v parameter in the equation 2.18 is free-stream velocity U_0 (m/s), c is the chord length of the wing, and time movement is non dimensional time T_0.

Table 2.2 shows an example of calculation at reduced frequency $k = 0.09$ at AR 1.6 with the chord length $c = 250$ mm. By using the time step size such in the equation 2.19, it applied on the pitching motion based on the equation 2.2, we will have the input data in all variation of reduced frequencies. The input data was provided in rad/s or RPM. Table 2.3 shows an example of input data AR 1.6 at $k = 0.09$ for one cycle only. Then, the similar calculation was applied in all cases of AR in baseline and WLE wing.

Table 2.3 Input calculation of AR 1.6 at k = 0.09

Parameter	Value	Unit
v	0.8	m/s
f	0.0458	Hertz
T_0	21.8166	-
Total travel time	0.3125	-
Time step size	0.015625	s
Number of iterations	1396	-

Table 2.3 Input data of AR 1.6 at k = 0.09

Number of iterations	Sum of Time step size (s)	T_0	α (t) in (deg)	α′ (t) in (rad/s)	α′ (t) in (RPM)
1	0.0156	0.05	34.9999	-0.0001	-0.0010
2	0.0312	0.1	34.9997	-0.0002	-0.0021
3	0.0468	0.15	34.9995	-0.0003	-0.0032
.	.	.	.	.	.
.	.	.	.	.	.
.	.	.	.	.	.
1396	21.8125	69.8	34.9999	0.0001	0.0002

2.4 Summary

To understand the mechanism of fluid flow on the WLE wing, the numerical method by using Autodesk® CFD was employed in this study. As a comparison, the experimental work is given in this chapter. The NACA 0018 profile was used with and without the WLE with wavelength 8% and amplitude 5% of the chord length. In the beginning, the wing was used is in a rectangular shape. This study was performed in a steady and unsteady case with three reduced frequencies i.e., k = 0.09, 0.12, and 0.25. To get the maximum benefit of the WLE effect, this study was varied in various aspect ratios (AR) i.e., 1.6, 3.9, 5.1, 7.9, and 9.6 in baseline and WLE wing. Besides that, to approach the humpback whale flipper shape, the wing was modified into the taper wing with three taper ratios (TR) i.e., variations i.e. 0.1, 0.3, and 0.5.

CHAPTER 3
WAVY LEADING-EDGE PERFORMANCE ON THE RECTANGLE WING

In this chapter, the experimental results will be given as references. Then, the numerical results will be discussed in the last section. As comparison, the vortex generator (VG) experimental results also given to see the differences between WLE and VG effect on the wing. The wavy leading effect was discussed on the rectangle wing especially for 1.6 aspect ratio. Others aspects ratios will be discussed in the next chapter.

3.1 Experimental Results

Experimental study was conducted in steady and unsteady case for baseline and WLE wings. The baseline profile is NACA 0018 with the chord length I 250 mm. The WLE shape as mentioned in the chapter 2 has the wavelength (W) equal 8% of c with the amplitude (h) 5% of c. The standard deviation of the measured lift coefficient (Cl) and drag coefficient (Cd) are 0.027 and 0.0060, respectively, for steady case. The Cl and Cd are lift and drag coefficients normalized by the uniform flow velocity and the wing area. In unsteady case, pitching motion experiments were carried out for reduced frequencies of k = 0.09, 0.12, and 0.25. As mentioned above, the VG as vortex generator was observed to clarify the differences between VG and WLE effect on the wing. The VG or WLE is located at the leading edge. The VGs have counter-rotating vanes of height 0.016c, length 0.048c. Where the angles relative to the chord-wise direction are ±20°.

In the following figure shows a comparison of baseline wing, VG wing and WLE wing with 100-cycle phase-average of measured Cl and Cd. The measured steady results are given for comparison at reduced frequency k = 0.25. In the Figure 3.1 “up-stroke” means the angle of attack is increasing and “down-stroke” means the opposite. In steady case, the baseline and VG has similar Cl during pre-stall condition ($\alpha < 22°$). The baseline wing stall is about at the angle of attack 22.5°. A little difference with the VG wing, it has stall at the angle 23°. After stall condition, both the wings also similar tendency. This difference is quite same. Meanwhile, the stall angle of WLE wing is about 18° where the Cl is not decrease so much after stall condition. The Cl on the WLE wing has superior value comparing with the baseline and VG wing as shown in Figure 3.1.

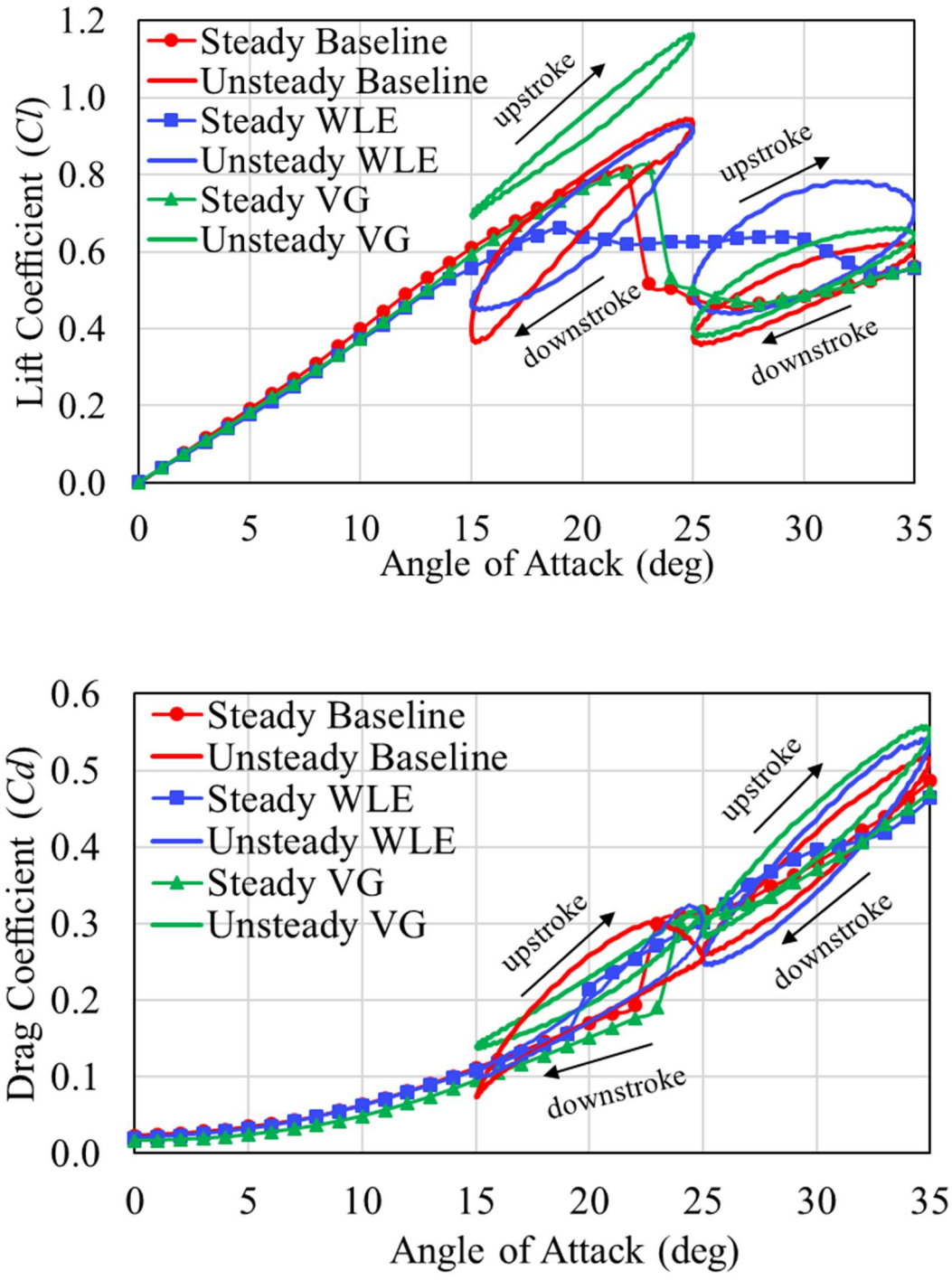

Figure 3.1 Comparison of Baseline, VG and WLE wing results at $k = 0.25$

Next, see the unsteady case results as shown in the Figure 3.1 where there are two range of angles i.e. during pre-stall condition ($15° \leq \alpha \leq 25°$) and after stall condition ($25° \leq \alpha \leq 35°$). During pre-stall condition, the VG has superior *Cl* comparing the baseline and WLE wing. Meanwhile, after stall condition the WLE has the prior *Cl* among both wings. It means, the WLE wing is able to acquire higher *Cl* than that of VG or baseline wing at the post-stall condition. As to *Cd*, the drag increase is found to be less than the lift increase. At the post-stall region, WLE is effective to suppress the dynamic stall. The benefit of WLE effect seem better after stall condition, therefore this research is focused on the post-stall condition. It may be interesting if the WLE can be applied in some application operated at the deep-stall condition such as fin stabilizer or wind turbines. Table 3.1 shows comparison of the ratio of $Cl_{VG}/Cl_{Baseline}$ and $Cd_{VG}/Cd_{Baseline}$ at 30°↑ and 30°↓, where Cl_{VG} denotes *Cl* of VG wing and Cd_{VG} denotes *Cd* of VG wing.

Table 3.1 Ratio of forces at $k = 0.25$ in between baseline wing and VG wing

Ratio	30°↑	30°↓
$\frac{Cl_{VG}}{Cl_{Baseline}}$	1.08	1.04
$\frac{Cd_{VG}}{Cd_{Baseline}}$	1.07	1.11

$$\frac{Cl_{VG\ 30°\uparrow}}{Cl_{Baseline\ 30°\uparrow}} < \frac{Cl_{WLE\ 30°\uparrow}}{Cl_{Baseline\ 30°\uparrow}}, \text{ and}$$

$$\frac{Cd_{VG\ 30°\uparrow}}{Cd_{Baseline\ 30°\uparrow}} > \frac{Cd_{WLE\ 30°\uparrow}}{Cd_{Baseline\ 30°\uparrow}}.$$

A similar trend is seen at the three reduced frequencies. In more detail, high frequency pitching WLE wing can increase the maximum lift compared to the lower frequency motion. In the post-stall region, the *Cl* of WLE wing is higher than baseline wing. The trend of *Cl* increase differs between the up-stroke process and the down-stroke process. Table 3.2 shows the *Cl* and *Cd* at 30° for up-stroke motion (30°↑) and 30° for down-stroke motion (30°↓) for baseline wing and WLE wing at reduced frequency k = 0.25. Table 3.3 shows the ratio of "$Cl_{WLE}/Cl_{Baseline}$", where Cl_{WLE} denotes *Cl* of WLE wing and $Cl_{Baseline}$ denotes *Cl* of baseline wing at reduced frequency $k = 0.25$. The same denotation is given for *Cd*.

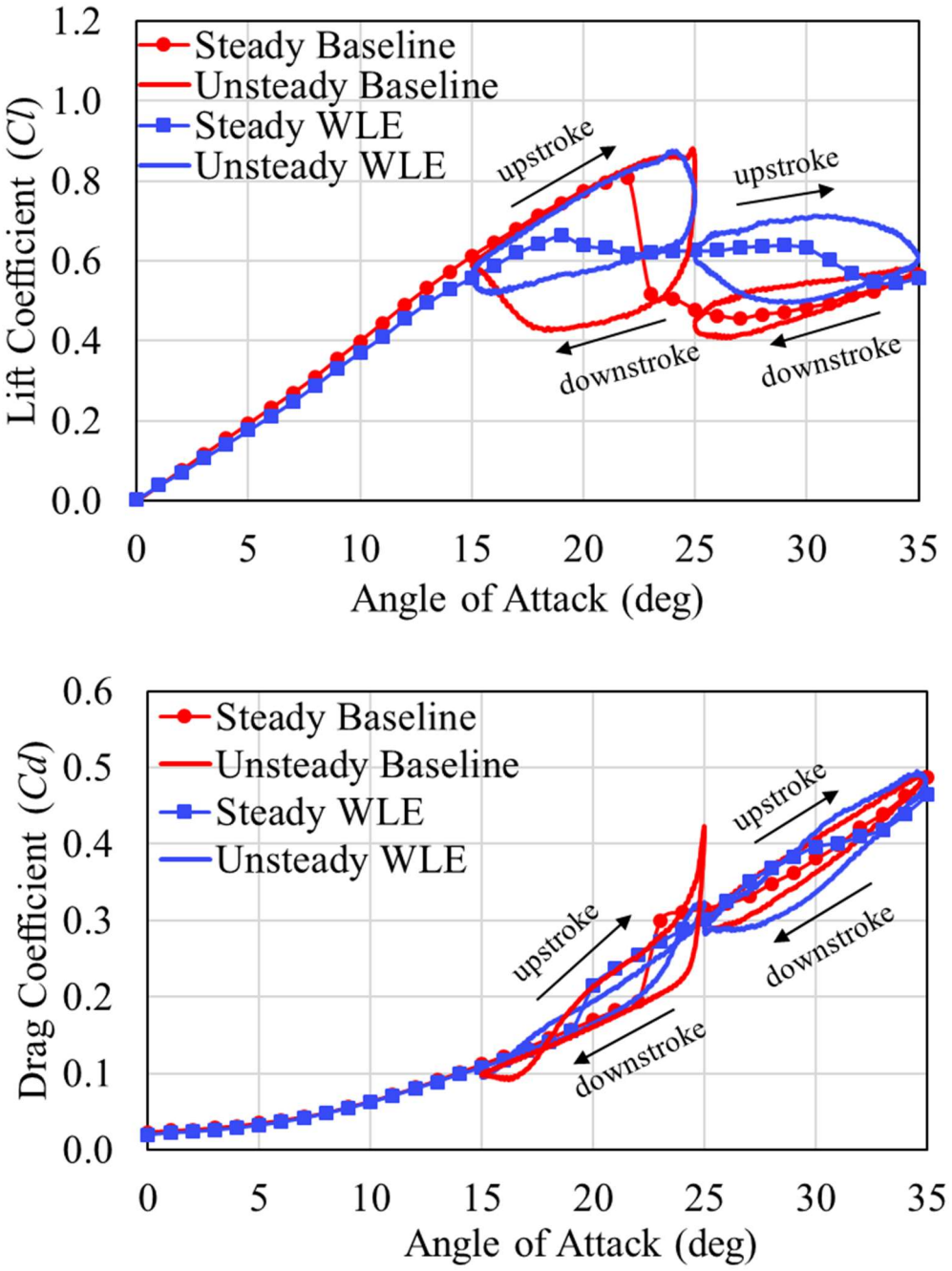

Figure 3.2 Baseline and WLE wing results at $k = 0.09$

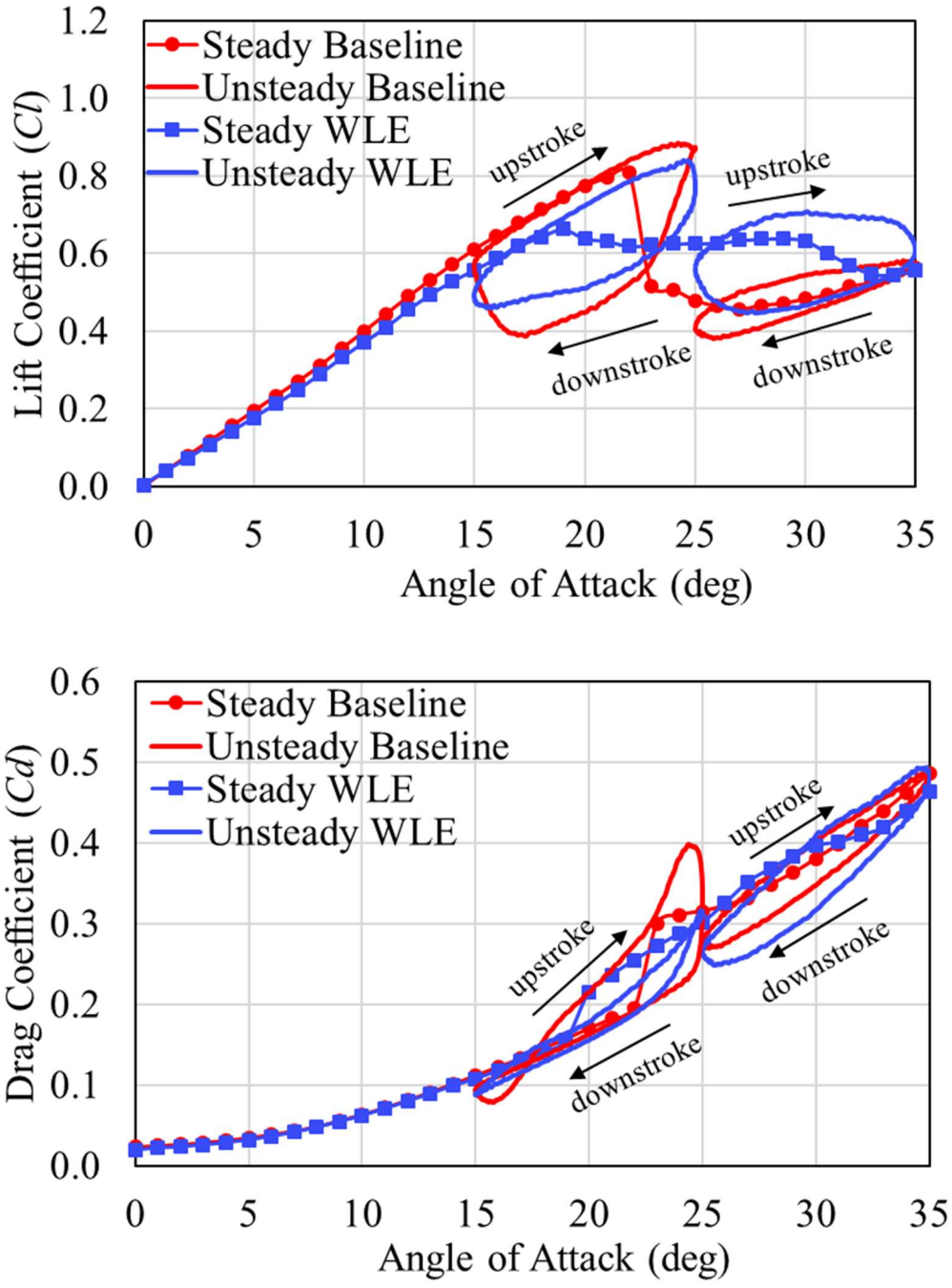

Figure 3.3 Baseline and WLE wing results at $k = 0.12$

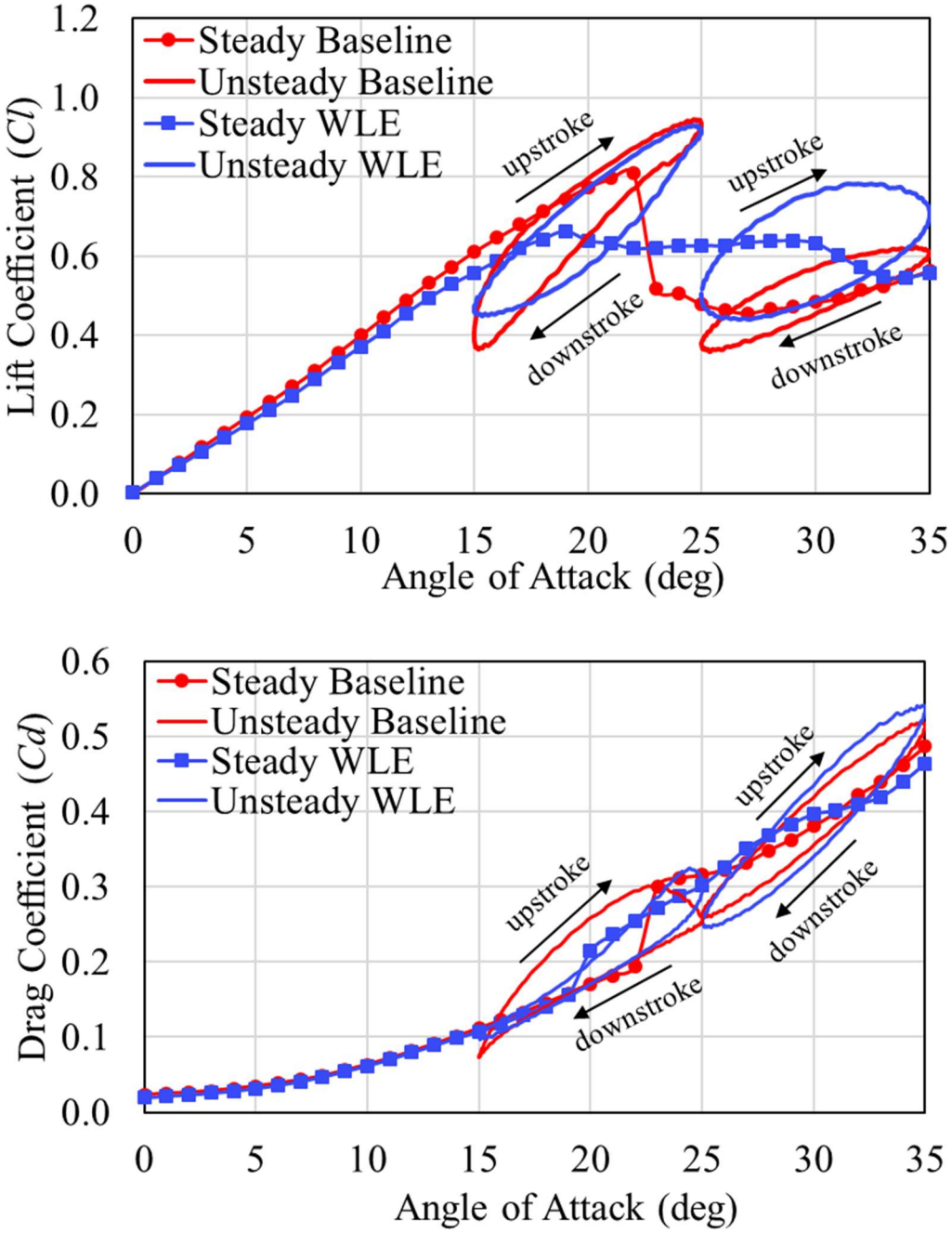

Figure 3.4 Baseline and WLE wing results at $k = 0.25$

Table 3.2 *Cl* and *Cd* at 30° for $k = 0.25$ in Experiment

Wing type	30°↑		30°↓	
	Cl	*Cd*	*Cl*	*Cd*
Baseline	0.57	0.43	0.46	0.35
WLE	0.76	0.44	0.49	0.34

Table 3.3 Ratio of forces at $k = 0.25$ in between baseline wing and WLE wing

Ratio	30°↑	30°↓
$\frac{Cl_{WLE}}{Cl_{Baseline}}$	1.33	1.07
$\frac{Cd_{WLE}}{Cd_{Baseline}}$	1.02	0.98

Here, we get:

$$\frac{Cl_{WLE\ 30°\uparrow}}{Cl_{Baseline\ 30°\uparrow}} > \frac{Cl_{WLE\ 30°\downarrow}}{Cl_{Baseline\ 30°\downarrow}} > 1.$$

It is clarified that the ratio of $Cl_{WLE}/Cl_{Baseline}$ is higher at upstroke motion than the down-stroke motion. It can be seen that the lift increase by WLE is more effective in up-stroke motion than down-stroke motion. Meanwhile, we get the followings for $Cd_{WLE}/Cd_{Baseline}$ ratio,

$$\frac{Cl_{WLE\ 30°\uparrow}}{Cl_{Baseline\ 30°\uparrow}} > \frac{Cd_{WLE\ 30°\uparrow}}{Cd_{Baseline\ 30°\uparrow}}, \text{ and}$$

$$\frac{Cl_{WLE\ 30°\downarrow}}{Cl_{Baseline\ 30°\downarrow}} > \frac{Cd_{WLE\ 30°\downarrow}}{Cd_{Baseline\ 30°\downarrow}}.$$

It is clarified quantitatively that the drag increase is found to be less than the lift increase. WLE is effective to suppress the dynamic stall at the post-stall region.

$$\frac{Cl_{VG\ 30°\uparrow}}{Cl_{Baseline\ 30°\uparrow}} < \frac{Cl_{WLE\ 30°\uparrow}}{Cl_{Baseline\ 30°\uparrow}}, \text{ and}$$

$$\frac{Cd_{VG\ 30°\uparrow}}{Cd_{Baseline\ 30°\uparrow}} > \frac{Cd_{WLE\ 30°\uparrow}}{Cd_{Baseline\ 30°\uparrow}}.$$

The ratio of $Cl_{VG}/Cl_{Baseline}$ is lower than $Cl_{WLE}/Cl_{Baseline}$ at both up-stroke and down-stroke motion. And the ratio of $Cd_{VG}/Cd_{Baseline}$ is larger than $Cd_{WLE}/Cd_{Baseline}$ also at both up-stroke and down-stroke motion. So that, it indicates that VG wing is not effective to suppress the dynamic stall, compared with WLE wing at the post-stall region. Meanwhile, VG wing at pre-stall region has higher *Cl* compared with Baseline and WLE wing. Based on the lift coefficient ratio analysis between baseline wing, VG wing and WLE wing as shown in the Table 3.1 and 3.3, proven that the VG wing has higher drag coefficient. This fact affects the efficiency on the wing. In Table 3.4 shows the comparison of advantages and disadvantages of VG and WLE as turbulent generator in steady and unsteady cases based on Figure 3.1.

Table 3.4 Comparison of Baseline, VG, and WLE wing in steady and unsteady cases

Case	Baseline wing	VG wing	WLE wing
Steady	• The maximum *Cl* was at $\alpha \approx 22°$ • The *Cl* decrease at $\alpha > 23°$	• The maximum *Cl* was at $\alpha \approx 23°$ (able to delay stall angle) • Has the same *Cl* tendencies after stall condition	• The maximum *Cl* was at $\alpha \approx 19°$ (earliest stall) • After stall condition, the *Cl* able to acquire
Unsteady	• During pre-stall condition ($15° \leq \alpha \leq 25°$), the ranges of *Cl* was $0.38 \leq Cl \leq 0.9$ • After stall condition ($25° \leq \alpha \leq 35°$), the ranges of *Cl* was $0.4 \leq Cl \leq 0.6$	• During pre-stall condition, the range of *Cl* was $0.7 \leq Cl \leq 1.18$ (has favorable value) • In *Cd* distribution, the VG has highest *VG* compared to the baseline and WLE wings	• During pre-stall condition, the tendency was similar with the baseline wing • Has the highest *Cl* compared to the baseline and VG wings

Three reduced frequencies were selected $k = 0.09$, $k = 0.12$, and $k = 0.25$ by considering the ship stabilizers of a RORO ship. The following table shows the *Cl* for 2 mean angles at 20° and 30°. In the Figure 3.5, it can be seen that highest *Cl* is accomplished by reduced frequency $k =$

0.25 for both wings. Since the results of WLE wing at post-stall region ($\alpha > 21°$) has favorable values than baseline wing, numerical methods only focused on the range angle of attack $25° \leq \alpha \leq 35°$.

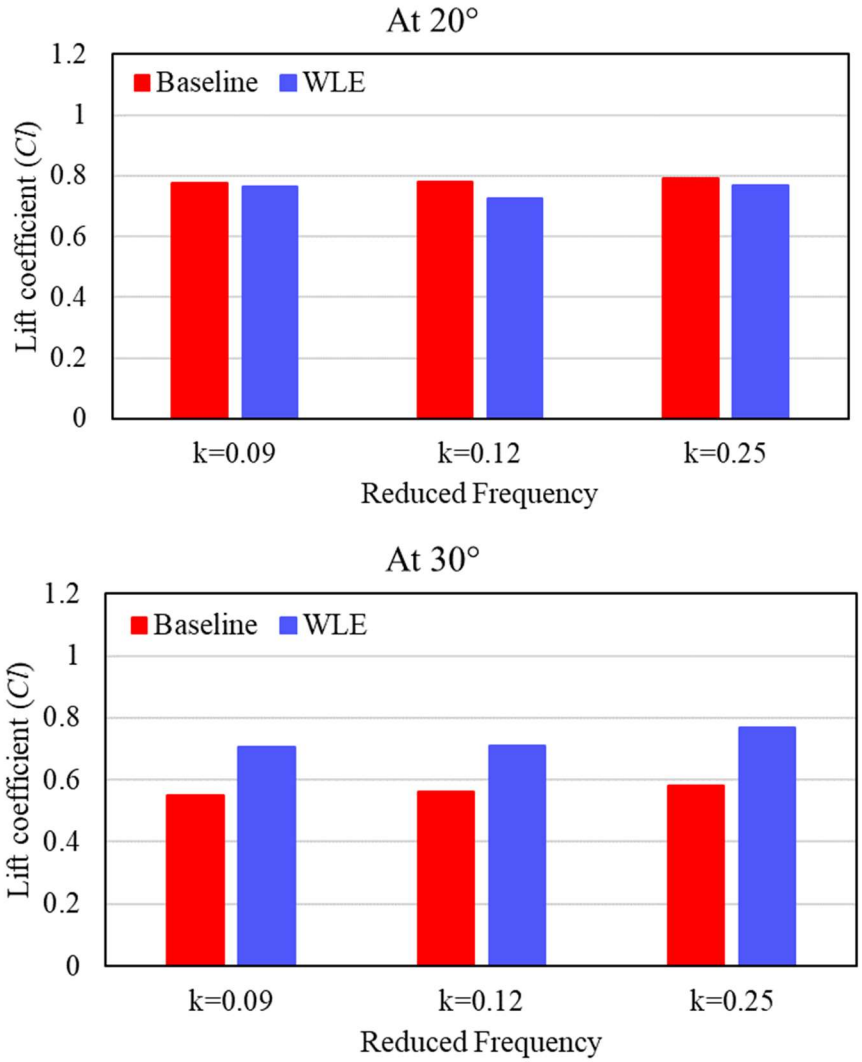

Figure 3.5 Comparison of *Cl* at 20° and 30° at three reduced frequencies

Keep in mind to find out the best wing between the baseline, VG, and WLE wing, the ratio analysis has been employed as mentioned above. The VG wing has higher ratio in *Cd* compared to the WLE wing in the post-stall region. It indicates that, the VG is not effective to reduce the *Cd* in the post-stall region. Besides that, the VG wing is similar to the baseline wing which is unable to acquire the *Cl* after stall condition. In this study, the analysis only focused on the range angle of attack $25° \leq \alpha \leq 35°$ (post-stall region). A consideration based on this analysis, the WLE wing is better than the VG wing in this case.

3.2 Validity with Experimental Data

The CFD simulation is chosen in the study to approach the experimental results. There are several benefits using CFD simulation such as predicting forces acting on the wing with mathematical model, static pressure pattern, $y+$, helicity and else. To determine the accuracy of the CFD results, it validated with the experimental results. Arai et al. [15] conducted experimental study using water channel. Furthermore, the experimental results are used as a comparison of CFD results.

To establish the accuracy of the CFD simulation and keep the low cost computation, the mesh independence study is needed. The mesh convergence study was performed by developing three different meshes with coarse, medium and fine mesh. The lift and drag coefficients were explored to determine how the mesh quality affects the CFD simulation results. Three cases simulated using SST k-ω turbulence model which has the y+ less than 3. Due to the numerical method were conducted in steady and unsteady cases, the validity of numerical methods also conducted in two methods (steady and unsteady validation). Table 3.4 below was steady case validation at the angle of attack 25°. The value of % error was calculated the deviation each type of mesh with the value of experimental results. In that table, the experimental value was denoted as "Exp". Based on % error of *Cl* results, the medium mesh type was chosen for further numerical method in steady case.

Table 3.4 Validation of steady case at angle of attack 25°

	Baseline		**Ratio number of mesh**
	Cl	**% error**	
Exp	0.4806	-	-
Coarse	0.4903	2.018	1
Medium	0.4912	2.195	2
Fine	0.4905	2.062	4

Meanwhile, the validation of unsteady case is given in the Table 3.5. The lift and drag coefficient are shown in Fig. 3.6. Three types mesh is in good agreement with the experimental data, especially for the drag coefficient. The lift coefficient of coarse and medium mesh lower than the experimental data. It means that the fine mesh type has the best performance. To evaluate the grid independency each type of the mesh, the deviation of lift coefficient and drag

coefficient are calculated as Table 3.6. The % error is calculated comparing with *Cl* value of experimental result at the angle of attack 25°. The optimum grid independence study based on % error value is the medium mesh. The medium mesh type is chosen for the next numerical unsteady case.

Table 3.5 Number of Mesh and Ratio

Mesh type	Number of Mesh	Ratio
Coarse	574,343	1
Medium	1,079,044	2
Fine	2,886,453	6

Table 3.6 % Error of the grid independency

Mesh type	% *Cl*	% *Cd*
Coarse	2.31	3.05
Medium	0.43	2.45
Fine	1.77	1.32

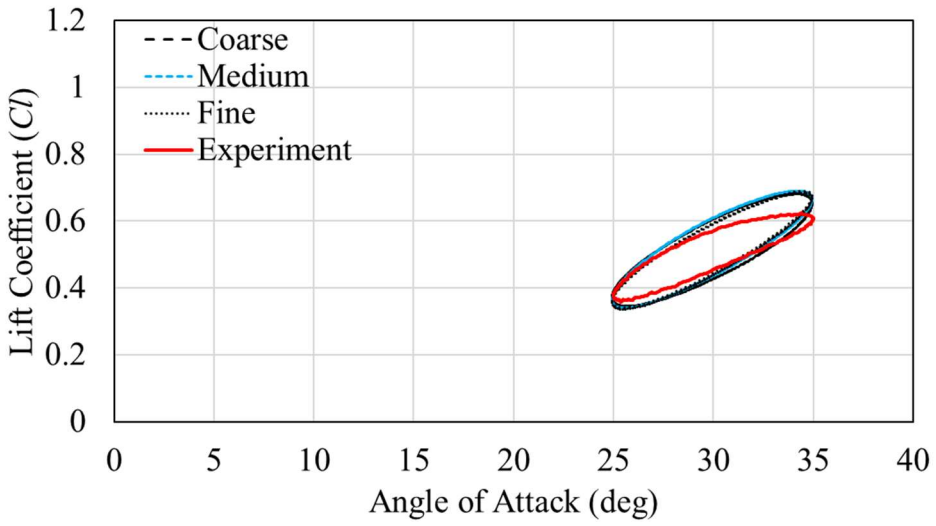

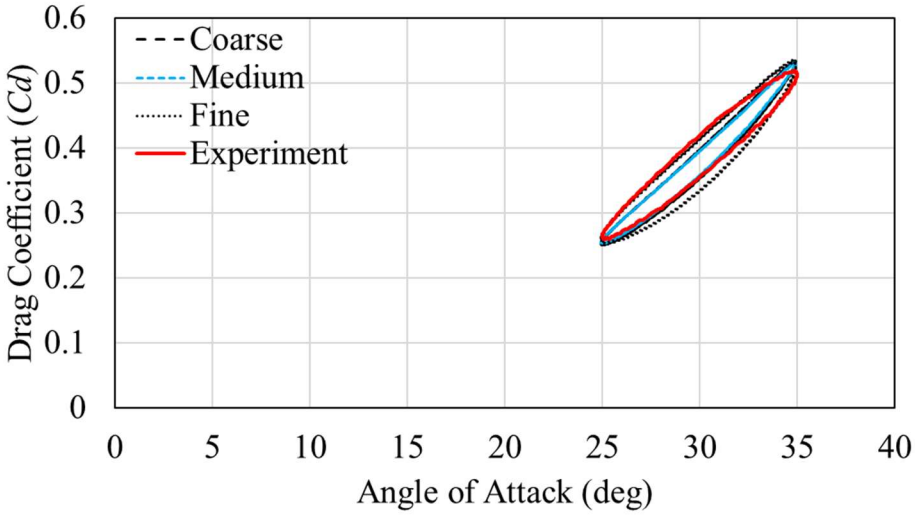

Figure 3.6 Comparison of *Cl* and *Cd* for differences meshes

3.3 Numerical Results

3.3.1 Steady Case

Figures 3.7-3.8 show the lift coefficient and drag coefficient of steady CFD results of the wing with AR 1.6. The tendencies of the results are quite good following the experimental results for *Cl* and *Cd*. The WLE wing after stall condition has prior *Cl* comparing the baseline wing. This phenomenon will be discussed clearly on the unsteady case in the next section.

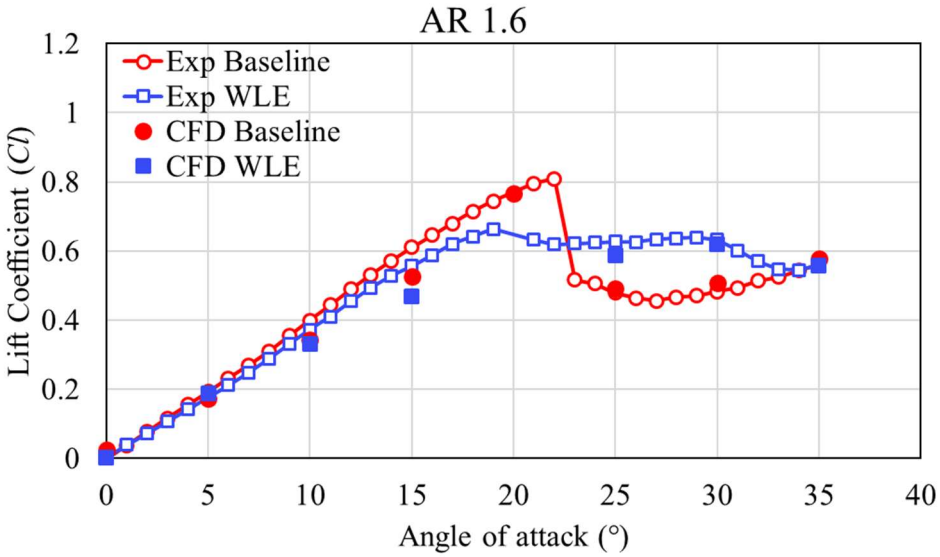

Figure 3.7 Lift coefficient (*Cl*) of steady case at AR 1.6

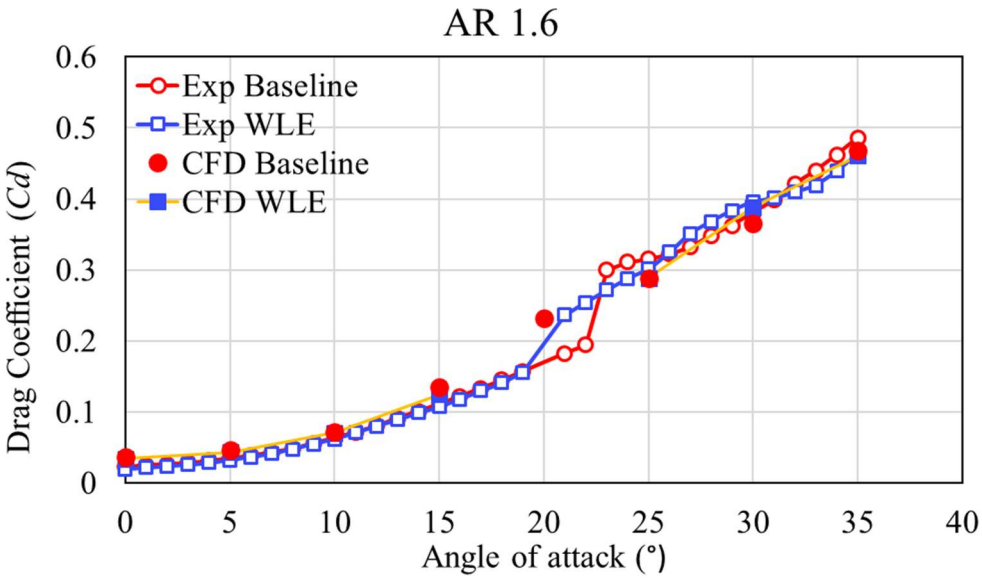

Figure 3.8 Drag coefficient (*Cd*) of steady case at AR 1.6

3.3.2 Unsteady Case

In this section, the unsteady method was conducted with three types of reduced frequencies (k = 0.09; k = 0.12; and k = 0.25). The reduced frequency was inspired with fin stabilizer of a RORO ship with k = 0.1. Figures 3.9-3.11 show the comparison between calculated unsteady results for baseline wing and WLE wing at k = 0.09, k = 0.12 and k = 0.25, respectively. Experimental and numerical results are denoted as "Exp" and "CFD", respectively. Similar to the facts seen in the experimental results, the calculated results show that at the post-stall region, *Cl* by WLE wing tends to be greater than *Cl* of baseline wing. The increase in *Cl* by WLE wing tends to be greater in the up-stroke process than in the down-stroke process. The tendencies of *Cd* are quite good for three types of reduced frequencies but *Cl* value is not as good as *Cd* value. Similar trend was found only at reduced frequency k = 0.25 but there is still 53discrepancy between experimental and CFD results. This discrepancy will be discussed in the next section.

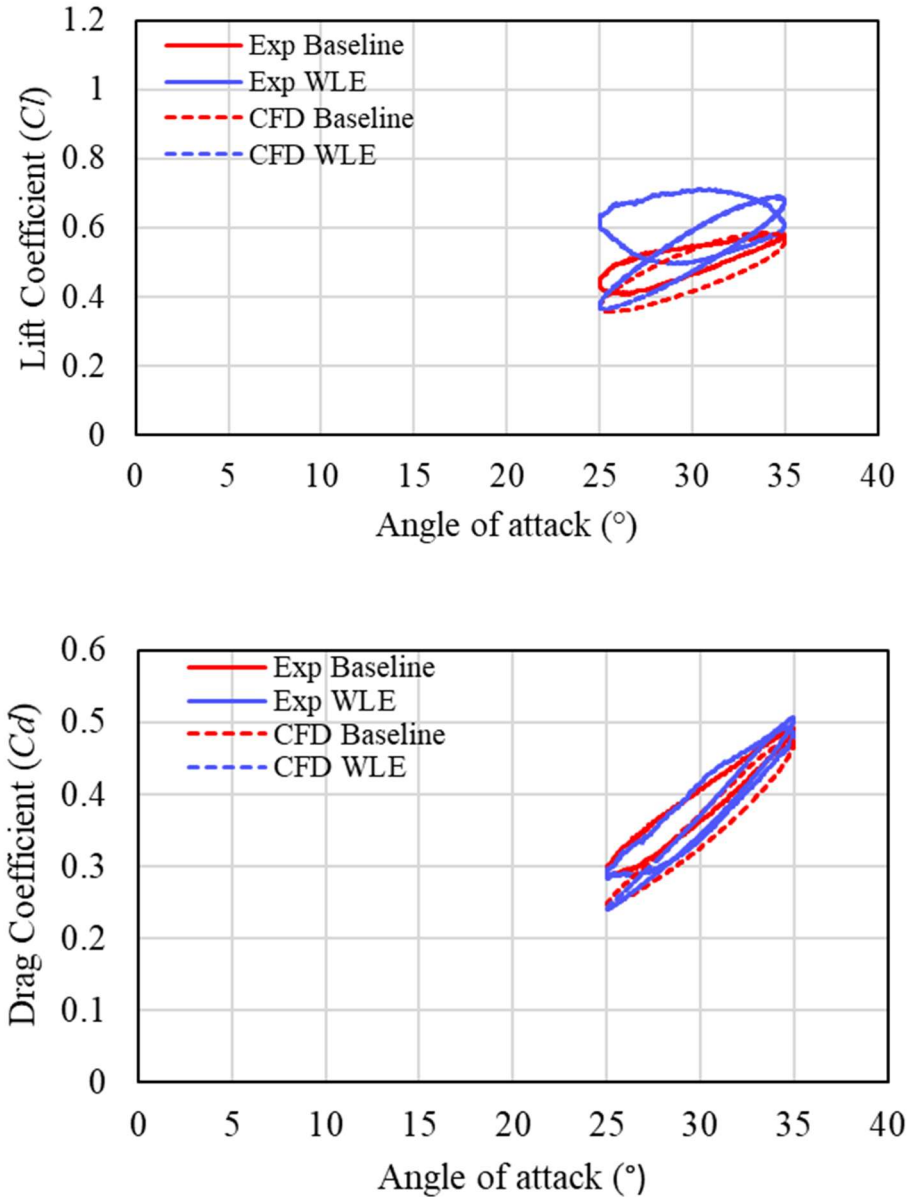

Figure 3.9 Lift and drag coefficient results at $k = 0.09$

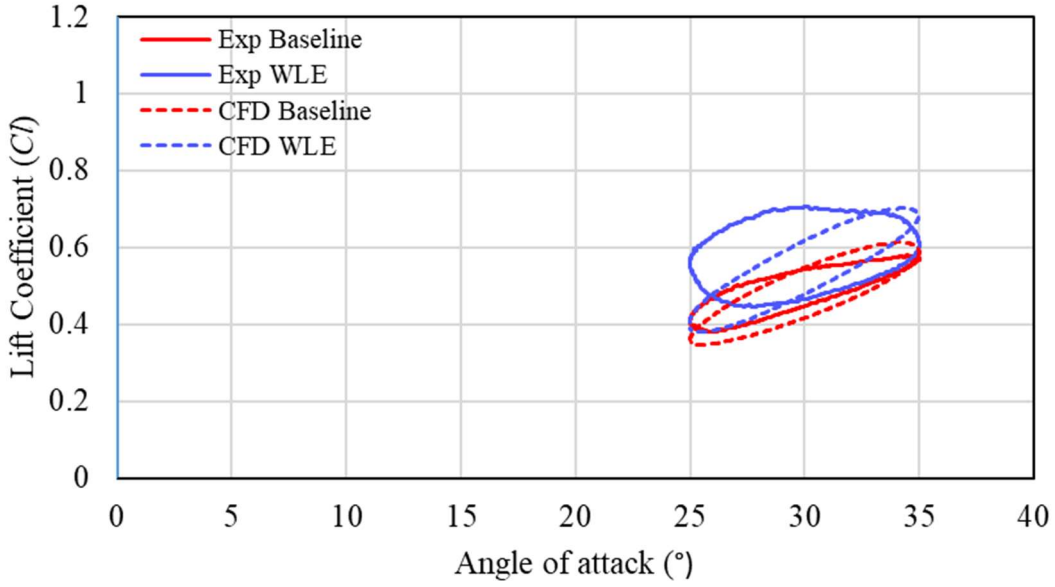

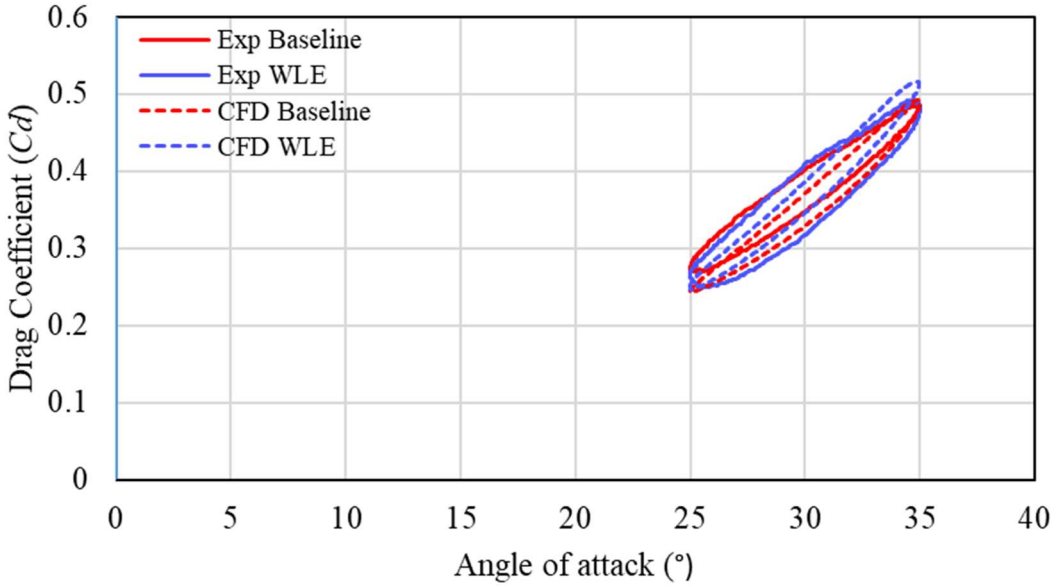

Figure 3.10 Lift and drag coefficient results at $k = 0.12$

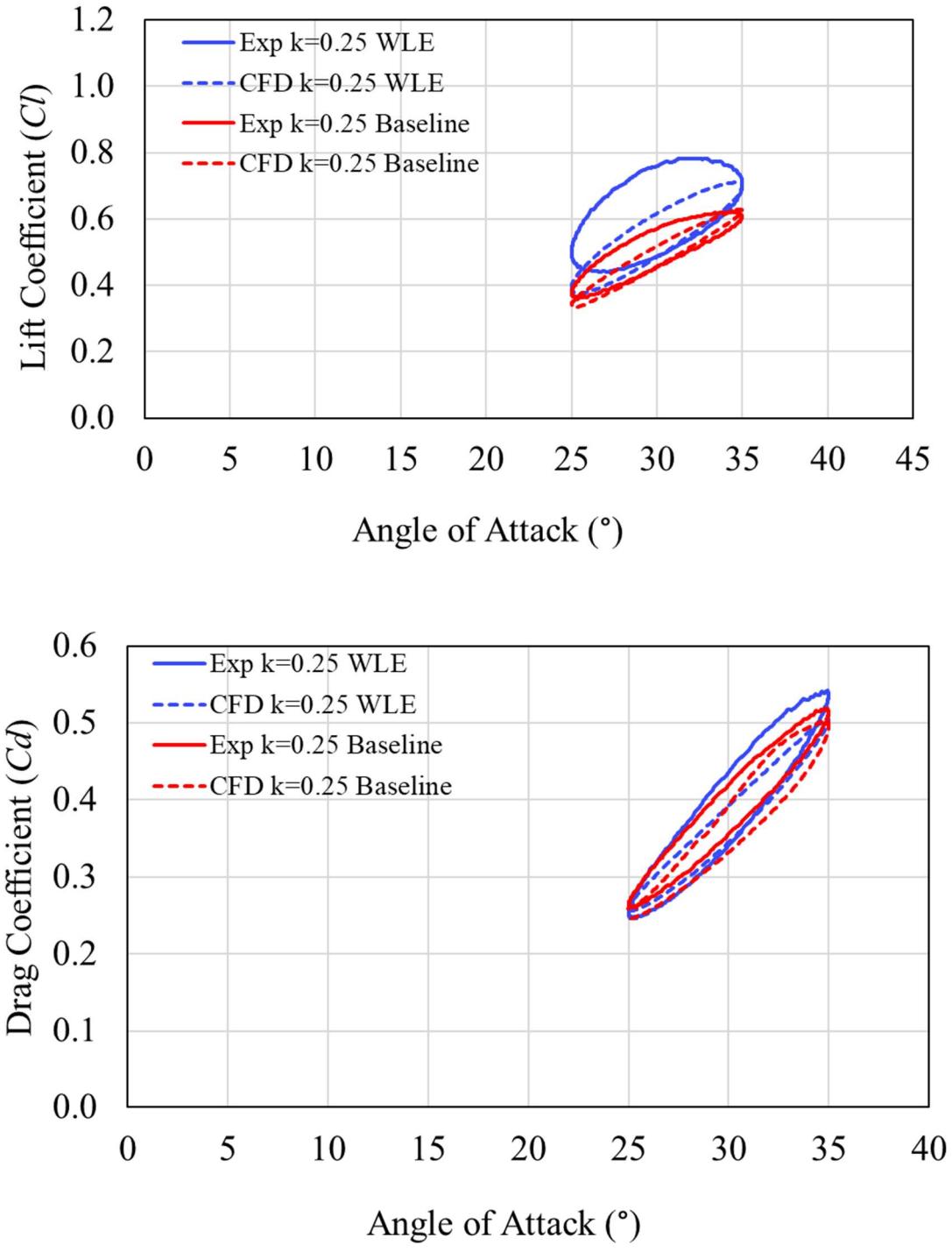

Figure 3.11 Lift and drag coefficient results at $k = 0.25$

Figure 3.12 shows the comparison of the ratio of Cl_{WLE}/Cl_{Base} at 30° up-stroke (30°↑) and 30° down-stroke (30°↓). The same denotation is given for Cd_{WLE}/Cd_{Base}. The trends of Cl_{WLE}/Cl_{Base} and Cd_{WLE}/Cd_{Base} observed in the experimental results are shown in the numerical results. The improvement of the lift force in the upstroke motion is remarkable more than that of down-stroke motion. The increase in drag due to WLE is not significant and the increase is less than the lift increase.

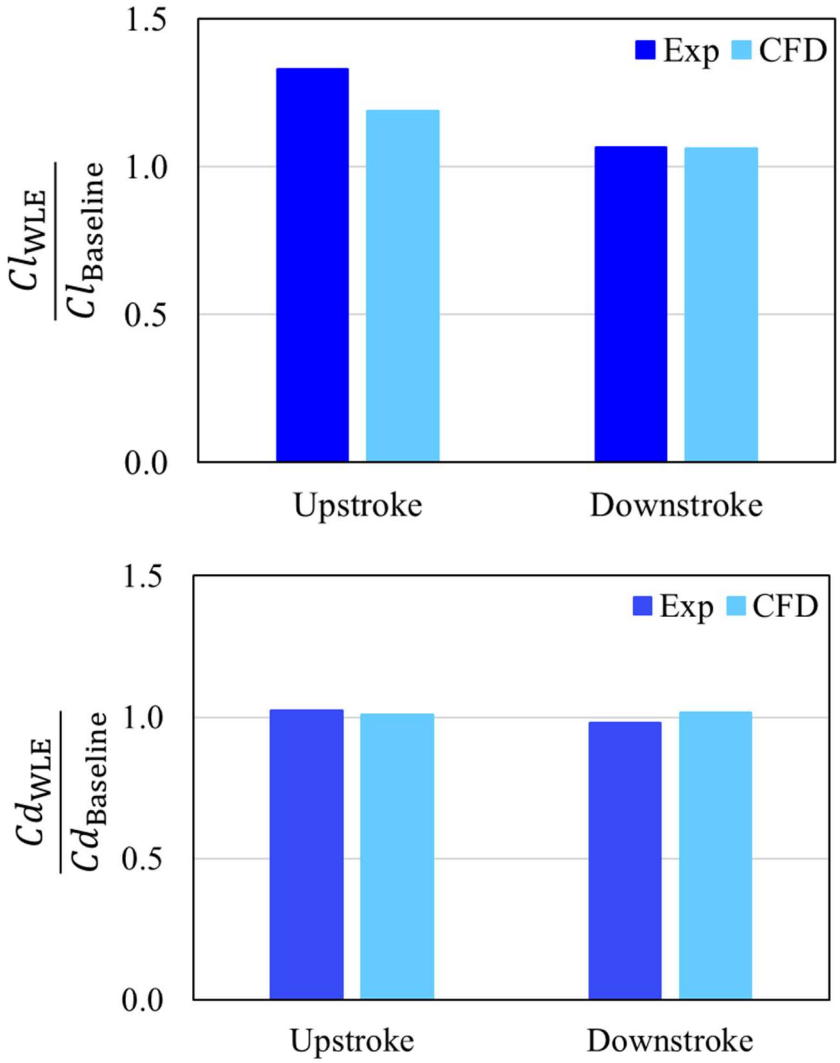

Figure 3.12 Lift and drag coefficient ratio analysis at 30°

In order to investigate the difference in trend between up-stroke and down-stroke motion, distributions of pressure coefficient (Cp) are compared. Here, Cp is normalized by the uniform flow velocity. Figures 3.13-3.15 show the instantaneous of Cp distribution on the suction side of the wing at 30° up-stroke (30°↑) and 30° down-stroke (30°↓) at reduced frequency $k = 0.09$, $k = 0.12$ and $k = 0.25$, respectively. The symmetry plane is given as SP. A significant differences

of *Cp* distribution among three reduced frequencies in these figures is the lower pressure area were found during the upstroke motion in both wings. The lower pressure area was found in the leading-edge area. It indicates that the fluid was easier flowing through its area compared to the downstroke motion. In the left side of these figures, the deep blue color represents the low pressure compared to the surrounding area. At the upstroke motion, the lower pressure is wider than the down-stroke motion. It can be seen that the pressure on the suction side of WLE wing is lower in the upstroke motion than in the down-stroke motion. Due to the pressure distribution around the leading edge, the *Cl* at upstroke motion is higher than the down-stroke motion.

In these figures, the WLE wing has favorable area wider than the baseline wing. Wider favorable area was found while increasing the reduced frequency from $k = 0.09$ to $k = 0.25$. The reduced frequency $k = 0.25$ is better to analyze the differences during upstroke and downstroke motion. Then, the next section only focused on reduced frequency $k = 0.25$.

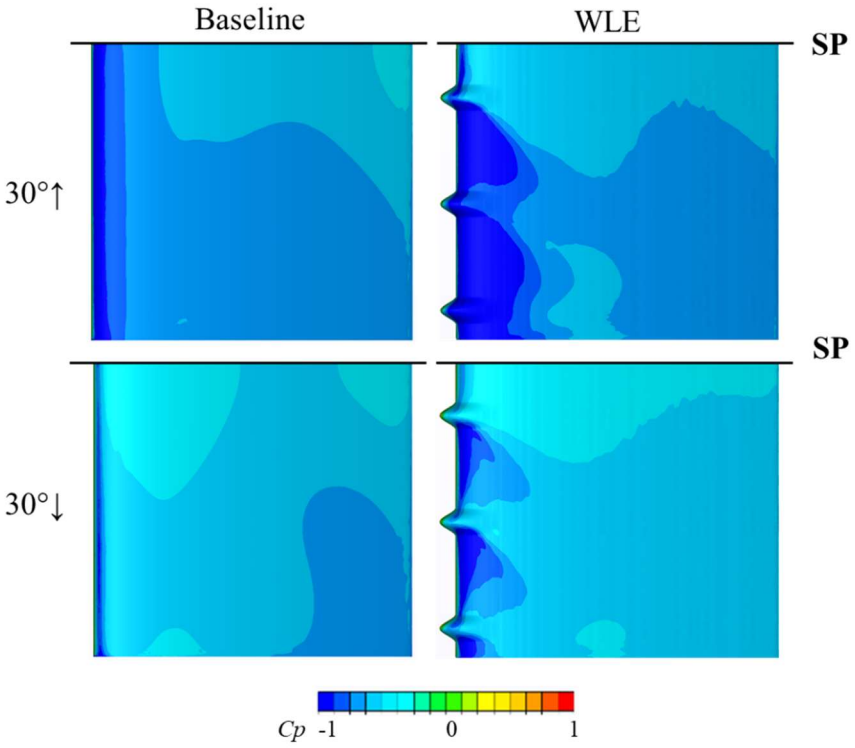

Figure 3.13 Pressure coefficient (*Cp*) at α=30°, $k = 0.09$

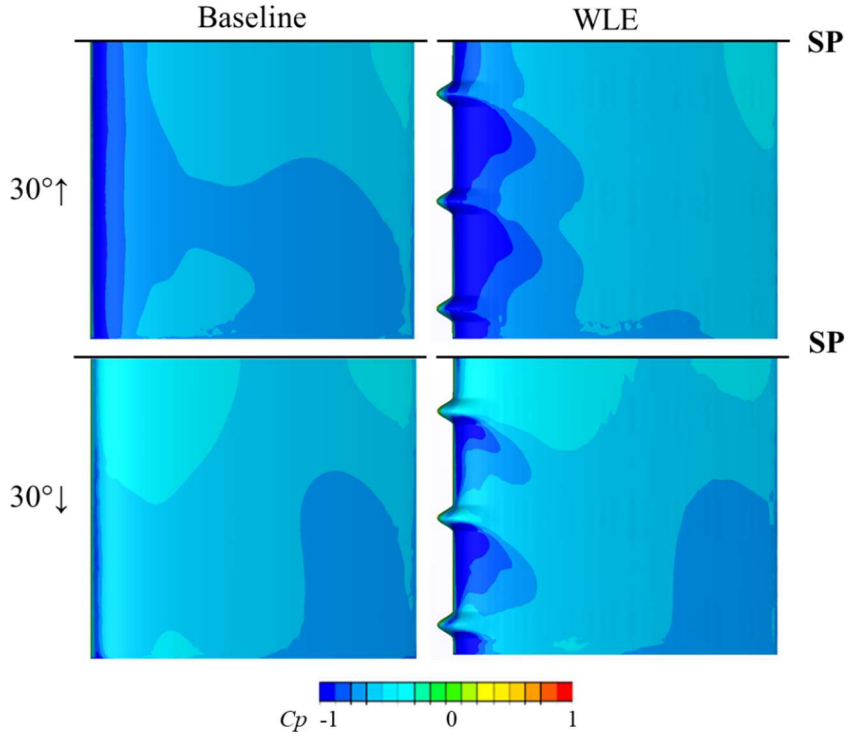

Figure 3.14 Pressure coefficient (*Cp*) at α=30°, *k* = 0.12

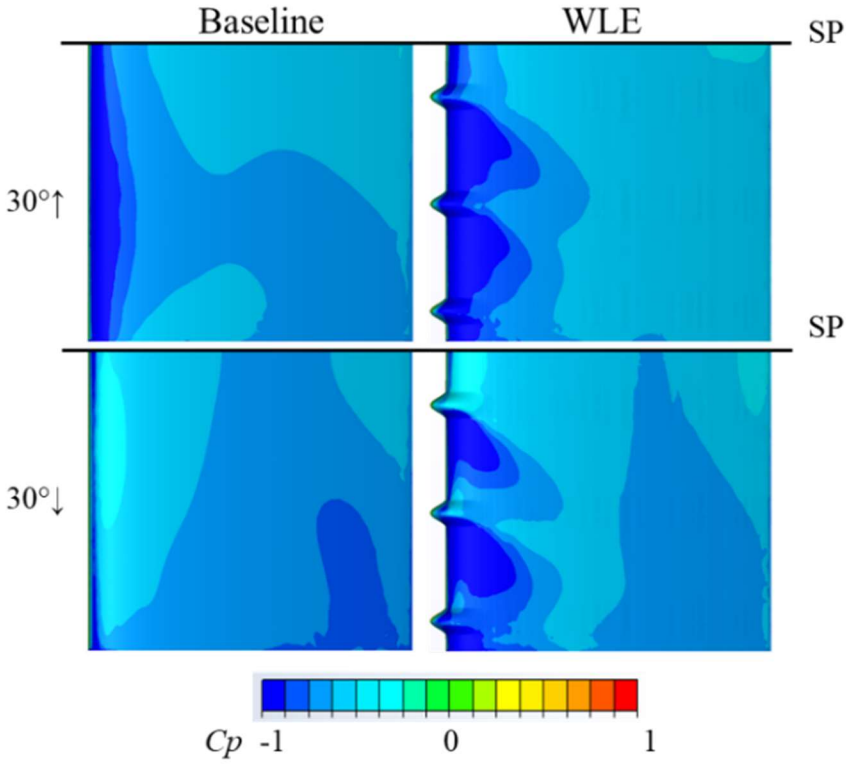

Figure 3.15 Pressure coefficient (*Cp*) at α=30°, *k* = 0.25

Figures 3.16-3.18 shows the velocity distribution on *y-z* plane taken from side view at each angle of attack. The *y-z* plane is located at z = 0.29*c* for reduced frequency k = 0.09, 0.12 and 0.25, respectively. In these figures, a streamline is drawn to make clear the flow pattern around the leading edge. The velocity distribution of baseline wing and WLE wing are given in the left and right side, respectively. The separated area can be compared based on how the streamlines divide. The streamline of WLE wing is closer to the wing surface than baseline wing.

On the WLE wing, the flow is capable to attach the wing surface. Furthermore, there is a stagnant flow shown as deep blue on the suction side of the wing. Both baseline and WLE wings, the stagnant flow is greater in the down-stroke motion than the upstroke motion. In case of WLE wing, the stagnant flow at the suction side of the wing is suppressed compared to baseline wing. As comparison, the velocity distribution on *y-z* plane at z = 0.319 c were given in the Figures 3.19-3.21. A similar streamline was found in these figures compared to the figures which located at z = 0.29 c.

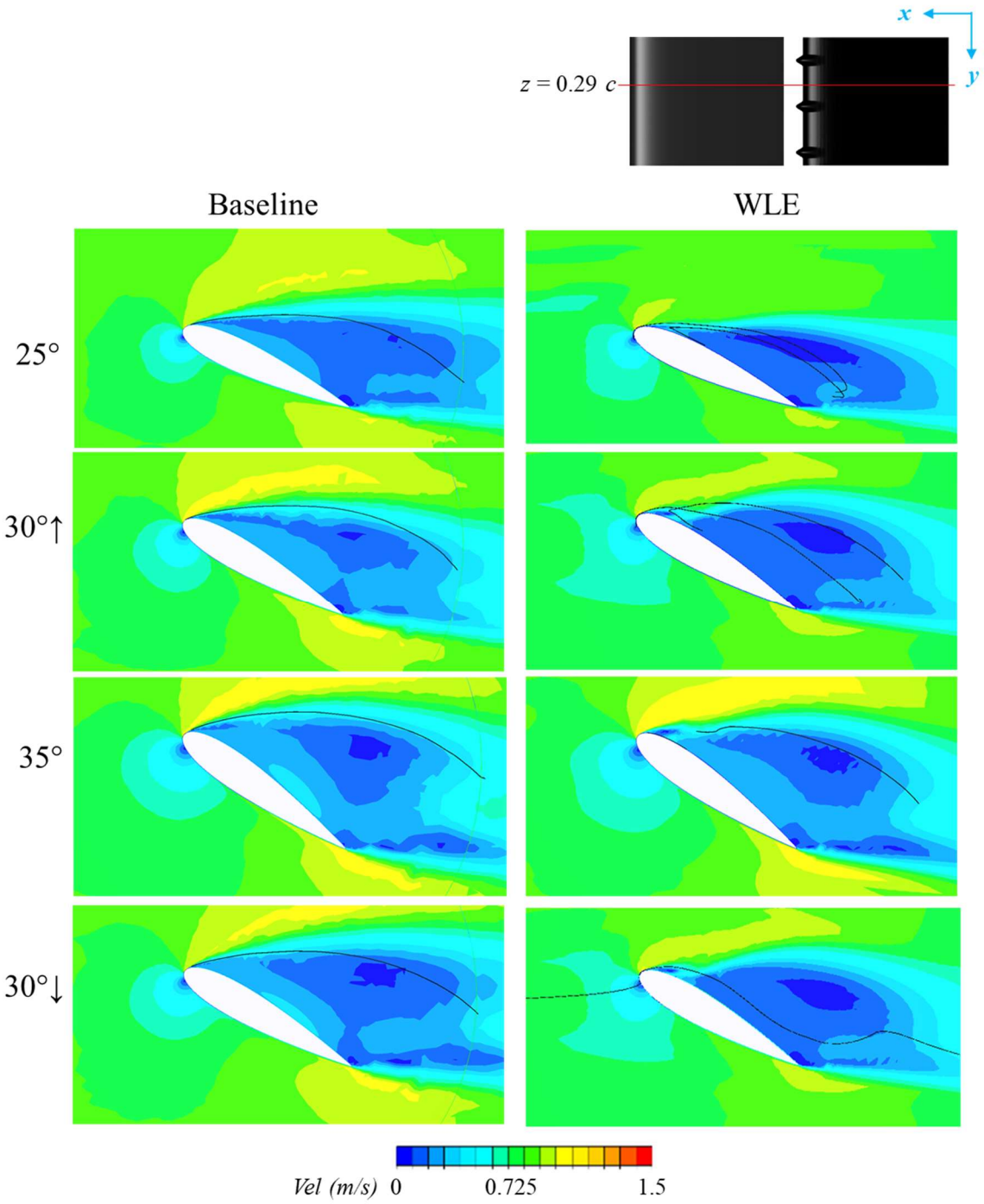

Figure 3.16 Comparison of velocity distribution at $z = 0.29c$, $k = 0.09$

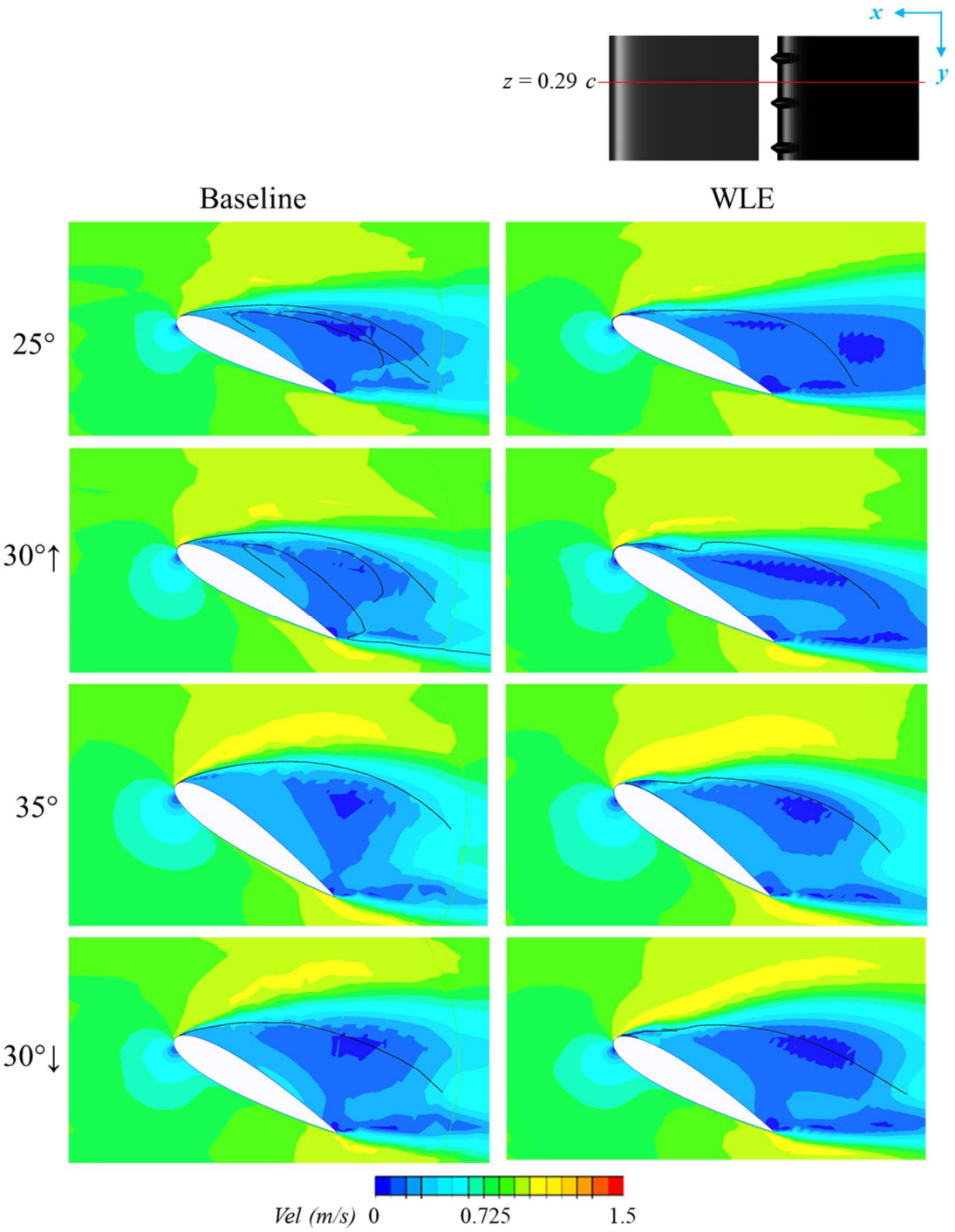

Figure 3.17 Comparison of velocity distribution at $z = 0.29c$, $k = 0.12$

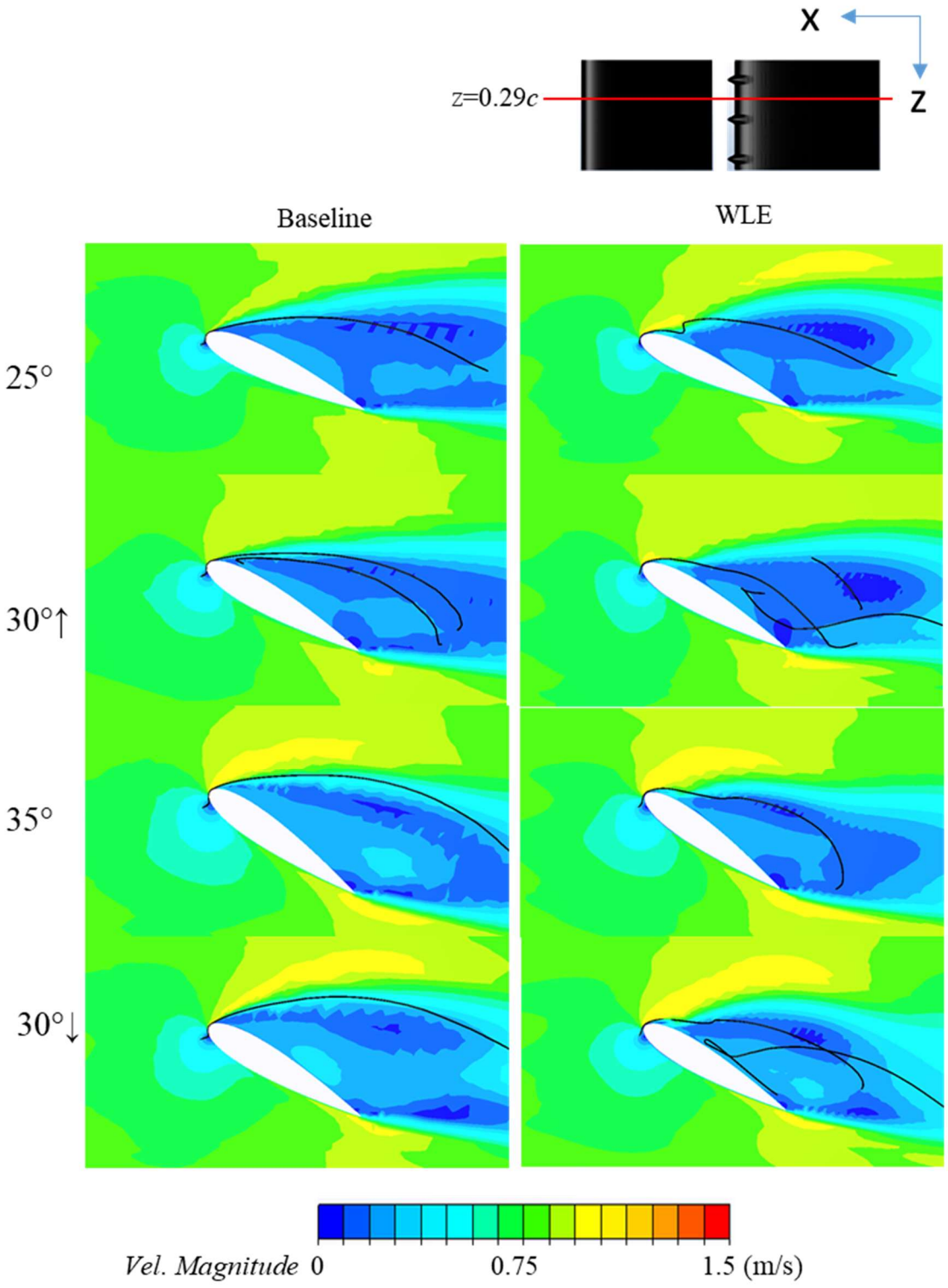

Figure 3.18 Comparison of velocity distribution at $z = 0.29c$, $k = 0.25$

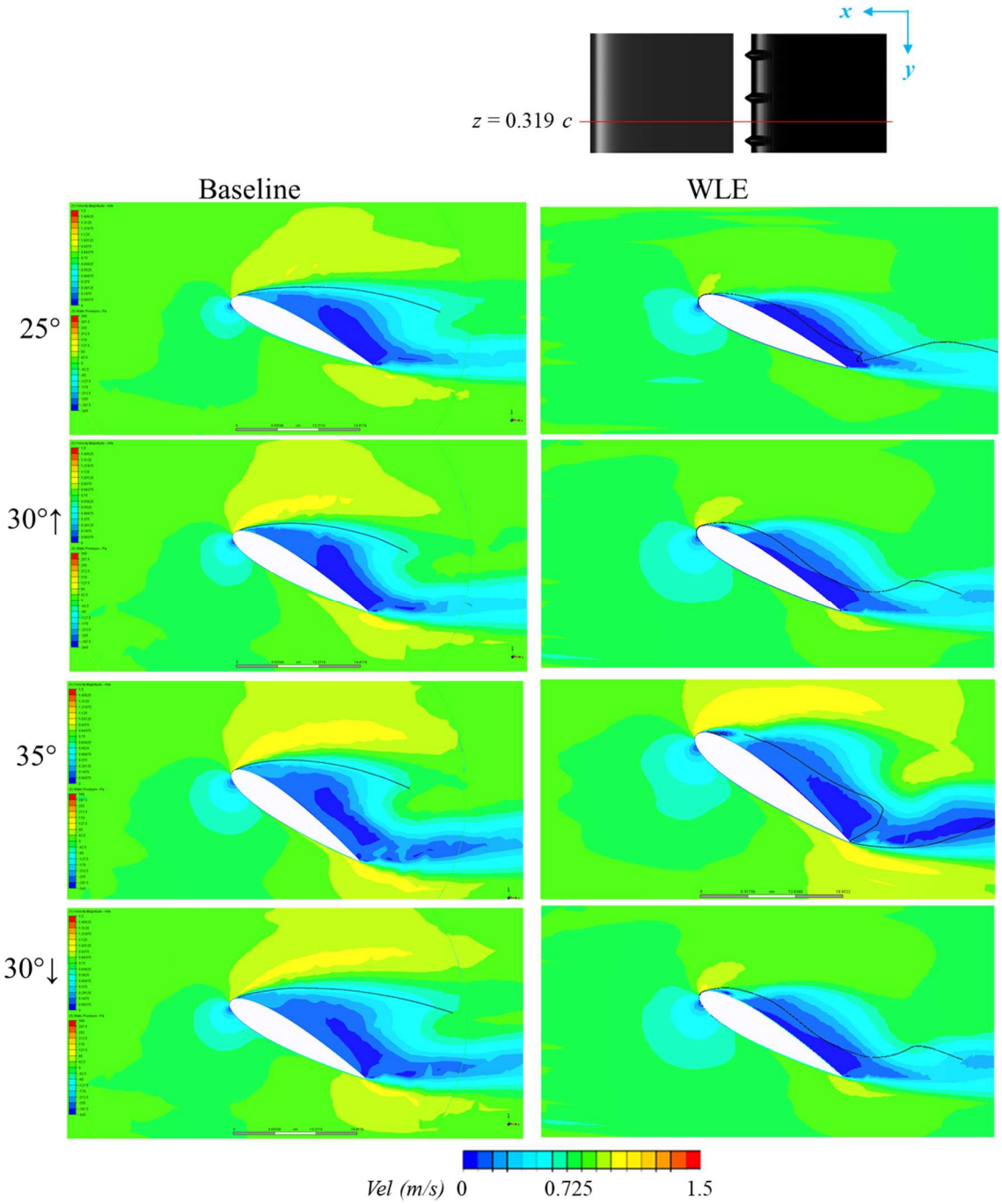

Figure 3.19 Comparison of velocity distribution at $z = 0.319c$, $k = 0.09$

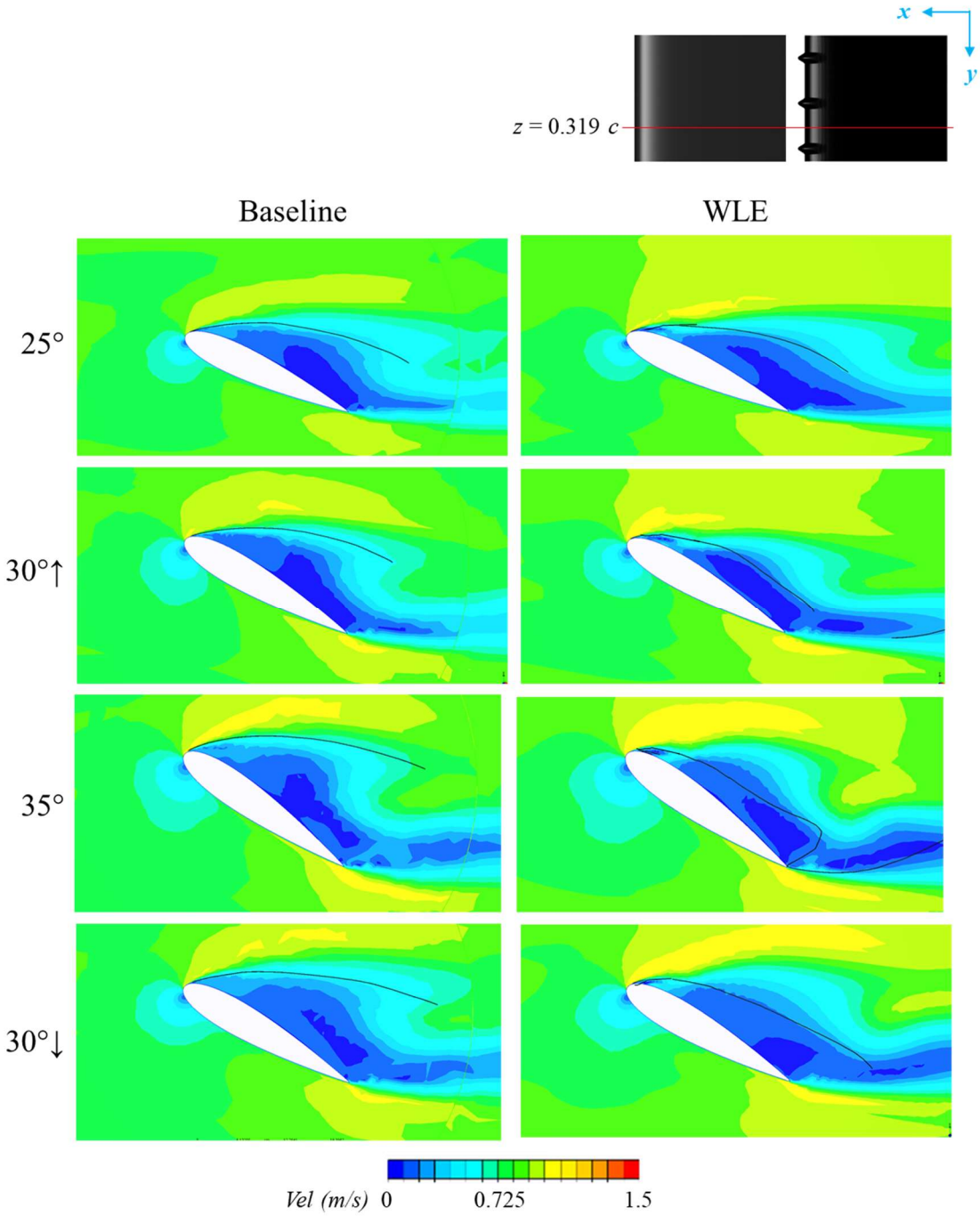

Figure 3.20 Comparison of velocity distribution at $z = 0.319c$, $k = 0.12$

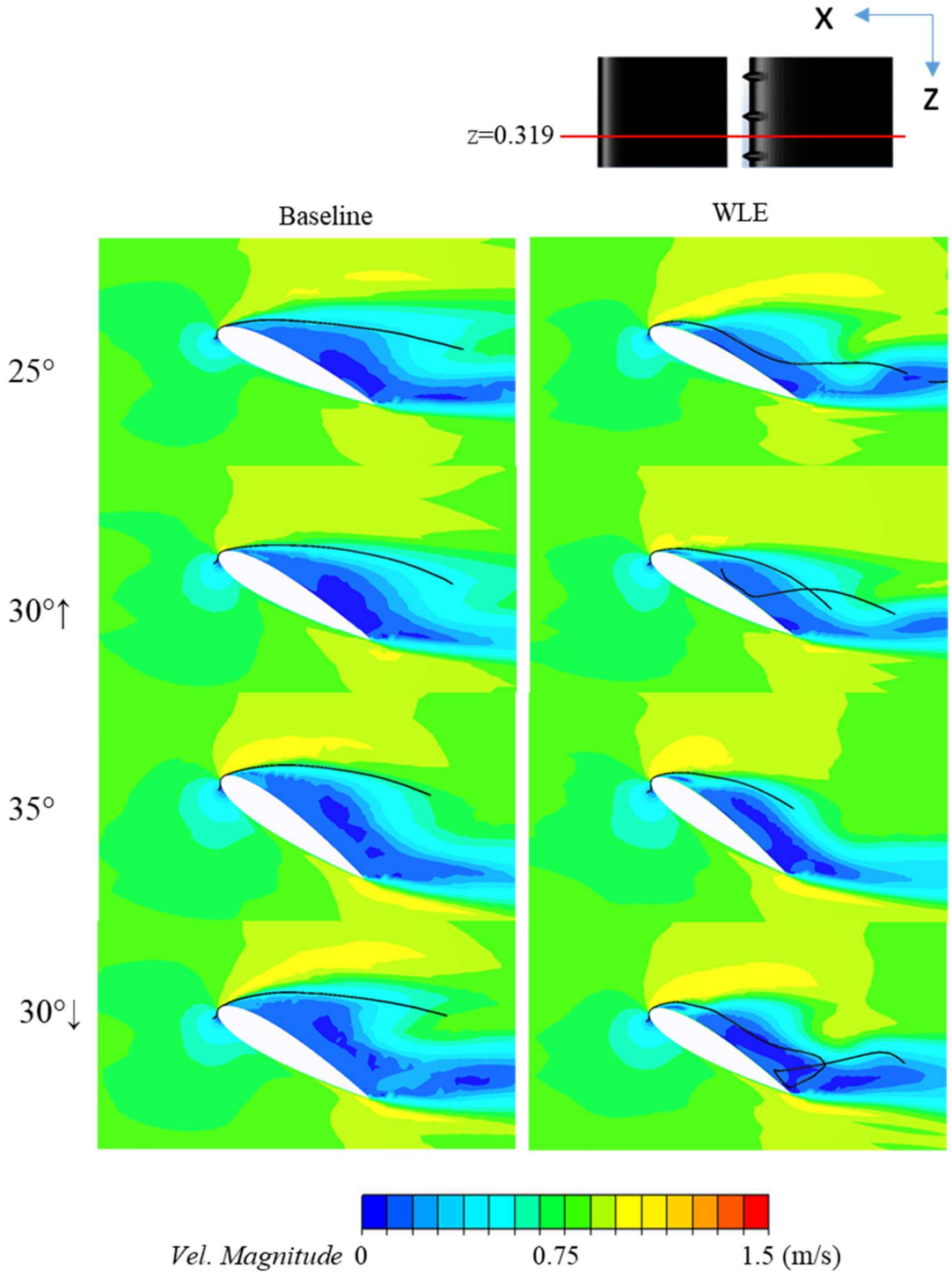

Figure 3.21 Comparison of velocity distribution at $z = 0.319c$, $k = 0.25$

Next, Figures 3.22-3.27 show the streamlines flowing through in front of the leading edge at the position $z = 3.632\ c$. The streamlines are rotating in the wing tip direction for WLE wing. While, in the case of baseline wing, the streamlines are headed straight to the trailing edge area. On WLE wing during upstroke motion, the streamlines are curlier than at the down-stroke motion. As described by Arai et al. [15], [48] and Torro et al. [25], the stream-wise vortical flow around WLE is thought to contribute to the suppression of separation. In the present unsteady study, the similar stream-wise vortical flow is observed around the WLE during the upstroke and down-stroke motion. The twisted vortical flow observed at the upstroke motion is stronger than the down-stroke motion, which is thought to be related to the fact that the higher lift is obtained at the upstroke motion than the down-stroke motion.

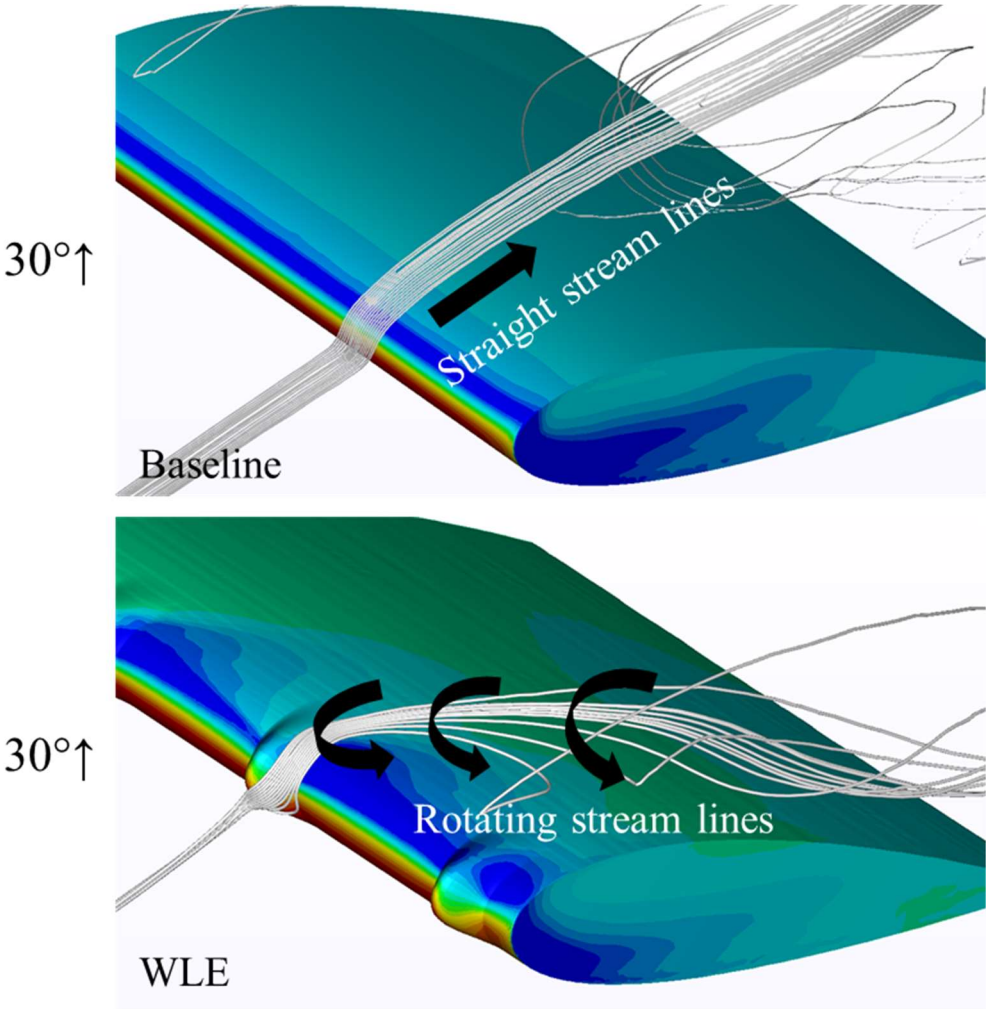

Figure 3.22 Up-stroke streamline at 30°, $k = 0.09$

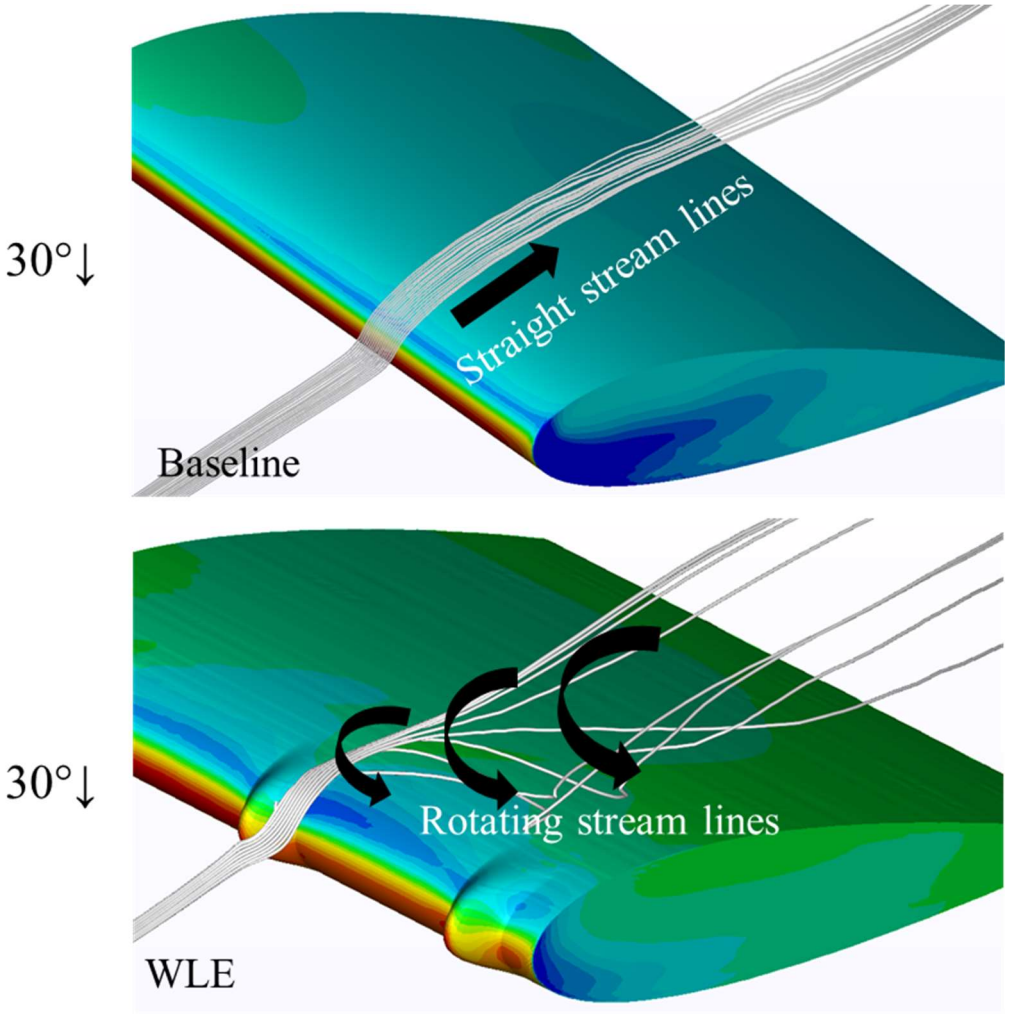

Figure 3.23 Down-stroke streamline at 30°, k = 0.09

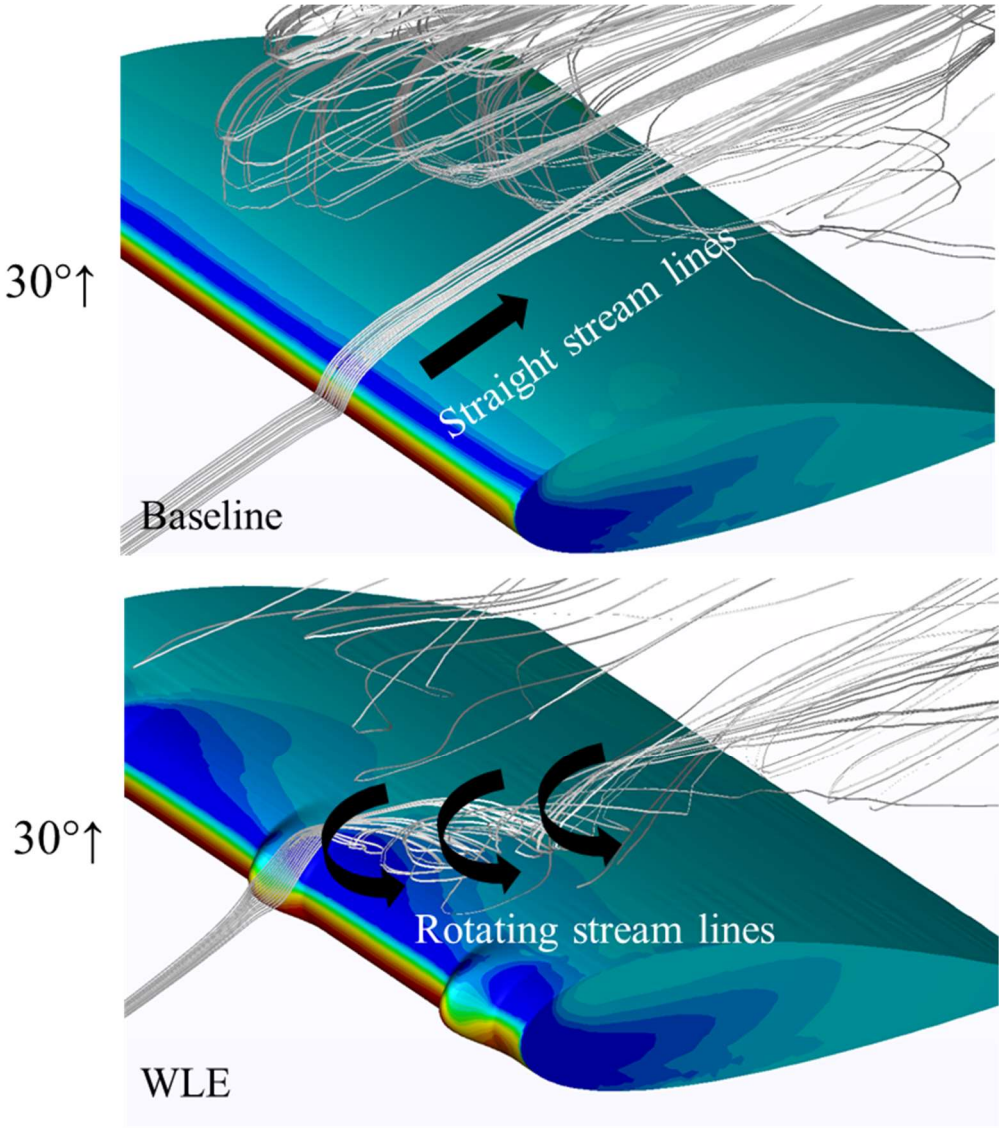

Figure 3.24 Up-stroke streamline at 30°, $k = 0.12$

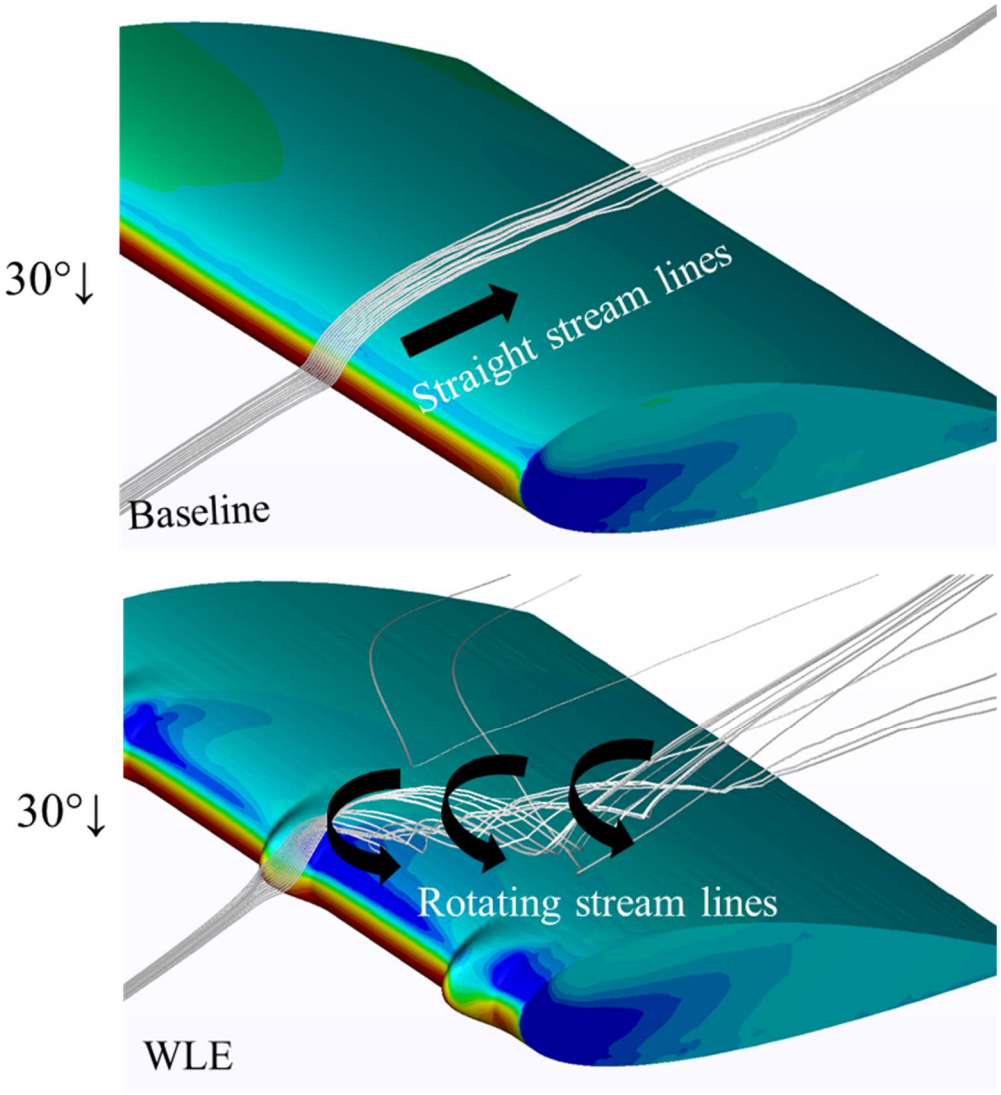

Figure 3.25 Down-stroke streamline at 30°, k = 0.12

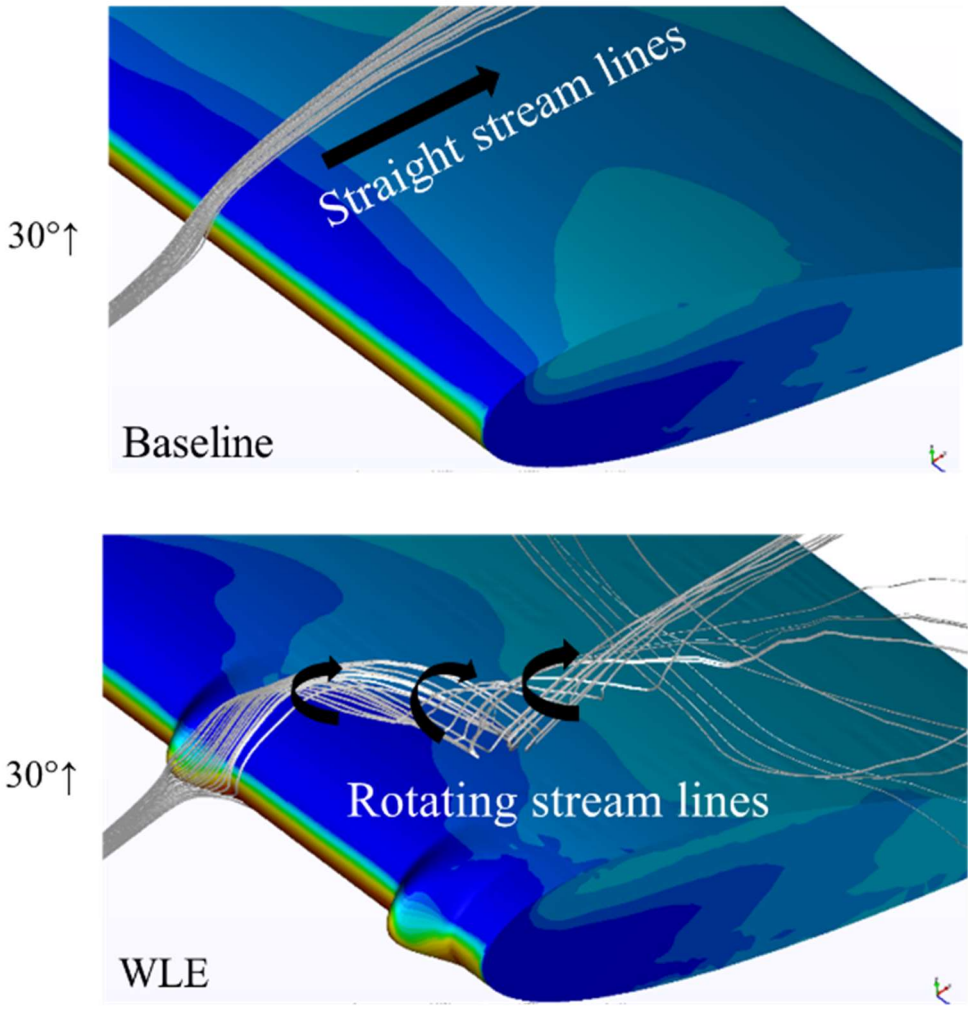

Figure 3.26 Up-stroke streamlines at α=30°, k = 0.25

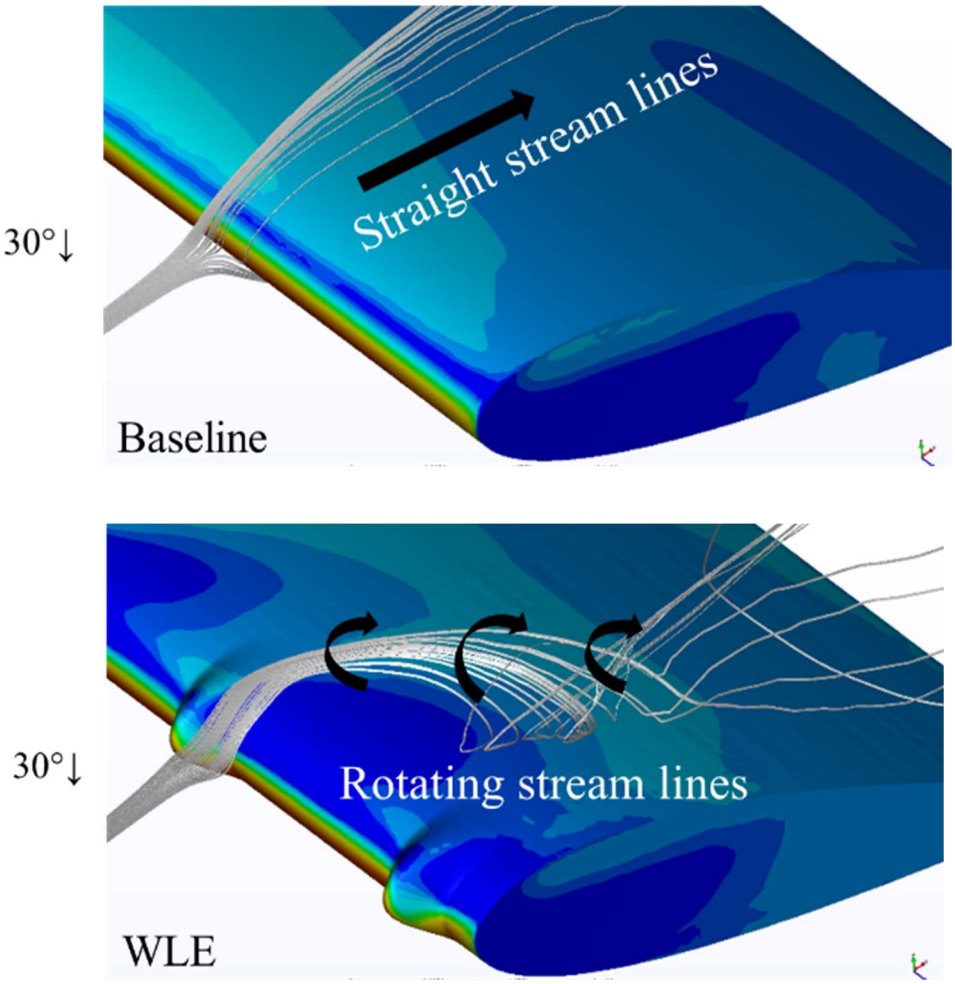

Figure 3.27 Down-stroke streamlines at α=30°, k = 0.25

3.4 Summary

In steady and unsteady cases the WLE effect on the rectangular wing was performed. Only one AR 1.6 was addressed in this chapter. To make a clear understanding of the WLE effect, the vortex generator (VG) was given as comparison. The VG wing has the same manner with the baseline wing, in a steady case. In the meantime, the WLE wing is able to acquire the lifting force after stall condition. The WLE wing has the best performance of three wing types. Therefore, just based on post-stall condition in unsteady condition. In this case, three reduced frequencies, i.e., k = 0.09, 0.12, and 0.25, were given to determine the WLE effect during unsteady condition. Clearly differences in the fastest reduced frequency k = 0.25 were observed between baseline and WLE wing.

Then, the streamlines distribution was explored around the WLE to find out the mechanism delaying the stall due to the WLE effect. The stream-wise vortical flow around the WLE is thought to contribute to the suppression of separation. In the present unsteady study, a similar stream-wise vortical flow has been observed around the WLE during the upstroke and down-stroke motion. The twisted vortical flow during upstroke motion is stronger than the down-stroke motion, which is thought to be related to the fact that the higher lift is obtained at the upstroke motion than the down-stroke motion.

CHAPTER 4
EFFECT OF WAVY LEADING EDGE WITH VARIOUS ASPECT RATIOS IN STEADY CASE

In this chapter, the WLE effect with various aspect ratio will be discussed to find out the WLE effect regarding the aspect ratio on the rectangle wing. There are four aspect ratios were conducted, i.e. 3.9, 5.1, 7.9 and 9.6 where the explanation of WLE effect emphasized only after stall condition. This various aspect ratio research is expected to use for some application such as fin stabilizer of ship, wind turbine or another fluid machinery.

Numerous applications such as fin stabilizers or wind turbines could be accomplished by learning from nature such as the wavy leading edge (WLE) in the flipper of the humpback whale. Their flipper morphology believed to increase the hydrodynamic performance by increasing the lift coefficient and reducing the drag coefficient. The pioneer research has been conducted by Fish et al [1] about the morphology of the humpback whale flipper. They reported that the tubercles of their flipper have an essential role to generate vortices to maintain lift and prevent a stall. The shape of their flipper is blunt and round in the leading-edge area. To obtain the benefit of this flipper shape, features of the WLE may be adapted to the applications which operate in a steady motion. Its applications could be worked with frequently facing the stall condition. Therefore, improvement should be necessary to avoid the stall condition within WLEs.

The previous chapter showed that the WLE wing with the aspect ratio 1.6 has superior forces at the post-stall region compared to the baseline wing in pitching motion. However, the previous studies above mentioned were conducted to explore the wavy leading-edge effect in just only steady case. In this study, to investigate the WLE effect based on variety of aspect ratios, steady case experiments were employed in this research. We investigate the effect of WLE regarding various aspect ratio. The numerical methods are carried out to clarify the flow mechanism on the wing with the WLE. Four aspect ratios are examined in the present study to find out advantages in practical applications such as fin stabilizers or wind turbines.

The shape of the WLE and the AR variations were referred AR 1.6 in the previous chapter. The plane view of the wings is shown in Figure 4.1. The chord length (c) of the wing is 125 mm.

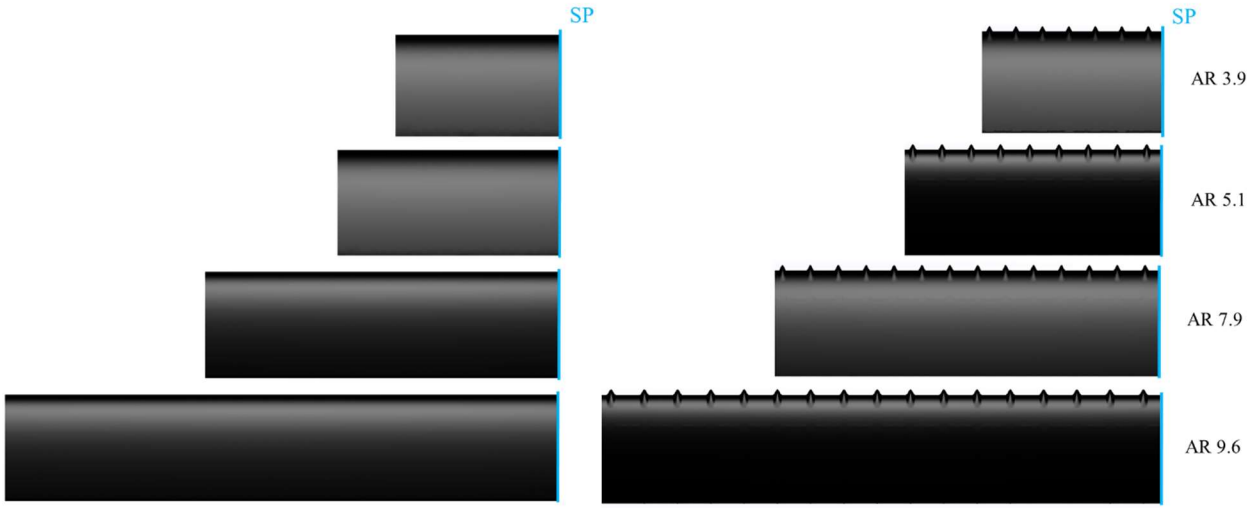

(a) Baseline wing (b) WLE wing

Figure 4.1 Plane view of the wings

In general, the wing performance could be expressed by using L/D ratio analysis. In this chapter, high performance wing adopted in the angles range from 0° to 35°. But before stall condition, the lift coefficient of WLE wing is a little bit lower than that of the baseline wing, although it is better after the dynamic stall condition. To find out the wing performance, the L/D ratio analysis was given to baseline wing and WLE wing as a comparison. In the Figures 4.2 and 4.3 show the L/D ratio for aspect ratio 3.9 and 5.1, respectively. During pre-stall condition, i.e. $\alpha < 17°$, the tendencies of L/D ratio on both wings were similar. In other hand, after stall condition, i.e. $\alpha > 17°$, the WLE wing has a favorable L/D ratio. It means that the WLE wing has the favorable benefit after stall condition.

4.1 Validation with Experimental Data

To validate the numerical analysis, the grid convergence of numerical results with experimental ones should be firstly required. The convergence check was performed in three different grid numbers with coarse, medium and fine mesh using the WLE wing of AR 1.6 at the angle of attack $\alpha = 25°$. The ratio of L/D was used to validate with the experimental results, and the convergence is indicated by deviation. The computed differences are shown in Table 1. Based on the deviation, the medium mesh has the lowest deviation. Therefore, the medium mesh system was employed in the following results of this study.

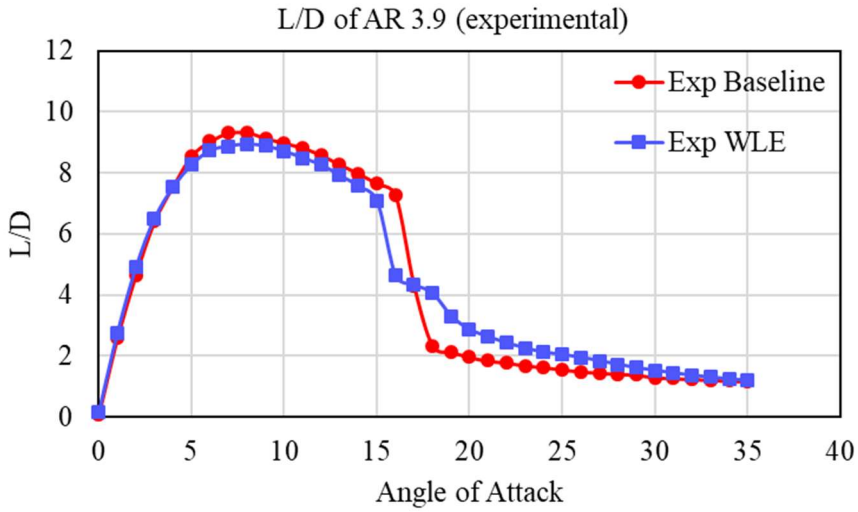

Figure 4.2 The ratio of L/D in AR 3.9 (experiment)

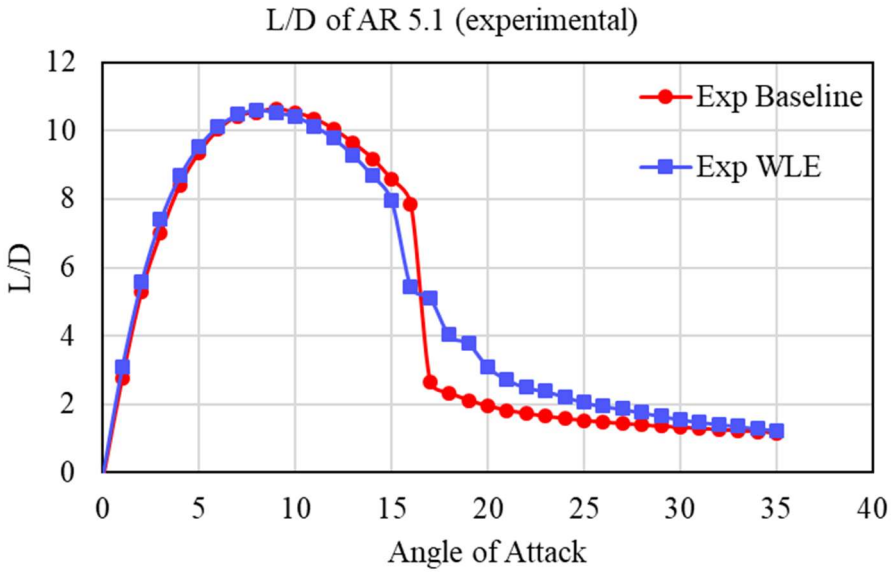

Figure 4.3 The ratio of L/D in AR 5.1 (experiment)

Figures 4.2-4.3 show the experimental and numerical results at the ratio of L/D in AR 3.9 and 5.1, respectively, in steady cases. The ratio of L/D in AR 7.9 and 9.6 are compared at the angle of attack 20° to 30° with no experimental results. The numerical results are in overall agreement with the experimental ones. Especially, the WLE wing show a pretty good agreement between them. On the other hand, there is a little difference with the experimental results for the baseline wing.

Table 1. Grid convergence

	Total Elements of Mesh	L/D	% deviation
Experimental	-	2.08	-
Coarse	3,160,847	2.00	3.91
Medium	11,407,996	2.01	3.43
Fine	20,838,293	1.81	12.85

4.2 Various Aspect Ratios

The similar tendencies of the ratio L/D can be found in Figures 4.4-4.8 for other aspect ratios. This may be caused by the wing in the deep-stall region. In this region, the small unsteadiness could be generated even-though the wing is set to a steady motion. The comparison of the maximum of L/D are shown in Figure 4.8. The tendencies of the wing results are pretty good with the experimental results. The tendency of numerical results on the baseline wing are a little higher than the experimental results. However, in this study, we are focusing on the improvement of hydrodynamic performance by using the WLE. We can see that the L/D of the WLE is higher than that of the baseline in all aspect ratios. Thus, the WLE could be one of the eco-friendly energy-saving-devices such as fin stabilizers of ships and wind turbines to improve hydrodynamic performance.

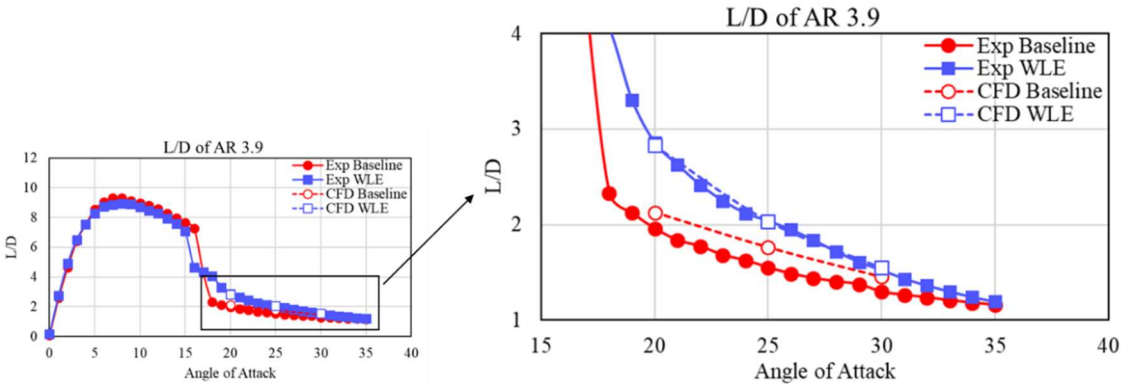

Figure 4.4 The ratio of L/D in AR 3.9

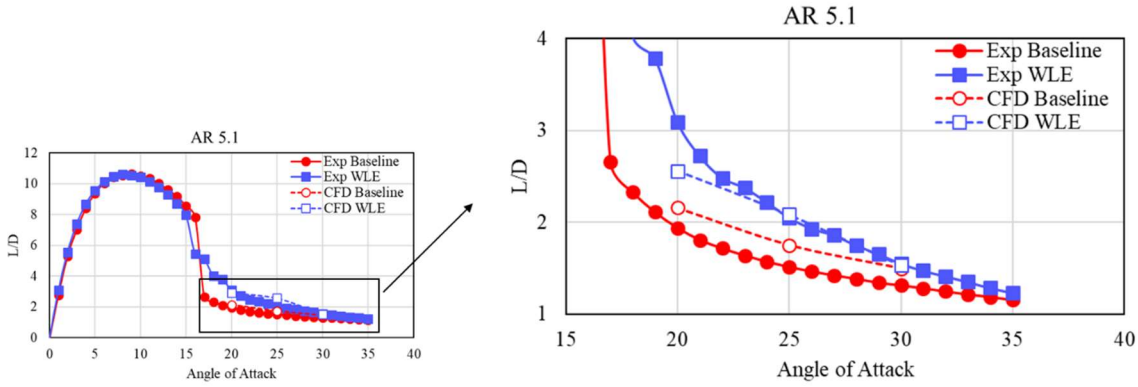

Figure 4.5 The ratio of L/D in AR 5.1

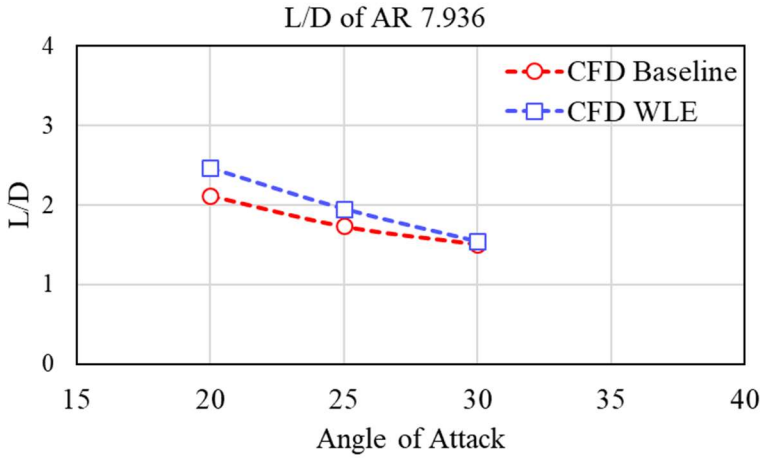

Figure 4.6 The ratio of L/D in AR 7.9

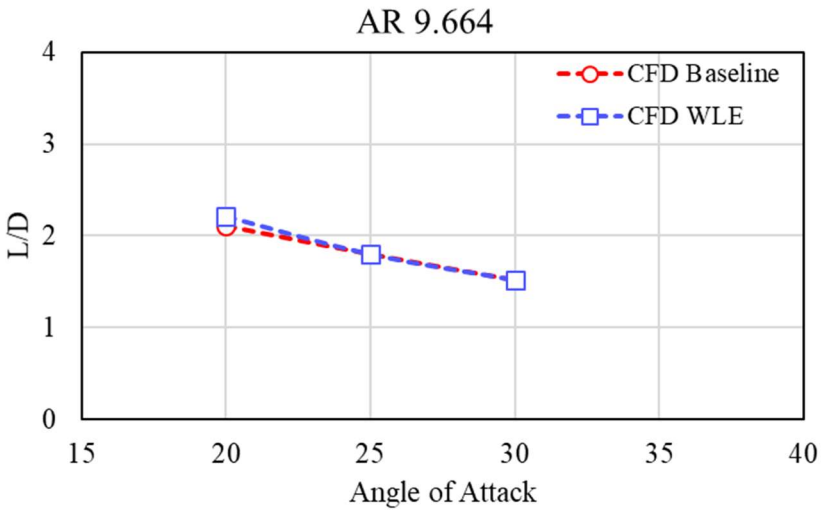

Figure 4.7 The ratio of L/D in AR 9.6

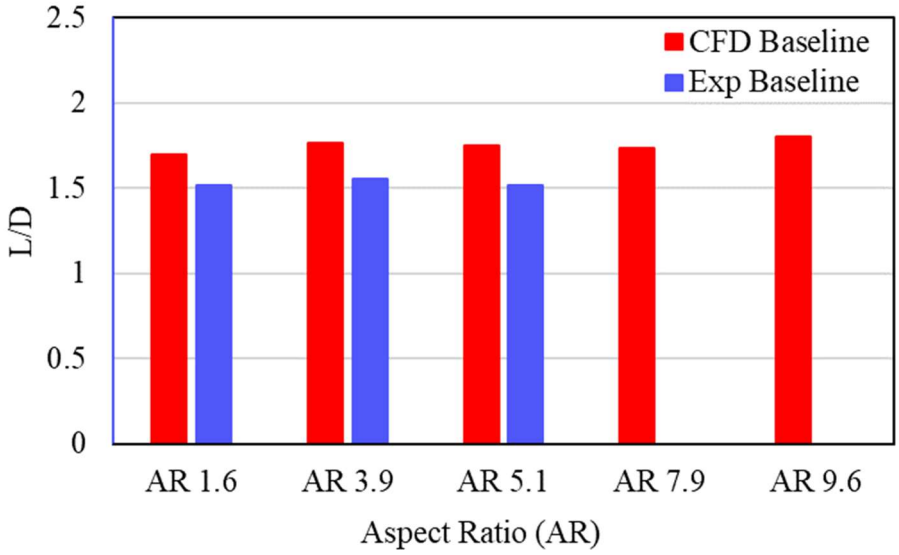

(a) Baseline wing

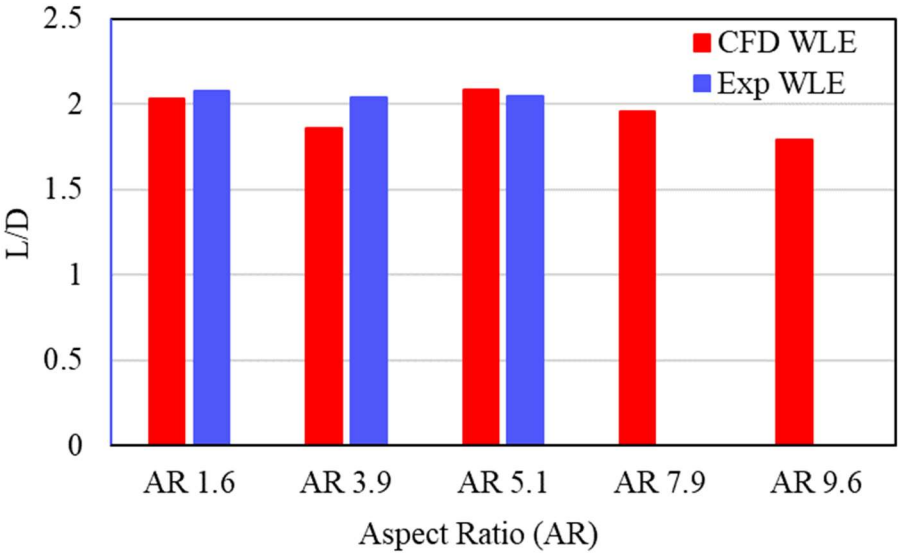

(b) WLE wing

Figure 4.8 The ratio of L/D in both wings at α = 25°

4.3 Effectiveness of WLE

In this section, the WLE effect was observed based on the WLE was placed on the wing. In the following figures were streamline in velocity magnitude distribution at AR 3.9 at the angle 25°. Figure 4.9 shows the velocity distribution at the mid-span in two *X*-*Y* plane (*a* and *b* plane). The streamline is spread to two areas i.e. the suction surface and the pressure surface of the wing. This formation created the *stream-tube* on the wing. Narrower *stream-tube* was found

in the WLE for both *a* and *b* position. Among two positions, the narrower *stream-tube* was found in *b* position. It indicates that the separation point in *b* position was delayed than in *a* position.

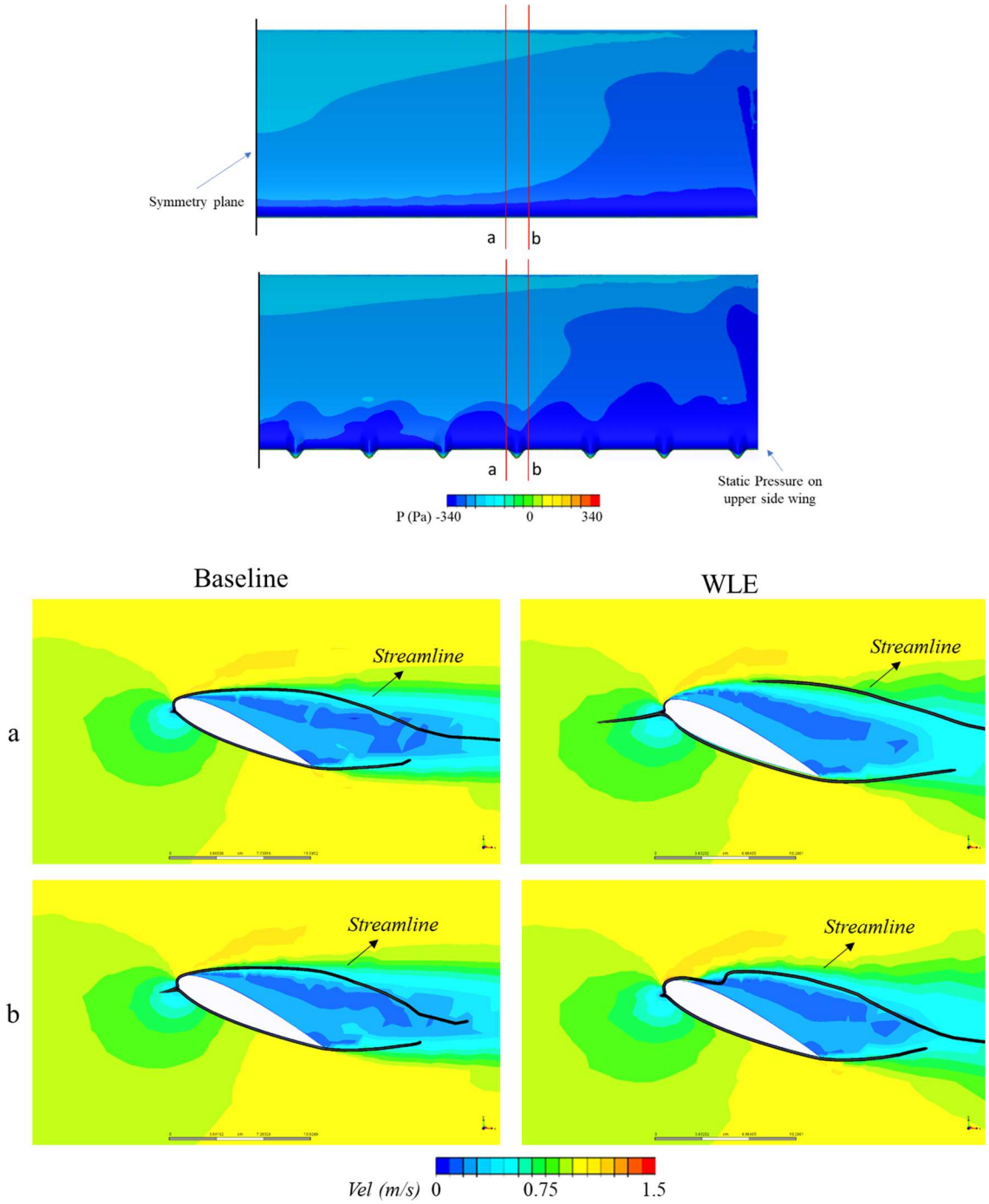

Figure 4.9 Velocity distribution of AR 3.9 at 25°

To make a clear comparison of wake area behind the trailing edge, Figure 4.10 shows the streamline around the wing in the static pressure distribution for AR 3.9 at the angle of attack

25°. As mentioned before, the streamlines in front of leading edge divided into two areas i.e. through the suction surface and pressure surface of the wing. Figure 4.10 describes the streamlines distribution in the symmetry plane, mid span and area close to the wing tip. Tighten wake area behind the trailing edge was found in the WLE wing along symmetry plane, mid span and area close to the wing tip.

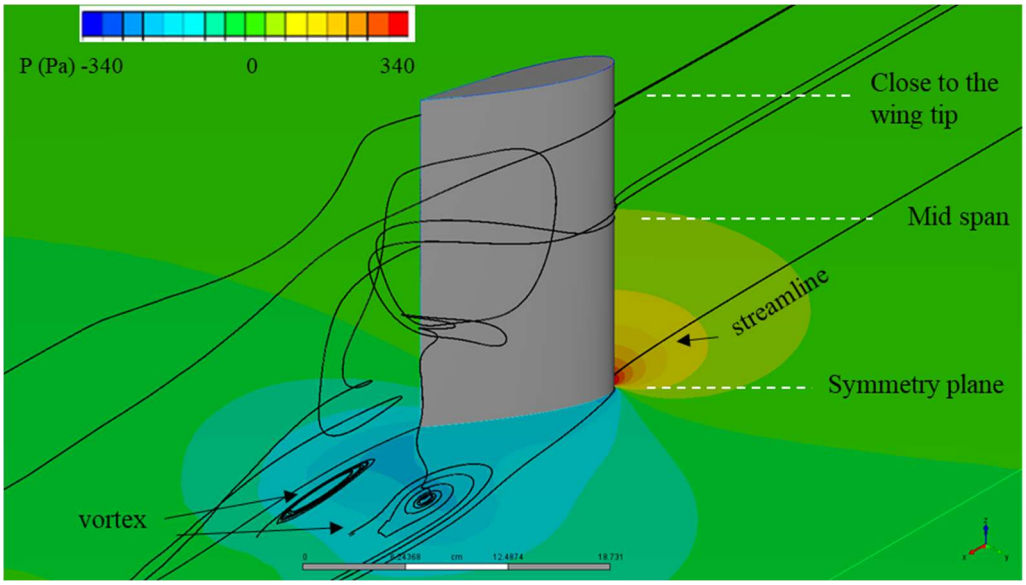

a) Baseline wing

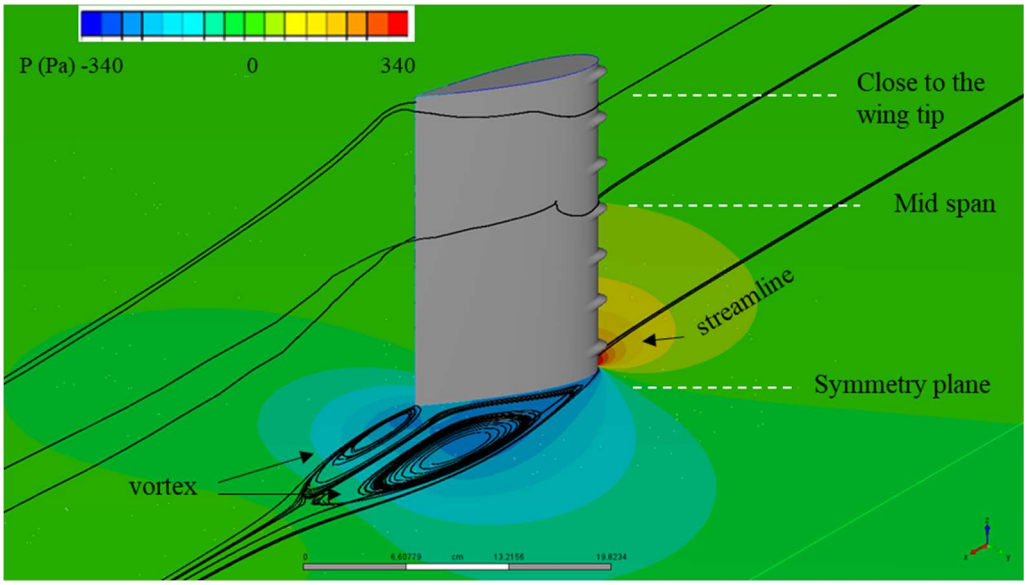

b) WLE wing

Figure 4.10 Streamline distribution of AR 3.9 at 25°

As comparison, the velocity distribution around mid-span at AR 5.1 and 7.9 given in the Figures 4.11-4.14 for AR 5.1 and 7.9, respectively. In the wing surfaces, we can see that the lower static pressure has wider area around the wing tip. Meanwhile, in the area between symmetry plane and mid-span, the lower pressure is not too large compared to the area between mid-span to the wing tip. In the velocity distribution figure for AR 5.1 and 7.9 has similar streamline tendency. The separation point around leading edge differences were found between baseline and WLE wing. In the WLE wing, the separation point was delayed that made the wake area was narrower comparing with the baseline. This phenomenon was clarified by streamline distribution in the Figures 4.12 and 4.14. Three area of streamline distribution were described in these figures. i.e. in the symmetry plane, mid span, and area close to the wing tip. In the symmetry plane, the wake area created by two streamlines was wider than the mid span and area close to the wing tip. It seems that the WLE has no effect in this location. But in the mid span section or area close to the wing tip, the wake area behind the trailing edge become narrower. Prove that the effectiveness of WLE was found based on its location i.e. between mid-span to the wing tip area only. This fact will be used for modified wing in chapter 6.

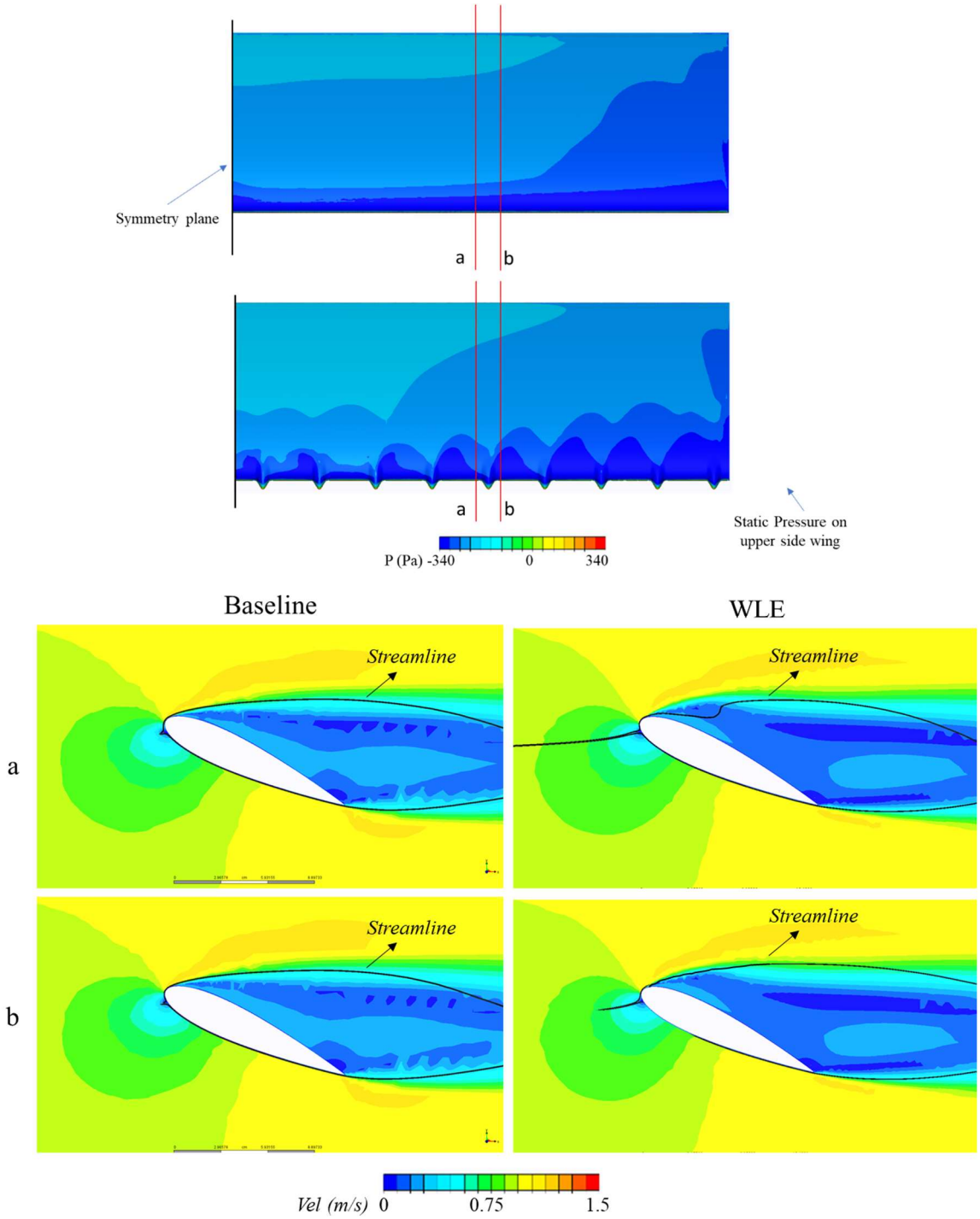

Figure 4.11 Velocity distribution of AR 5.1 at 25°

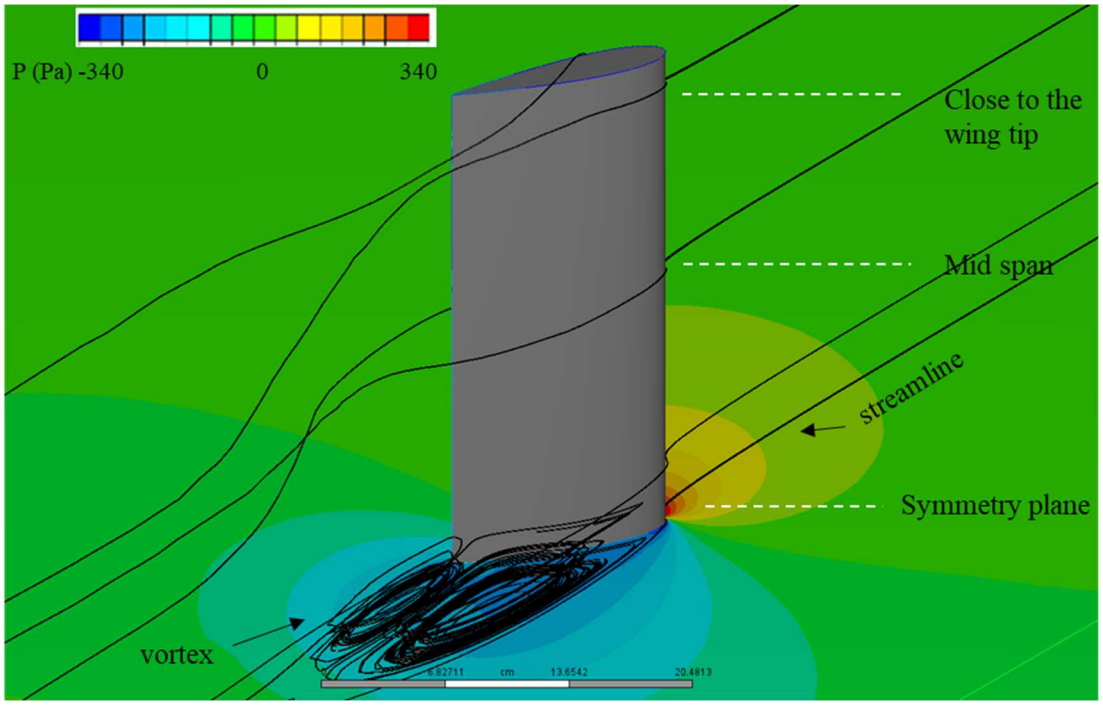

a) Baseline wing

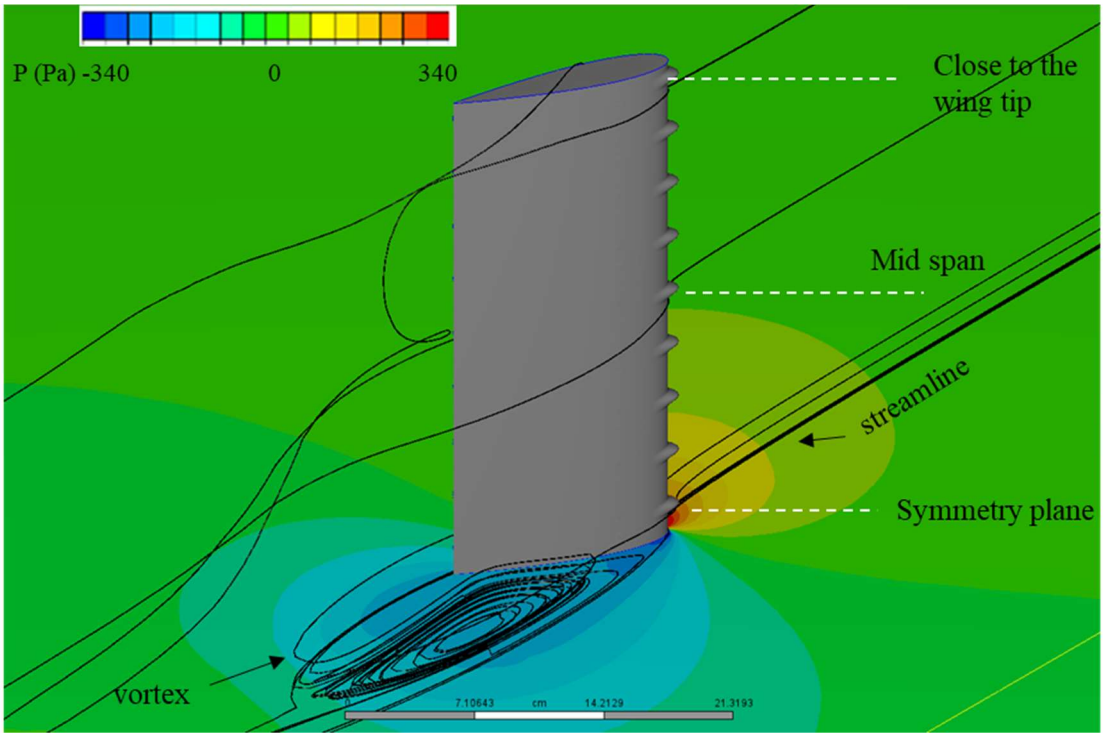

b) WLE wing

Figure 4.12 Streamline distribution of AR 5.1 at 25°

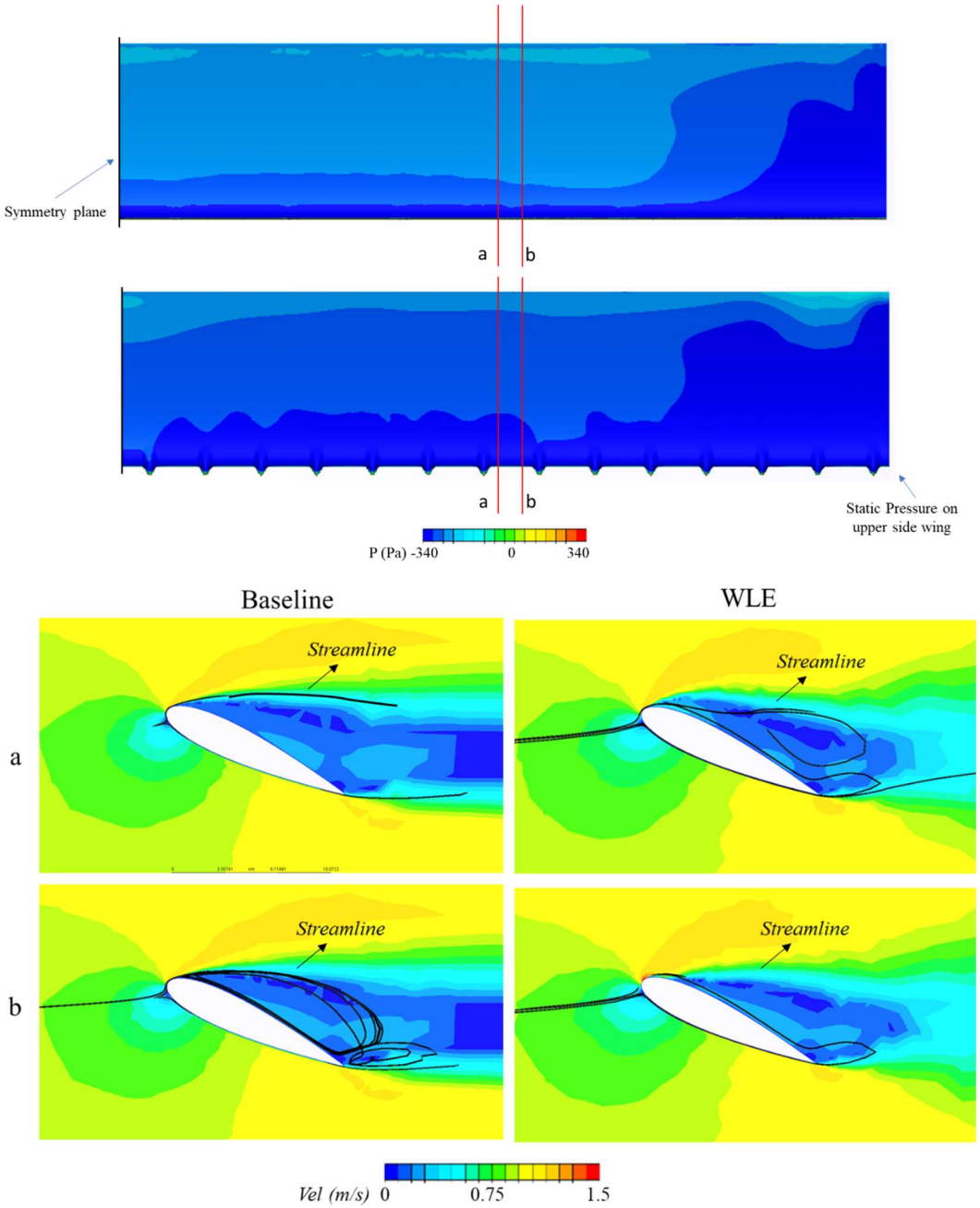

Figure 4.13 Velocity distribution of AR 7.9 at 25°

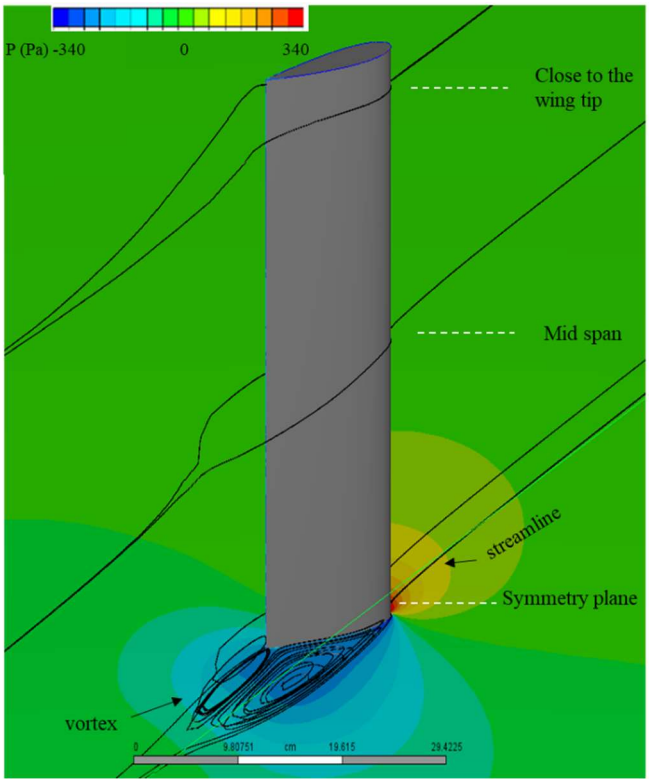

a) Baseline wing

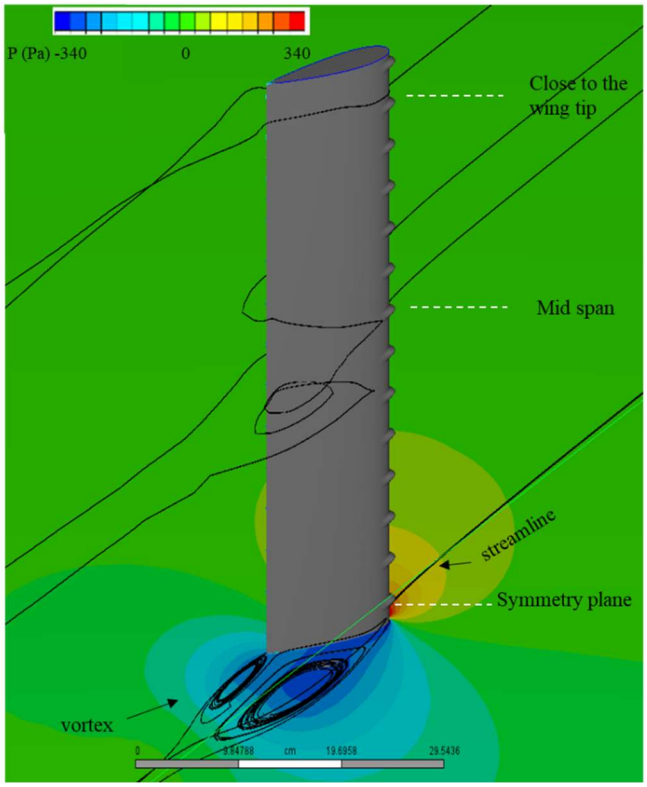

b) WLE wing

Figure 4.14 Streamline distribution of AR 7.9 at 25°

4.4 Aspect Ratio Effect

Next, the distribution of pressure coefficient (*Cp*) is investigated to clarify the WLEs effect on various aspect ratios. The attack angle of $\alpha = 25°$ is compared to examine the pressure distribution in the stall angle on various aspect ratios. Figure 4.15 shows the surface distribution of *Cp* at the all aspect ratios in both wings. The symmetry plane in those figures is denoted as "SP". The lower pressure region is indicated as blue area in Figure 4.15. We can find significant differences in the *Cp* distribution in both wings. The lower pressure is dominant around the WLEs area, and then this lower pressure area indicates that the fluid flow goes smoothly through around the WLE compared with that of the baseline wing at the all aspect ratios. Therefore, the WLEs could control fluid flow and hydrodynamic stall around the leading edge of the upper surface of the wing, and then the lift force could be increased at the larger attack angle, especially after the dynamic stall. The separation flow could be also controlled by the WLE. The WLE could improve the hydrodynamic performance of the wing. In the wing tip area, the wider low-pressure area can be found in the WLE wing at the all aspect ratios. Nevertheless, the WLE located near the SP, has no significant effect on the whole flow field and pressure distribution.

In the Figure 4.15, we can see that an interesting phenomenon between AR 7.9 and 9.6 in both wings baseline and WLE wing in pressure distribution. In the baseline wing comparison, AR 9.6 has wider area of low pressure than AR 7.6. It indicates with the deep blue region is wider at AR 9.6 than 7.9 in the wing tip area. In the baseline wing comparison, AR 9.6 has the best pressure distribution. Opposite phenomenon was found in the WLE wing comparison. On the WLE wing at AR 7.9 wing has wider area around the wing tip. In this research, we are focused on an improvement of hydrodynamic performance using WLE. Therefore, it is no problem if baseline wing at AR 9.6 has the best performance. We are focused on find out WLE effect regarding the AR on the wing. So, we can conclude that AR 7.9 on the WLE wing has the best performance in this case. To ensure the comparison of AR, the next section will be discussed the *Cl* and *Cd* comparison of each AR.

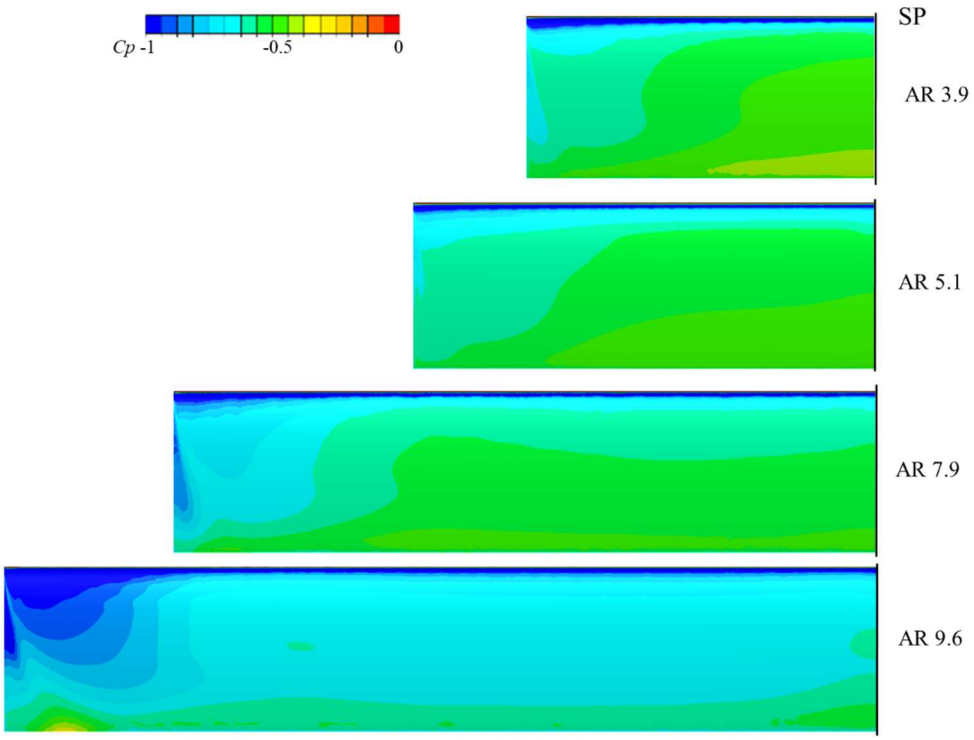

(a) Baseline wing

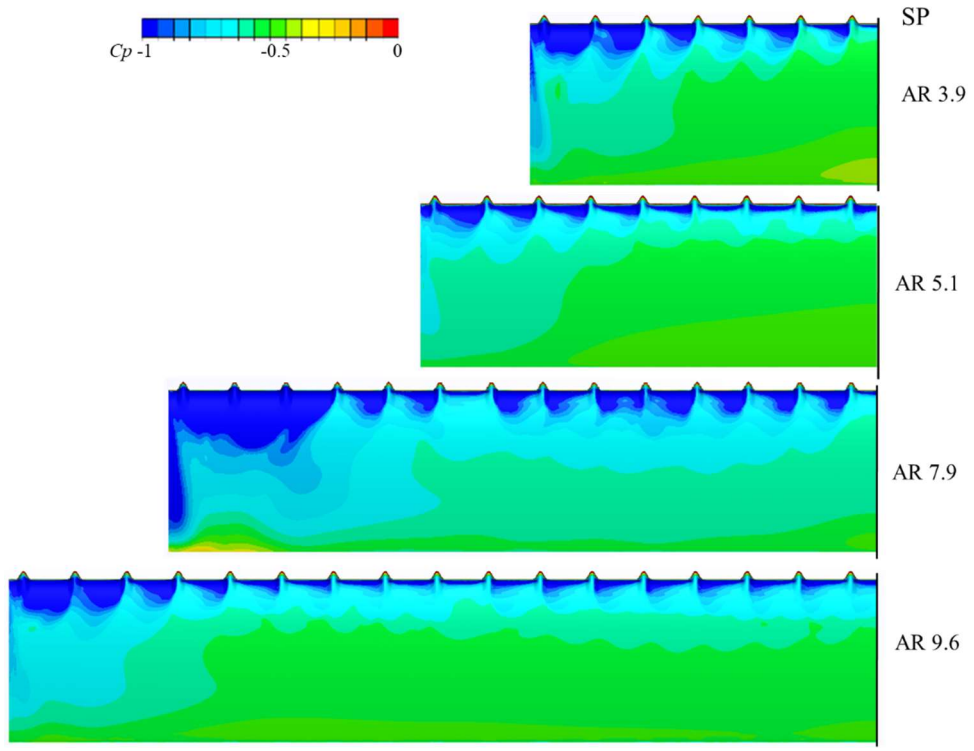

(b) WLE wing

Figure 4.15 Pressure distribution, *Cp* on the upper surface of the wings

Next, further analysis is focused on the WLEs located around the wing tip. The middle section between the second and the third WLEs from the wing tip is focused to investigate the WLE effect on various aspect ratios. We can see that on the right side, i.e. separation point of the wing is delayed than that of the baseline wing. As mentioned in previous chapter, the streamlines are directed toward to the trailing edge of the baseline wing, while the streamlines are rotating to the wing tip direction for the WLE wing. These streamlines are affected by the flow separation on the wing. As described in the references [25] the vortical flow streamlines around the WLE could contribute flow separation control.

In the following Figures 4.16-4.18 are a comparison of experimental and CFD method each AR at angles 20°, 25° and 30°. As reference, AR 1.6 was added in this section. The CFD's tendencies were similar to the experimental results. To find out the effective AR, a comparison of *Cl* and *Cd* at each AR is necessary. These figures show the *Cl* and *Cd* at the angles 20°, 25° and 30°, respectively. In these figures, the infinity wing was conducted to make clearly explanation of optimization AR. Highest lift coefficient was found in aspect ratio 7.9 at three angles i.e. 20°, 25° and 30° on the WLE wing. From *Cl* and *Cd* aspect ratio analysis, 7.9 aspect ratio has the best performance. Therefore, to approach the *Humpback whale* flipper shape, the wing is modified to taper wing. This modified wing will be discussed in the next chapter.

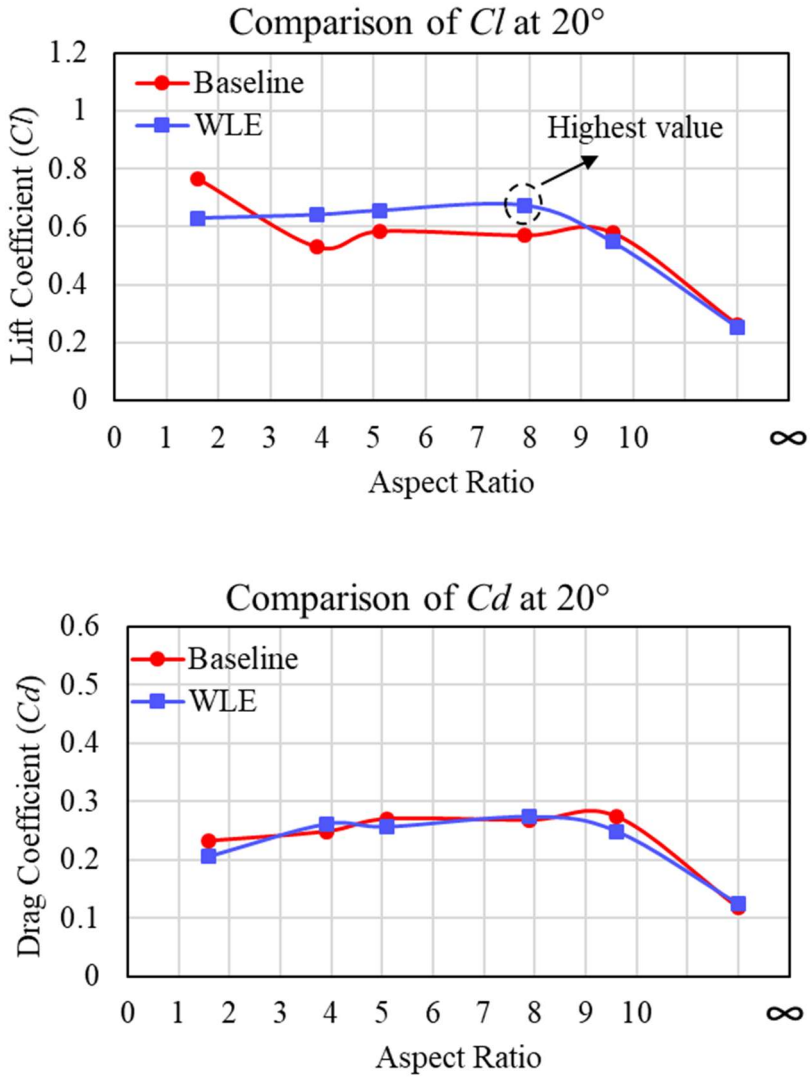

Figure 4.16 Comparison of *Cl* and *Cd* at the angle 20°

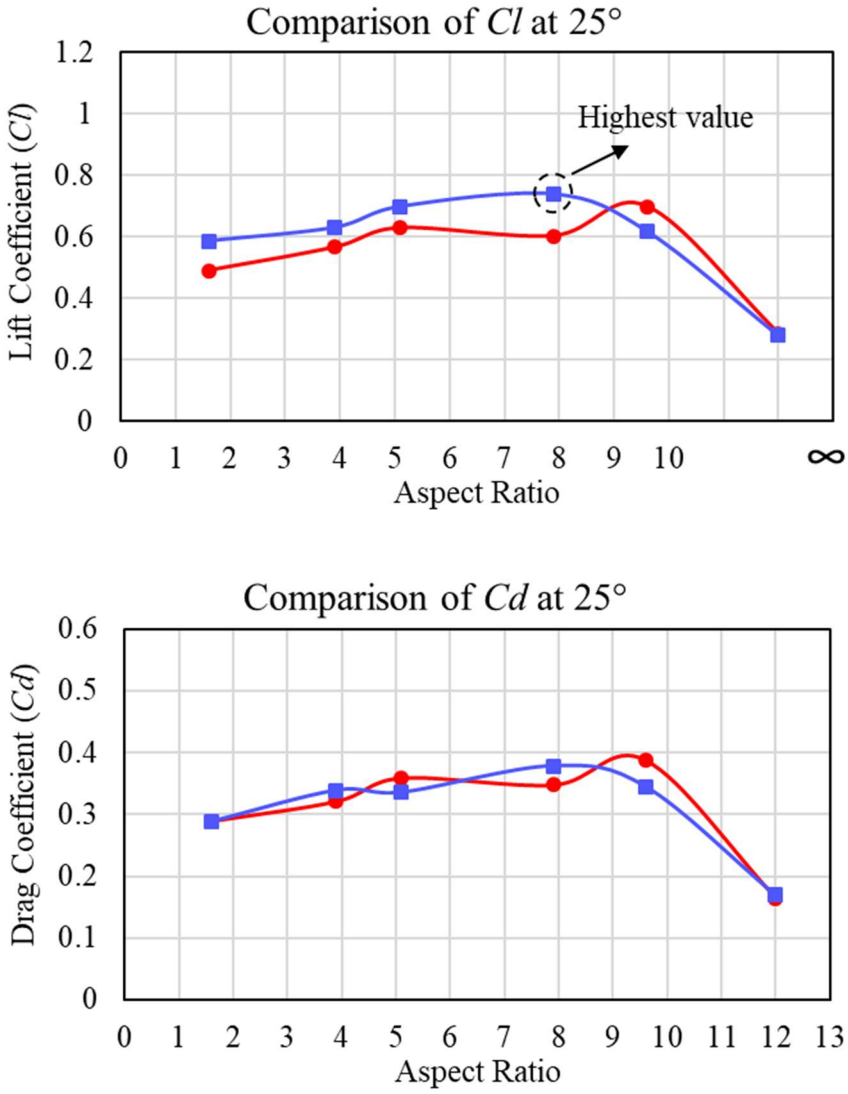

Figure 4.17 Comparison of *Cl* and *Cd* at the angle 25°

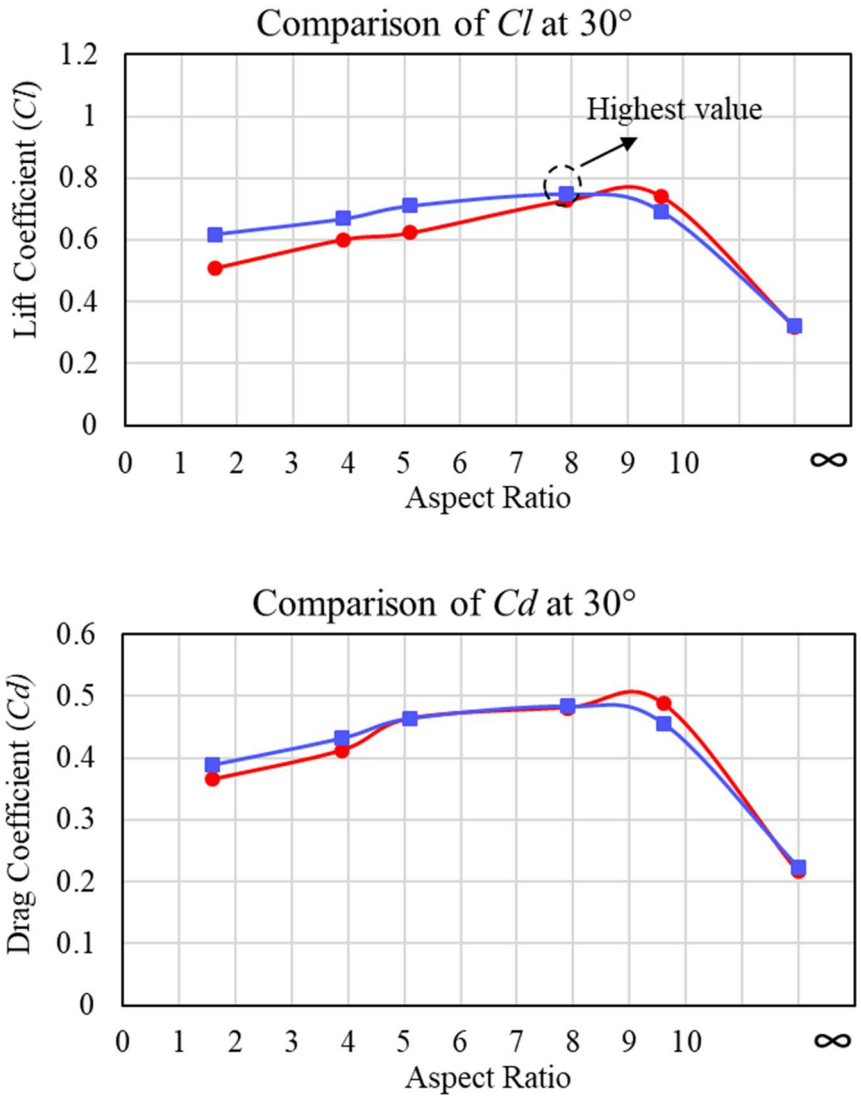

Figure 4.18 Comparison of *Cl* and *Cd* at the angle 30°

4.5 Summary

To get maximum applications on the WLE effect, the various aspect ratios has been performed in this study in the rectangular wing and steady case only. There are 1.6, 3.9, 5.1, 7.9, and 9.6 of aspect ratios. The best aspect ratio in this study is 7.9, which has the best lift coefficient in each angle compared to all aspect ratio. The WLE effect location also observed in this chapter. There are three sections to verify the WLE effect i.e. on the symmetry plane, mid-span, and area close to the wing tip. The WLE in the mid-span to the area close to the wing tip has the strongest effect to suppress the separation.

CHAPTER 5
UNSTEADY ANALYSIS OF WAVY LEADING-EDGE EFFECT ON THE RECTANGULAR WING WITH ASPECT RATIO SERIES

The most important of the aim of this research was implementation of WLE on some fluid machineries such as fin stabilizer or wind turbines. These applications suffer the dynamic stall due to its in unsteady motion. Therefore, unsteady analysis with various aspect ratios is necessary to explore. In the chapter 3, the unsteady case analysis was carried out only at aspect ratio (AR) 1.6. The WLE wing has superior value of *Cl* than the baseline wing, especially in the upstroke motion. In this chapter, unsteady analysis of 3.9, 5.1 and 7.9 aspect ratio will be employed. As mentioned before in the chapter 2, AR 3.9, 5.1 and 7.9 using rectangular wing of NACA 0018 profile with the chord length (*c*) 125 mm. The shape of WLE has wavelength (*W*) equals 8% of *c* and amplitude (*d*) 5% of *c*.

5.1 Unsteady analysis of rectangular wings

The unsteady analysis was performed after stall condition, i.e. at the angles 25°-35° only. Figure 5.1 shows the *Cl* and *Cd* at AR 3.9 in steady and unsteady cases. As a comparison, the steady case of experimental result was shown in this section. The baseline wing at the upstroke motion was completely similar to the experimental results at the angles 28°-35°. But at the downstroke motion, the *Cl* were lower. A similar result was found on the WLE wing, the *Cl* value in the upstroke motion has similar value with the steady case at the angles 30°-35°. Meanwhile, in the *Cd* comparison, the baseline wing has a lower value than the steady case. For the WLE wing, the *Cd* results were quite good with the steady case result. Since the unsteady result during the upstroke motion at the angle 30° has been similar with steady one, then the pressure coefficient and velocity distribution in this angle was explored as comparison as shown in the Figures 5.2-5.3, respectively.

Figure 5.2 shows the pressure coefficient at the angle 30° at AR 3.9. This figure shows that the WLE wing has the low pressure comparing the baseline in the steady and unsteady cases. Significant differences were found in the WLE wing during upstroke motion. The low pressure is dominant along its surface. It indicates that the flow was easier through the wing surface. Then the separation is possible to be postponed. In the Figure 5.3 shows the velocity magnitude distribution in the mid span. At the first glance the differences are the separation

point which is located near the leading edge. On the WLE wing, the separation point is slightly delayed compared to the baseline wing. Beside that the wake area formed is narrower on the WLE wing. Next in the Figures 5.4-5.6 show discussion the performance of AR 5.1 wing.

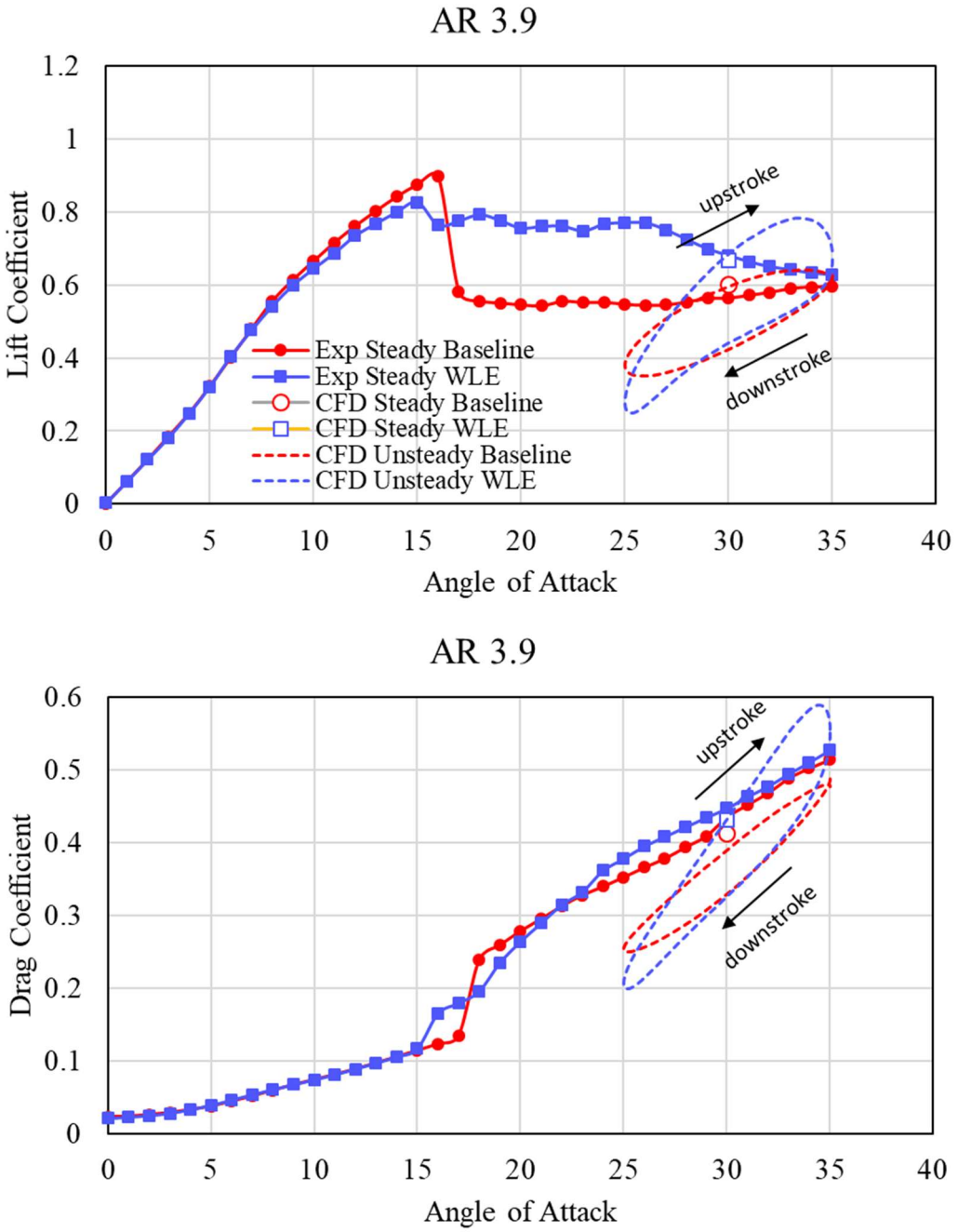

Figure 5.1 The *Cl* and *Cd* at AR 3.9 in steady and unsteady case

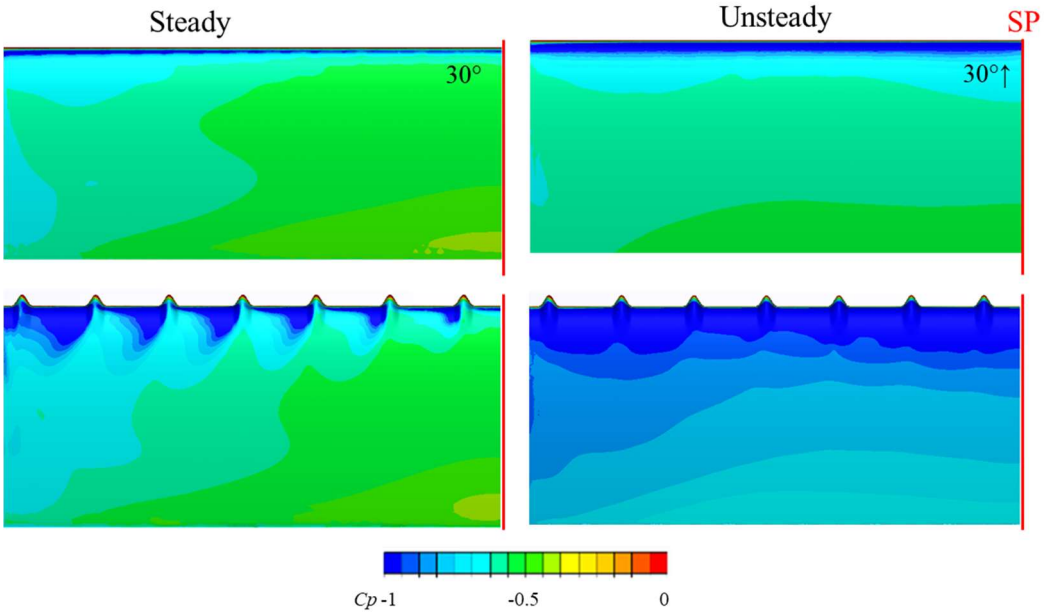

Figure 5.2 Pressure coefficient distribution of AR 3.9 in steady and unsteady case at 30°

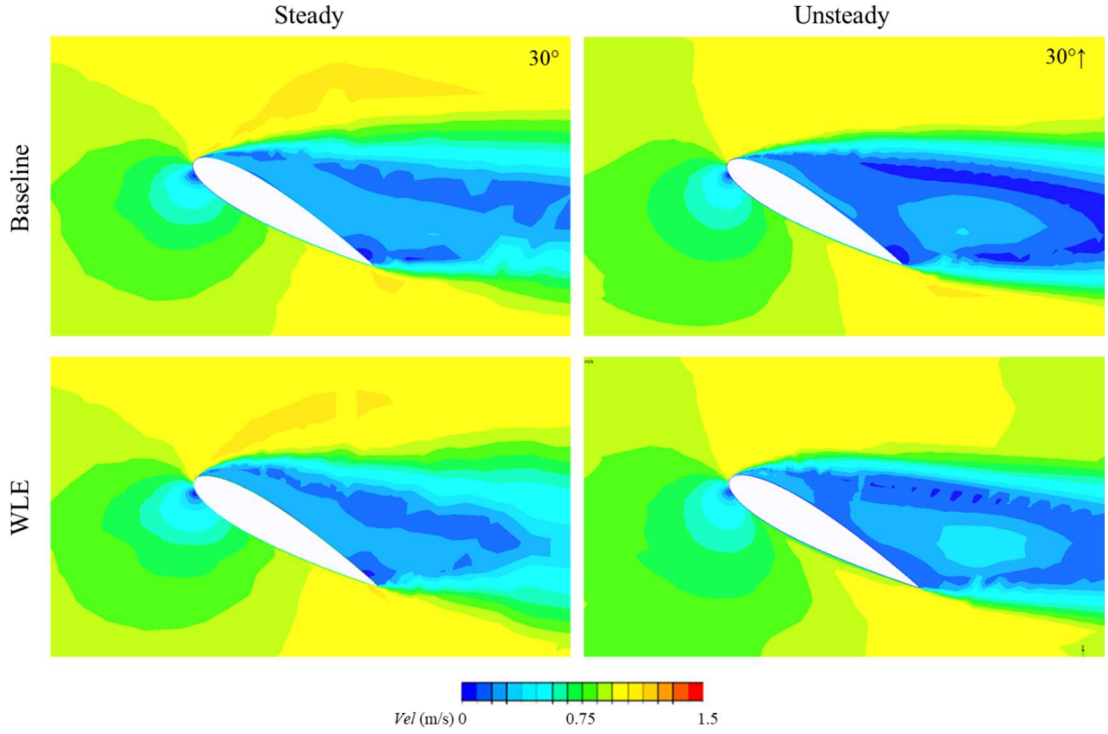

Figure 5.3 Velocity Magnitude distribution of AR 3.9 in steady and unsteady case at 30°

In the Figure 5.4, similar results were found in the AR 5.1 wing, where after stall condition in the range angle 25°-35° the WLE wing has higher *Cl* compared to the baseline

wing during upstroke motion. The *Cl* in the baseline wing during upstroke motion were same in the angles 30°-35°. During downstroke motion, the WLE and baseline wing has similar tendency. An interesting fact is in the angle of attack 30°, the steady and unsteady case meet in the same *Cl* value. So, a comparison was employed in this angle as shown in the Figures 5.5-5.6.

Pressure coefficient (*Cp*) on the suction wing surface were shown in the Figure 5.5. In the left side were the pressure coefficient distribution in steady case, then in the right side were unsteady case result during upstroke motion. There are no significant differences between steady and unsteady case in the baseline wing. But we can see the significant differences in the WLE wing between steady and unsteady case result. The deep blue colour almost covered up along its surface. This colour distribution indicates the lower pressure on the surface. So, we can say that in the WLE wing during upstroke motion the flow was easier through the wing surface. The unique fact is unsteady motion has better performance in this case.

The next figure was *Cl* and *Cd* in steady and unsteady case at AR 7.9. This kind of figure will make clear understanding about WLE effect regarding aspect ratio in unsteady case.

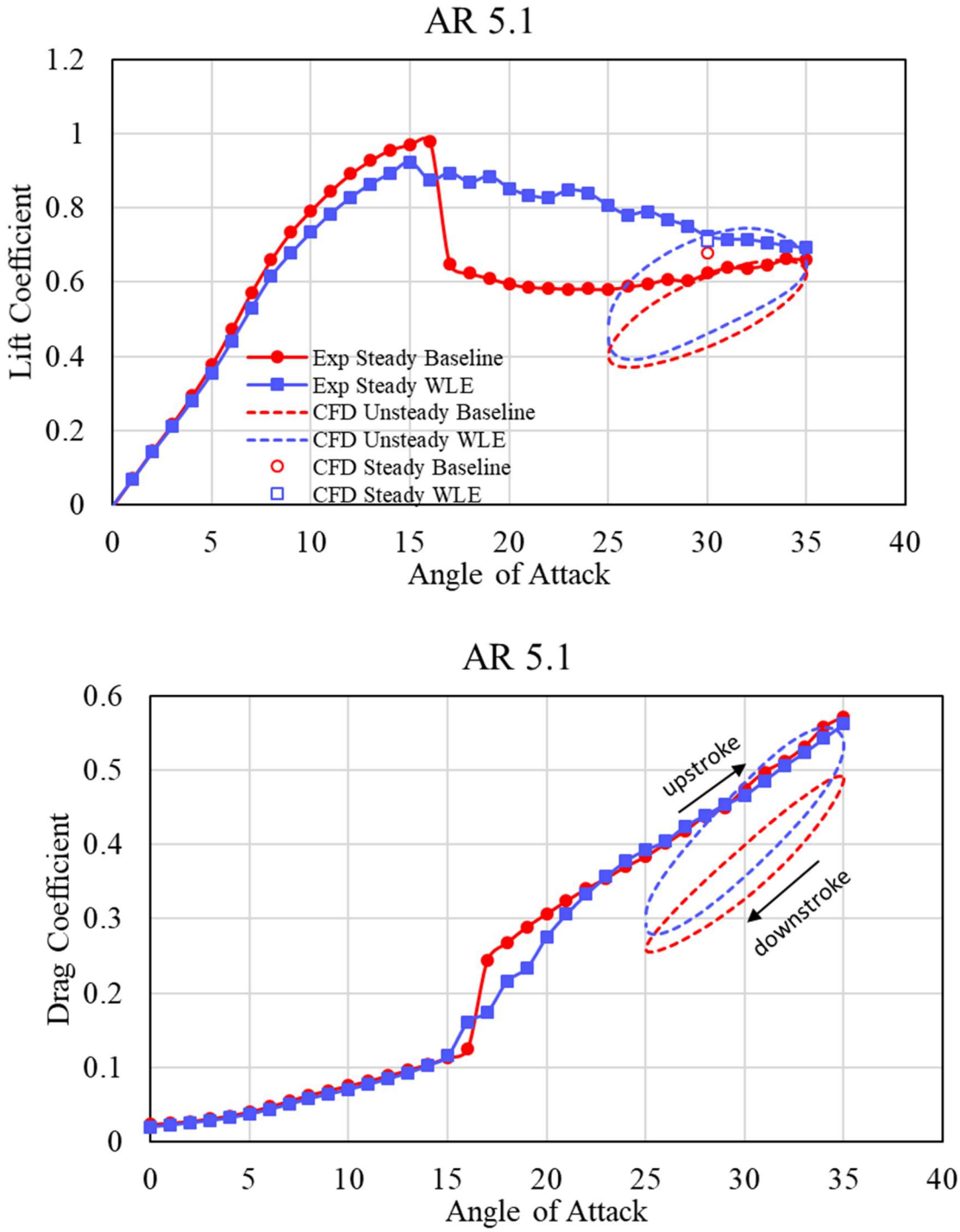

Figure 5.4 The *Cl* and *Cd* at AR 5.1 in steady and unsteady case

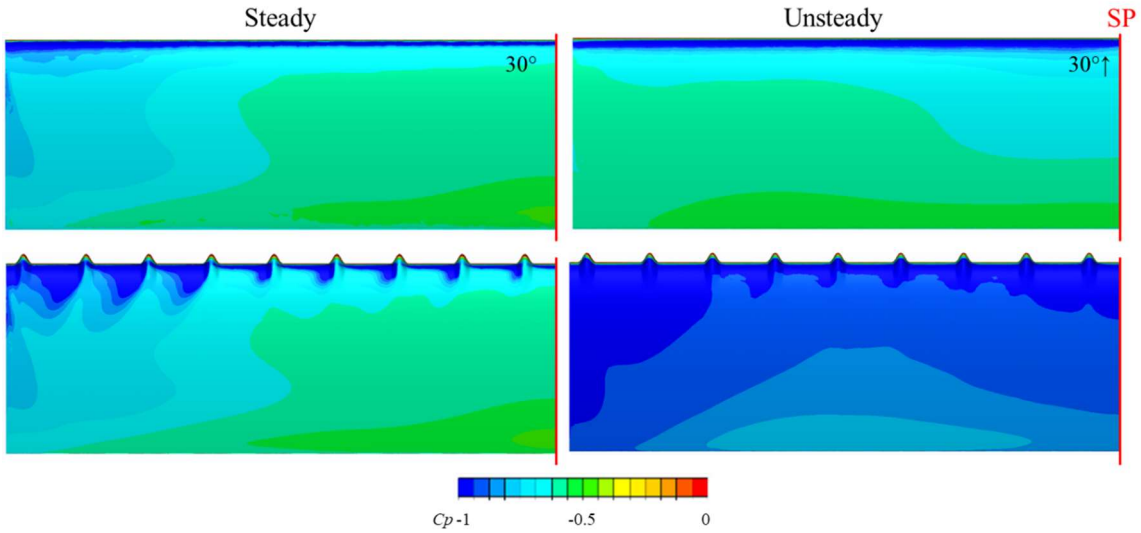

Figure 5.5 Pressure coefficient distribution of AR 5.1 in steady and unsteady case at 30°

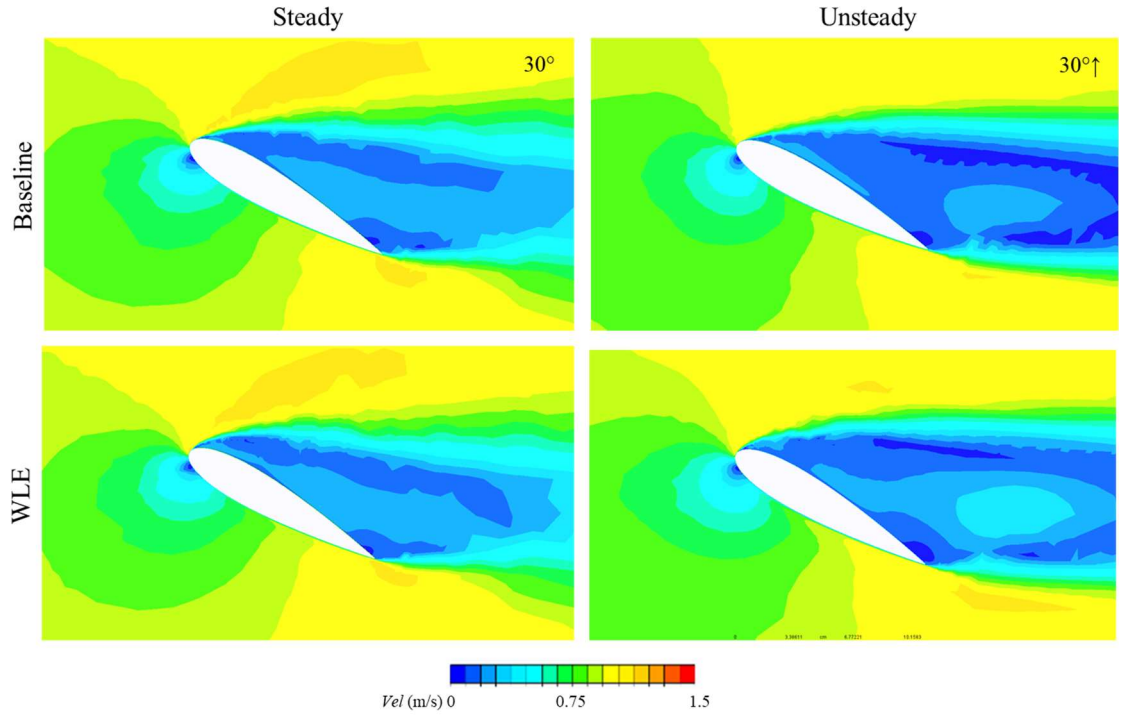

Figure 5.6 Velocity Magnitude distribution of AR 5.1 in steady and unsteady case at 30°

Figure 5.7 shows a performance of AR 7.9 in steady and unsteady motion. As mentioned before in the chapter 4, there is no experimental result in the AR 7.9. Therefore, only numerical result has been shown in these figures. In the Figure 5.7 was the *Cl* and *Cd* result for range angles 20°-35°. The steady and unsteady result shown with the straight line and dash line, respectively. An interesting fact *Cl* of AR 7.9 is in steady case at 30° has similar trend with the unsteady case during upstroke motion. This tendency also found in *Cd* in both cases. In the unsteady result, the baseline and WLE wing have similar tendencies during upstroke motion, the baseline wing is higher than the WLE wing during downstroke motion.

The flow pattern in this angle was chosen to be explored in this section as shown in the Figures 5.8-5.9. In the Figure 5.8 shows the pressure coefficient (*Cp*) on the suction surface of the wing. In the left side was the steady case results, while in the right side was unsteady case results during upstroke motion. In the pressure coefficient distribution, dominant lower pressure almost covered up the WLE wing surface during upstroke motion. It is shown with the deep color along WLE wing during upstroke motion. It means that the flow was easier to go through the wing than other cases. In the Figure 5.9 shows the velocity distribution on the mid span section. But in this case, there are no significant differences among them.

In the chapter 4 was mentioned that AR 7.9 has the best performance compared to other aspect ratio variation in steady case. Opposite in the unsteady case, the performance of AR 7.9 is not so good compared to the baseline wing.

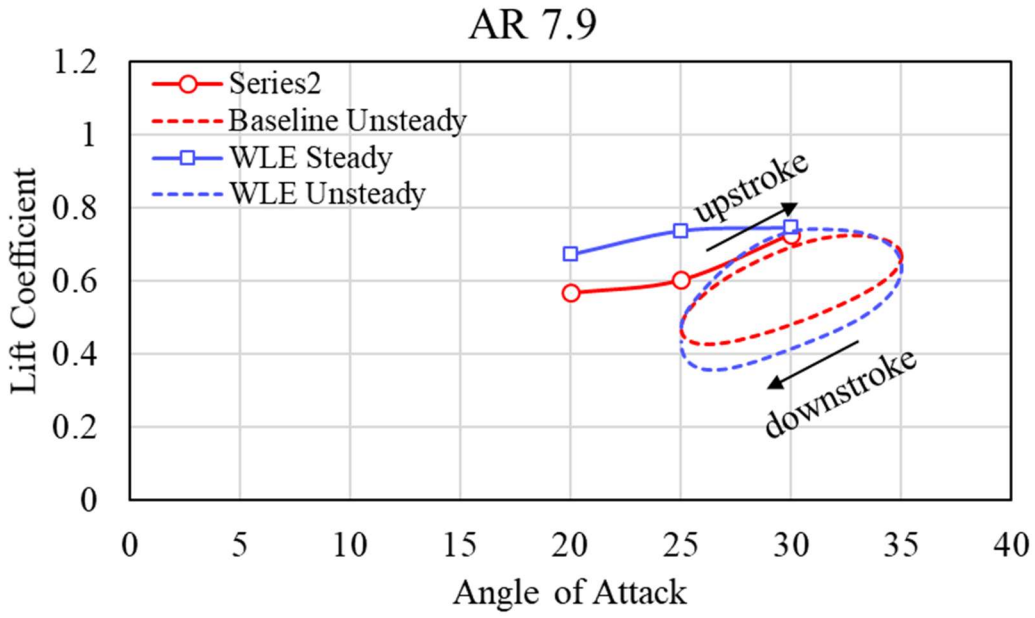

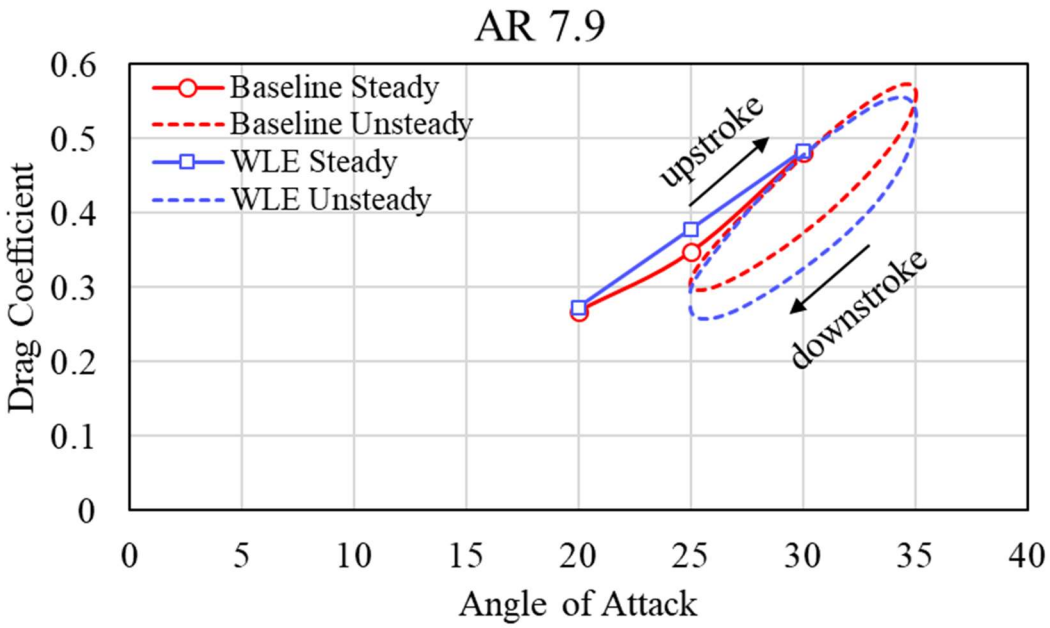

Figure 5.7 The *Cl* and *Cd* at AR 7.9 in steady and unsteady case

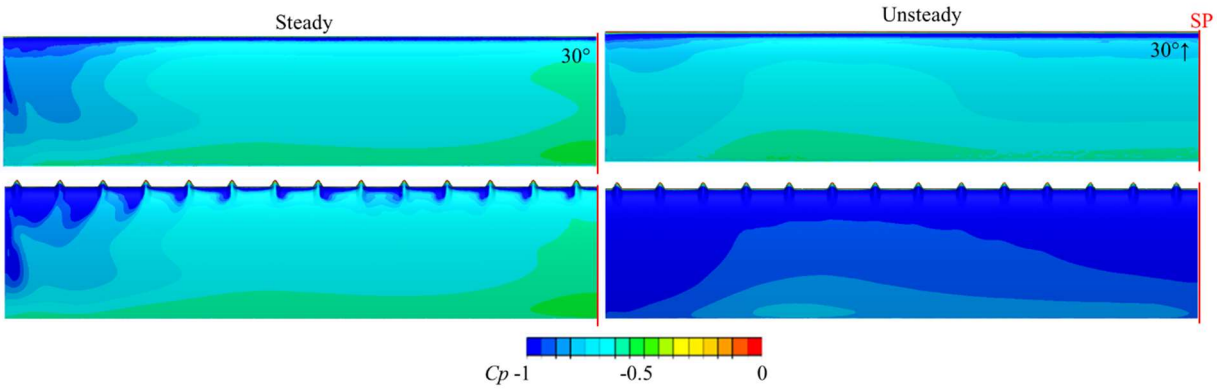

Figure 5.8 Pressure coefficient distribution of AR 7.9 in steady and unsteady case at 30°

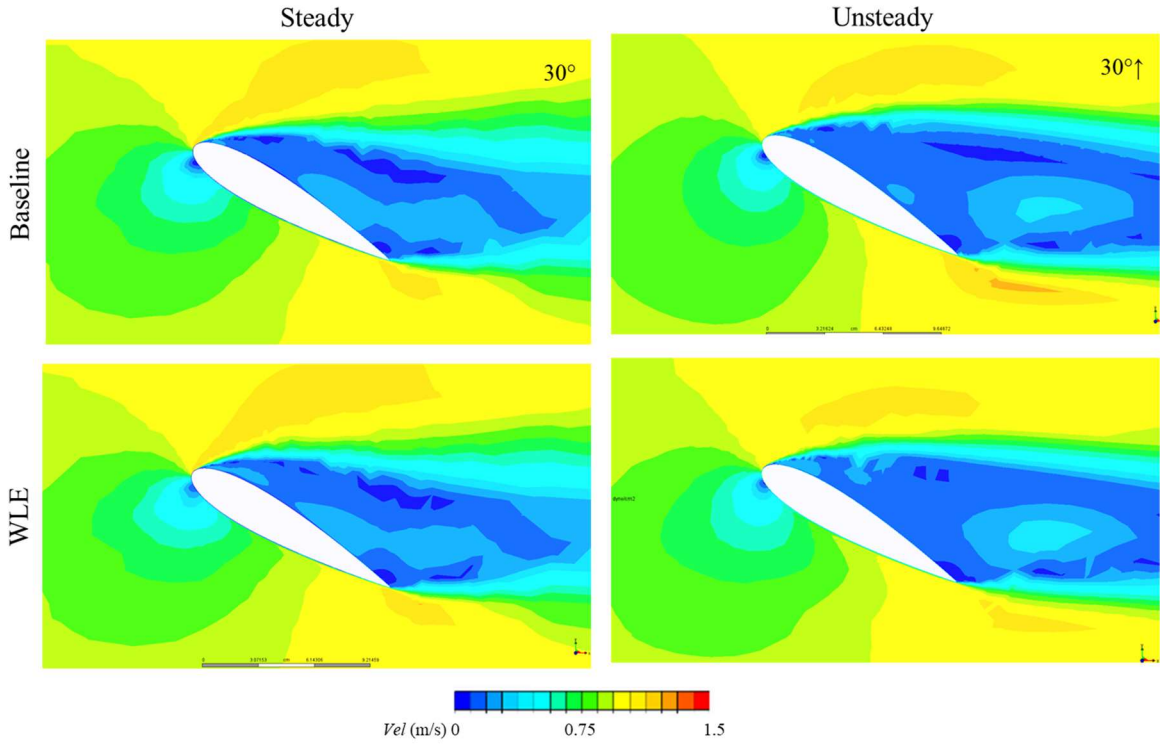

Figure 5.9 Velocity Magnitude distribution of AR 7.9 in steady and unsteady case at 30°

5.2 Summary

The WLE effect on the rectangular wing with three aspect ratios 3.9, 5.1, and 7.9 in the unsteady case has been observed. In this case, consistent results were found in the aspect ratio (AR) 3.9 and 5.1 where the WLE wing has a better performance than the baseline wing in the post-stall condition. Meanwhile, in the aspect ratio (AR) 7.9, there are no significant differences between baseline and WLE wing. A similar tendency was found with an aspect ratio (AR) 1.6 was mentioned in the previous chapter, better performance of the WLE wing was found during upstroke motion than downstroke motion.

CHAPTER 6
A COMPARISON OF RECTANGLE WING AND TAPERED WING USING WAVY LEADING EDGE

In chapter 3, the optimum aspect ratio has been analyzed among various aspect ratio series on the rectangle wing. We found that aspect ratio 7.9 has the best performance in steady case only. So, only AR 7.9 was used in this chapter. This rectangle shape of the wing is an approach of *Humpback whale* flipper. But this shape is easier to build for some applications such as fin stabilizer or wind turbine if we compare it with the flipper shape. As we knew that the flipper shape is close to the taper shape, but we do not know what the taper ratio is. As we know that the taper shape has the best performance to reduce the separation area if compared to the rectangular shape. An overview of the wing was performed in this chapter is a rectangular wing with NACA 0018 profile with the chord length (c) equals to 125 mm, and taper wing with the average of the chord length ($\bar{c}$) 128,5 mm. Three types of taper ratio (TR) were used in this chapter i.e. TR 0.1, 0.3 and 0.5. Aspect ratio of the *humpback whale* flipper varies from 3.6 to 7.7 [49]. Thus, a study about approaching the flipper shape is needed. In this chapter a comparison of rectangle and tapered wing will be discussed.

Lowest L/D ratio was found in aspect ratio 7.9 at three angles i.e. 20°, 25° and 30° on the WLE wing. From *Cl, Cd* and *L/D* ratio aspect ratio analysis, 7.9 aspect ratio has the best performance. Therefore, to approach the *Humpback whale* flipper shape, the wing is modified to taper wing. In the chapter 4 was mentioned about the effectiveness of WLE. The WLE on the taper wing only located between mid-span and the wing tip. The WLE shape was similar between rectangle and taper wing with wavelength (W) equals to 8% of c and amplitude (d) 5% of c.

6.1 Validation with Experimental Data

In the following figure is numerical validation of taper wing with the experimental results. The root chord length was 200 mm with the tip chord length was 57 mm. This make the wing has taper ratio about 0.285. The taper ratio of the wing was 7.74. This taper ratio has no big differences with the rectangle wing. The validity was employed using numerical method which has similar dimension of the experimental set-up. The validation was carried out at the angles

20°, 25° and 30° for both wing types. The validation assumed as quite good results in the Figure 6.1. Next, the mesh set-up from this validation is used for taper wing.

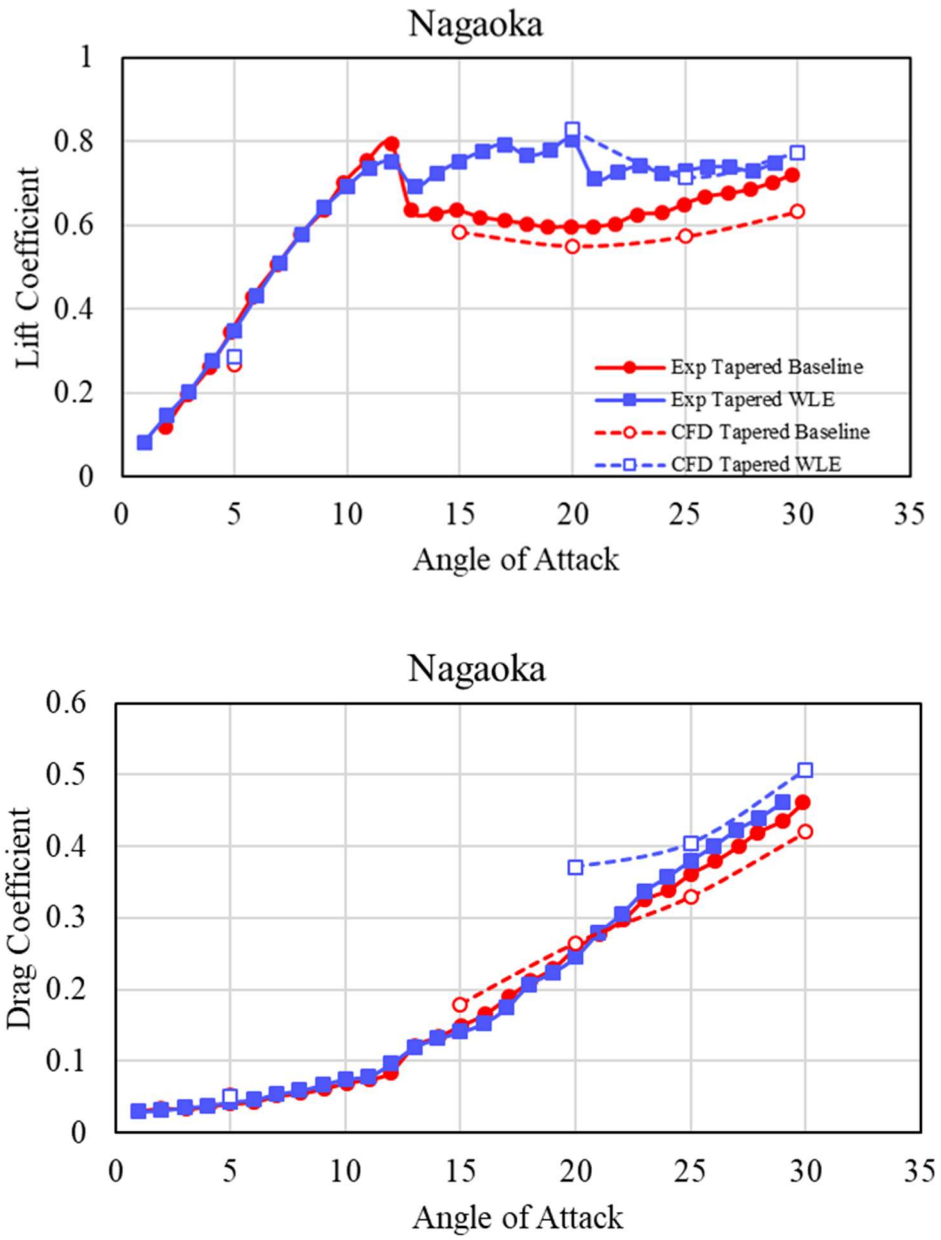

Figure 6.1 Validation with Nagaoka Experimental

6.2 Taper Ratio Variation in Steady Case

In the chapter 5 was mentioned that from *Cl, Cd* and *L/D* ratio aspect ratio analysis, 7.9 aspect ratio has the best performance. Therefore, to approach the *Humpback whale* flipper shape, the wing is modified to taper shape with 3 types of taper ratio (TR) :0.1; 0.3 and 0.5. In this section, the flow distribution will be discussed among three types of taper wing to find out the best shape of taper ratio wing. In the Figure 6.2 shows the lift coefficient at three types of taper ratio wing at the angles 20°, 25° and 30°, respectively. Regarding this figure, there is no significant differences between baseline and WLE taper ratio wing. But taper ratio 0.3 wing has the best value among them. Then, in the next section TR 0.3 wing is chosen to compare with the rectangular wing.

The next figure will explain a comparison between rectangle wing at AR 7.9 and TR 0.3 wing at the angle 20°. Effectiveness of WLEs also evaluated based total number and arrangement of WLE. The shape of WLE is same between rectangle and taper wing. From the static pressure distribution, the low pressure indicated with the deep blue colour were found at the rectangle and TR 0.3 wing. Next step is an investigation the flow distribution in the X-Y plane to find out the effectiveness of WLE in each wing shape. In the Figures 6.3 shows the pressure coefficient (*Cp*) distribution in *XY*-plane around the wing. There are 4 plane sections will be discussed where the numbering was started from the wing tip illustrated in the Figure 6.4. This comparison was set in the angle 20° only.

Refers to the Figure 6.5, in the position 1, the low pressure was found in the suction side (upper side) of the wing for all wing type. The lowest pressure coefficient indicates the deep blue region around leading edge. The taper wings have wider low pressure in *1st position* than the rectangle type. Similar result was found in the *2nd position*, the taper wings have wider low pressure than the rectangle type. In the 3rd position, wider low pressure was found in taper wings. Widest low pressure was found in TR 0.3 wing, it means the flow is easier through the wing than other wings. Strong effect of WLE was found in the 3rd position. On the other hand, on TR 0.3 wing, the lowest *Cp* distribution were wider than the rectangular wing. It indicates that the flow was easier through the wing.

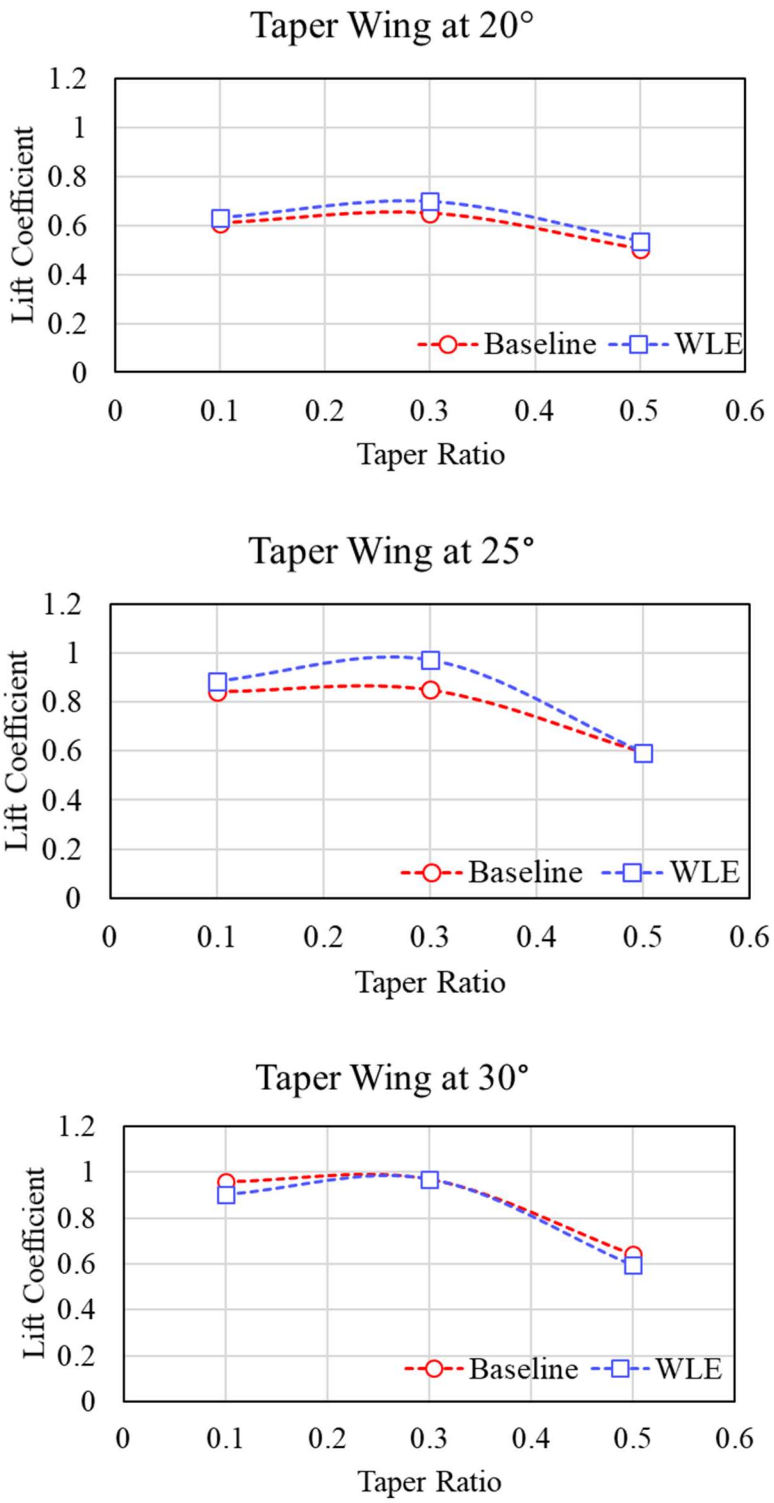

Figure 6.2 Lift coefficient each three taper ratio types

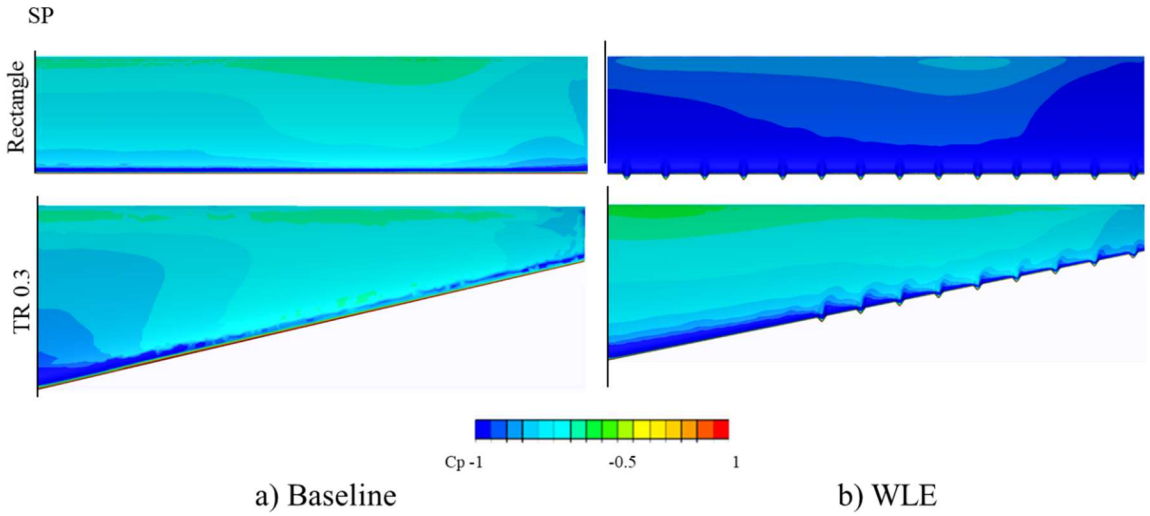

Figure 6.3 Comparison of pressure coefficient distribution at 20°

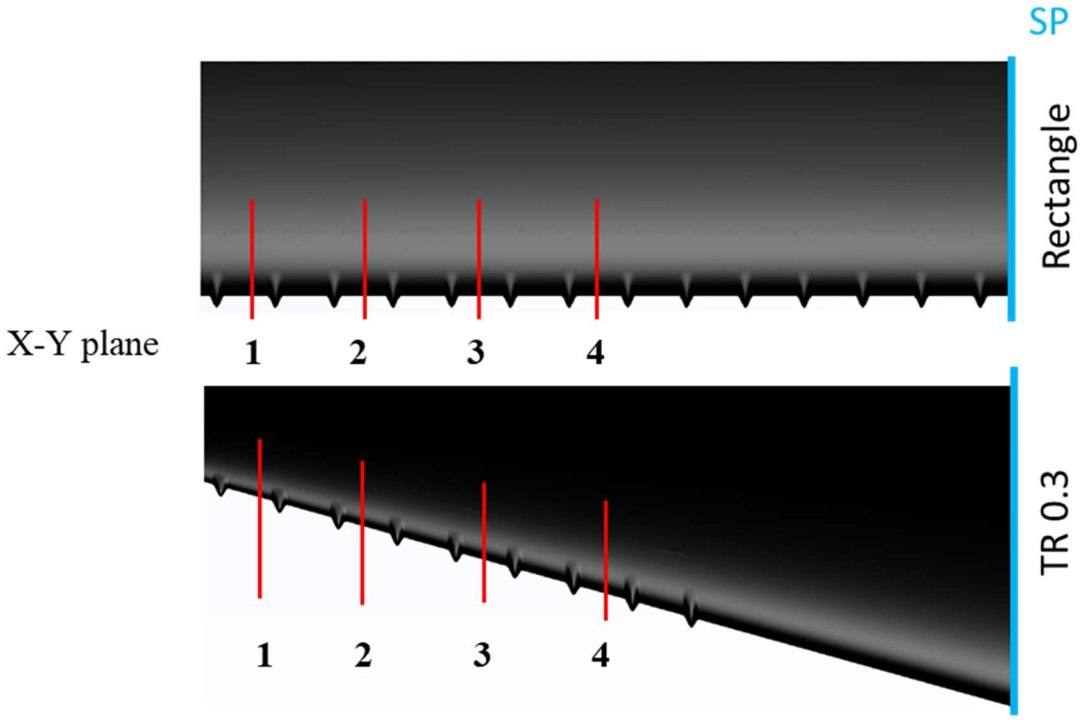

Figure 6.4 Numbering system of *XY*-plane

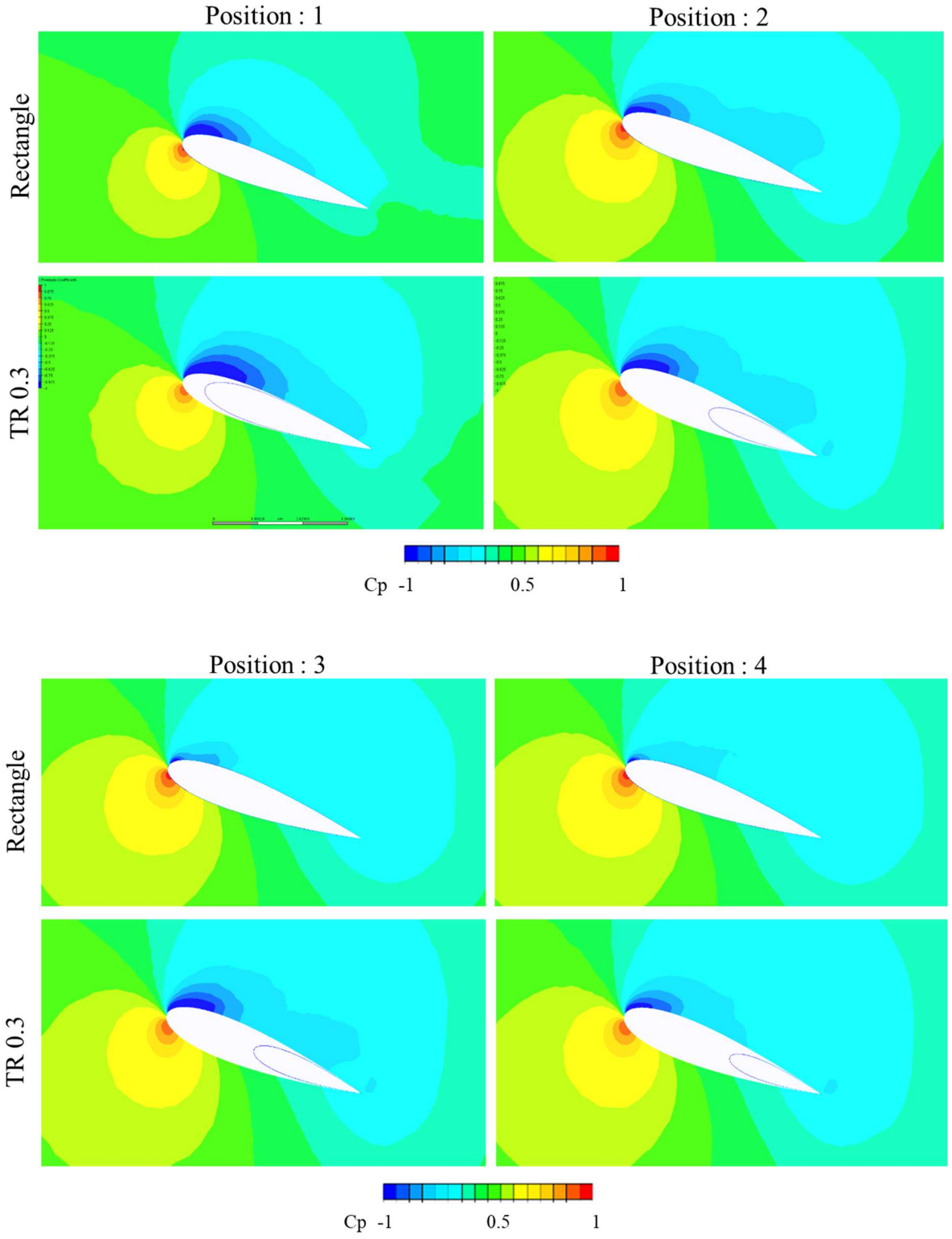

Figure 6.5 Pressure coefficient (*Cp*) distribution in each *XY*-plane section at 20°

6.3 Unsteady Taper Ratio Analysis

As previous explanation stated in the above, TR 0.3 is the best taper shape among three types of TR in steady analysis. Thus, unsteady analysis in this section only focused on TR 0.3 wing. Figure 6.6 shows a comparison unsteady case of TR 0.3 at the angles 25°-35°. Upper figure shows the *Cl* result and the bottom one is the *Cd* result. In the *Cl* comparison, seems that no significant differences between baseline and WLE wing in the Figure 6.7. The WLE wing has a little higher than the baseline wing at the angles more than 30°-35° during upstroke motion, but at the angle 30° is similar. In the *Cd* comparison, the baseline wing has higher *Cd* than the WLE wing during the upstroke motion. Then, did during the downstroke motion.

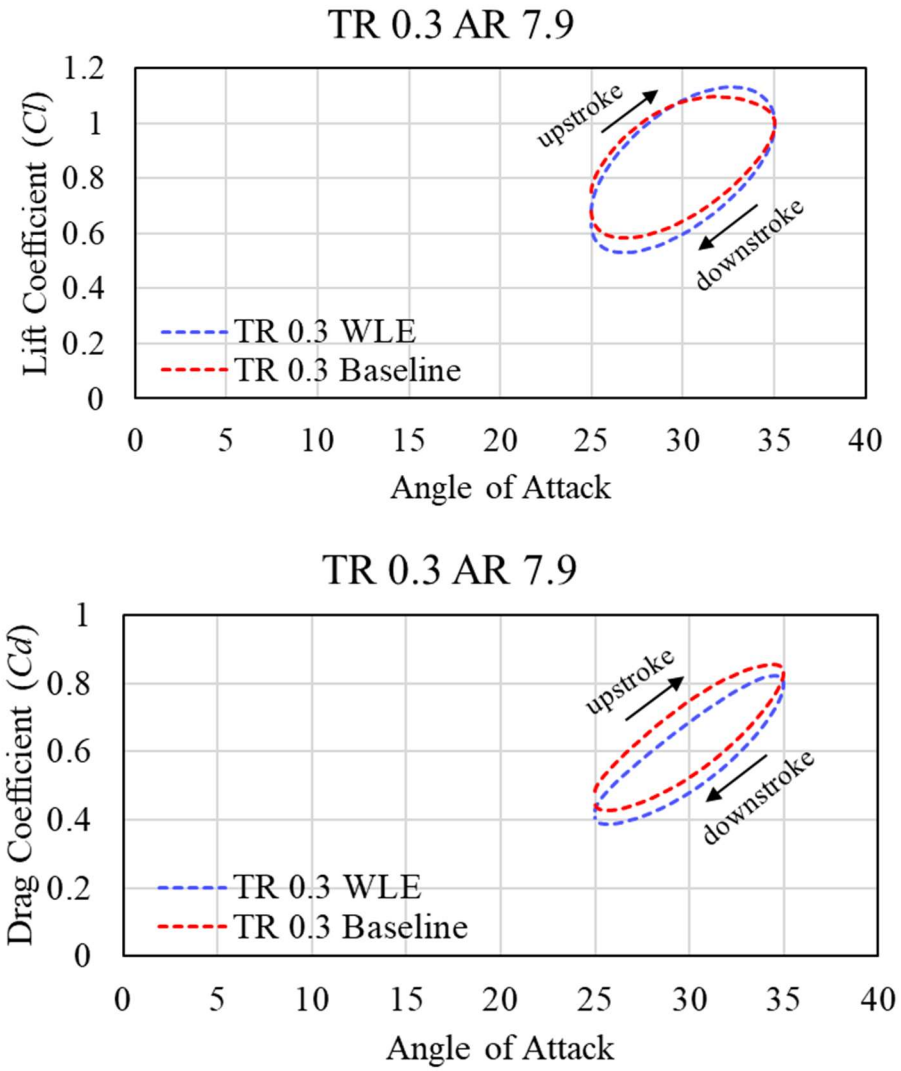

Figure 6.6 The *Cl* and *Cd* result of unsteady case of TR 0.3 wing

Next, a comparison of AR 7.9 on rectangular wing and TR 0.3 wing in unsteady case. In the following figure, only the WLE wing of TR 0.3 wing was given as comparison. In this case we are focused on the comparison of WLE wing in both wings. Figure 6.7 shows the *Cl* and *Cd* comparison between rectangular wing with AR 7.9 and taper wing TR 0.3. The WLE wing was show as blue dash line where the TR 0.3 wing was show as the green dash line. It is clearly seen that the TR 0.3 wing has higher *Cl* compared to the rectangular wing during upstroke motion or downstroke motion. This phenomenon also found in the *Cd* comparison as given in the bottom figure.

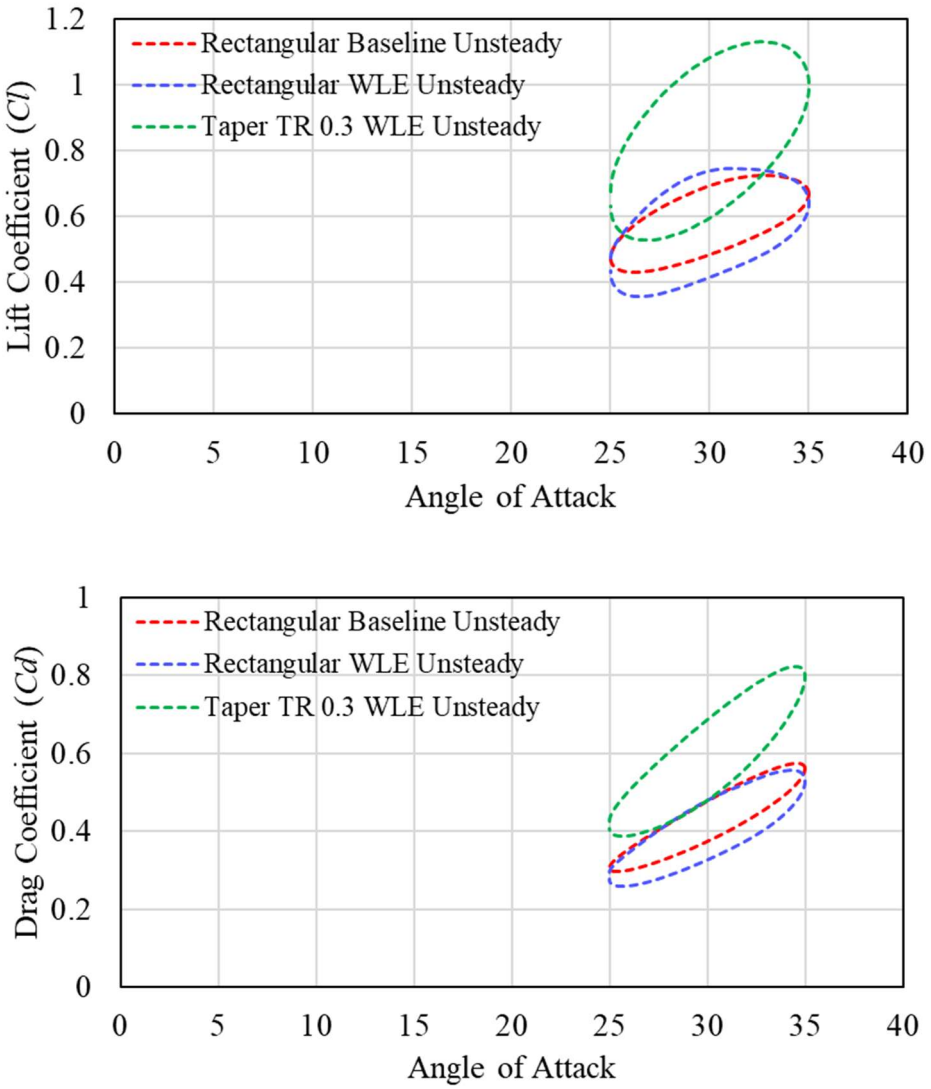

Figure 6.7 A comparison of *Cl* and *Cd* in unsteady case of rectangular AR 7.9 wing and TR 0.3 wing

To clarify the performance of both wing shape, the turbulent intensity (*TI*) was employed in this section. As comparison, the angle of attack 30° was chosen as shown in the Figures 6.8-6.9. These figures are instantaneous turbulent intensity (*TI*) at the angle of attack 30° during upstroke motion only. Figures 6.8 shows the *TI* distribution on the suction surface of the wing. In the rectangular wing, the *TI* distribution has higher value compared to the TR 0.3 wing as shown with the green area around the leading edge. This phenomenon was agreed with the pressure coefficient distribution as shown in the Figure 6.5 where the WLE on the rectangular wing has wider of low pressure along its surface.

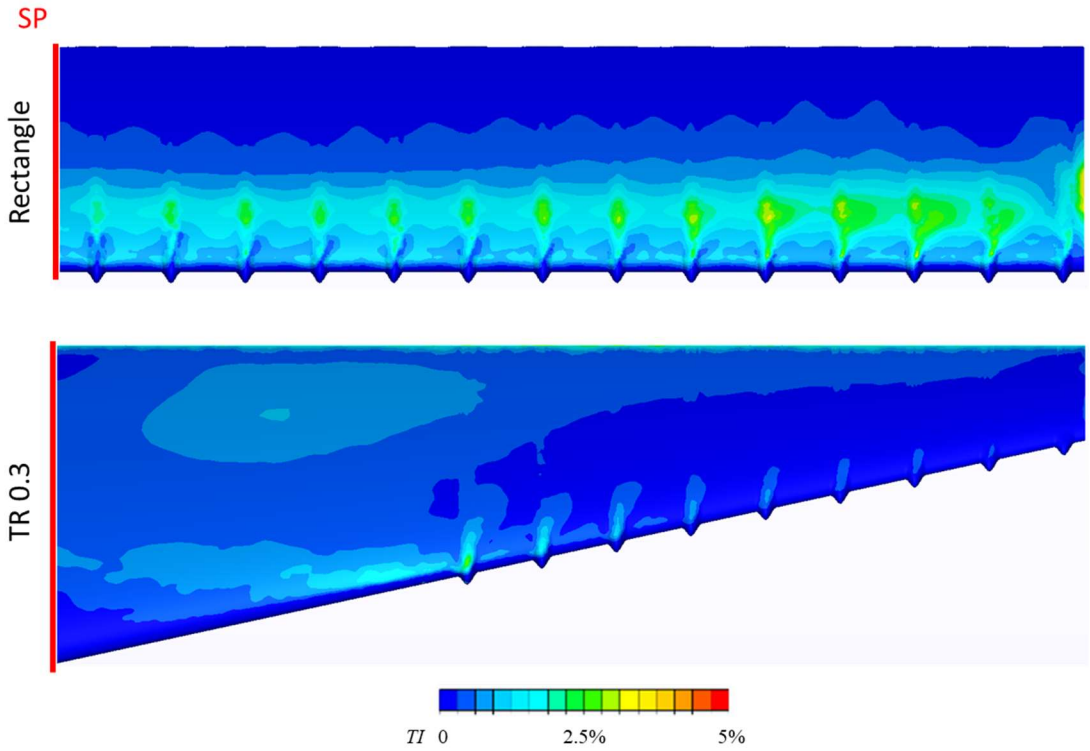

Figure 6.8 Instantaneous of *TI* distribution on the suction surface in rectangular and TR 0.3 wing

While the fact that the *Cl* distribution of TR 0.3 wing has higher value compared to the rectangular wing as shown in the Figure 6.7, the *TI* distribution has no same manner. It is interesting to find out the wake area after the flow through the wing surface. Figure 6.9 shows instantaneous of streamline distribution in the wake area at the angle 30° in perspective view. The streamline in this figure shows as the turbulent intensity where the red color indicates the higher *TI*. It can be seen that the streamline on the wake area of rectangular wing has rotating along the wing-span. But in the TR 0.3 wing, in the area close to the wing tip is not. The straight

streamline was described from leading edge through the trailing edge area. The *TI* distribution as streamline form in the wake area indicates the separation area. Then, we can say that the separation area in the TR 0.3 wing was controlled compared to the rectangular wing.

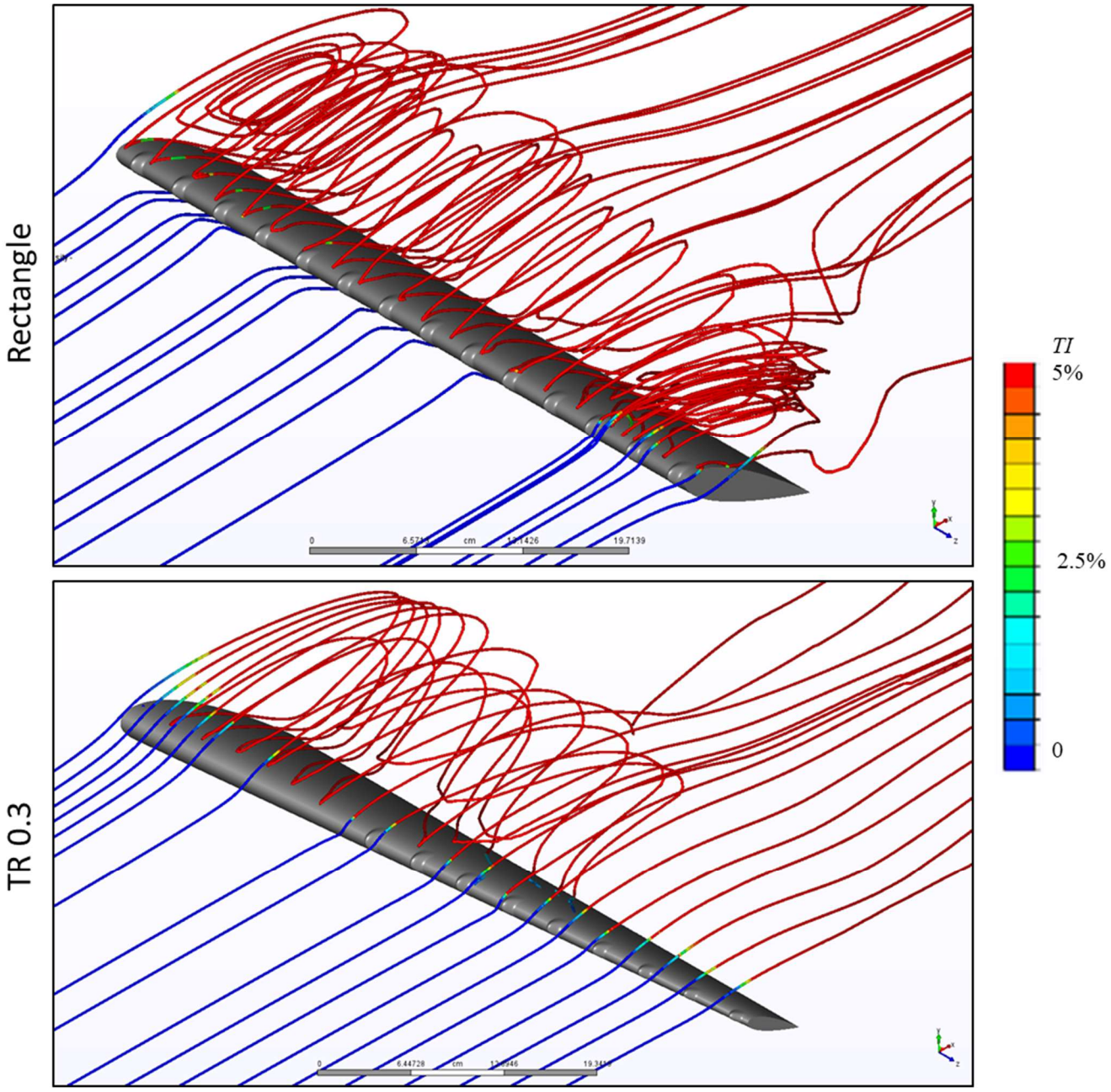

Figure 6.9 Instantaneous of *TI* as streamline distribution in rectangular and TR 0.3 wing

6.4 Summary

A comparison of the rectangular and tapered wing with aspect ratio (AR) 7.9 was employed in this chapter in steady and unsteady case. In this chapter, the WLE effect also verifies based on its location close to the symmetry plane, mid-span, and close to the wing tip area. The WLE which is located on the mid-span section to the wing tip area has the strongest effect to suppress the stall. This result is similar to the WLE effect on the rectangular wing that already mentioned in the previous chapter.

On the tapered wing, there are three types of taper ratios (TR) i.e. 0.1, 0.3, and 0.5. In steady case analysis, the taper wing with TR 0.3 has the best performance. Then, this taper ratio TR 0.3 has been used to compare with the rectangular wing at AR 7.9. Even though during unsteady motion on the rectangular wing with AR 7.9 there are no significant differences between baseline and WLE wing, the TR 0.3 wing has better performance among them. The streamlines distribution in turbulent intensity (TI) was used to see the separation phenomenon in this case. The streamlines on the wake area of the rectangular wing have rotating motion along the wing-span. But, on the TR 0.3 wing the straight streamlines were found in the mid-span to the wing tip direction. The separation area in the TR 0.3 wing was controlled compared to the rectangular wing.

CHAPTER 7
CONCLUSION

Learning from nature by inspired of humpback whale flipper which has the ingenious ability to catch their prey. Its flipper has several WLE with the form blunt and rounded shape along their leading edge. This flipper was expected to increase the performance during their ability to catch their prey faster. Therefore, the WLE was used in this research where in the beginning the rectangular wing was chosen to approach the flipper shape. The experimental and numerical methods were used to find out the WLE effect regarding the aspect ratio and the wing motion. The NACA 0018 profile was used with Reynolds number 1.4 x 10^5. The chord length of the wing was 125 mm and 250 mm, it depends on the aspect ratio (AR) variation. The WLE shape has the wavelength (W) 8% of c with the amplitude (d) equals to 5% of the c.

To understand the mechanism of fluid flow on the WLE wing, the numerical method by using Autodesk® CFD was employed in this study. As a comparison, the experimental work was given in Chapter 2. The NACA 0018 profile was used with the WLE shape with wavelength 8% and amplitude 5% of the chord length. In the beginning, the wing was used is rectangular. This study was performed in steady and unsteady case with three reduced frequencies k = 0.09, 0.12, and 0.25. To get the maximum benefit of the WLE effect, this study is varied in various aspect ratios (AR) 1.6, 3.9, 5.1, 7.9, and 9.6 in baseline and WLE wing. Besides that, to approach the humpback whale flipper shape, the wing shape was modified into the taper wing with three taper ratio (TR) variations i.e. 0.1, 0.3, and 0.5.

In Chapter 3, the WLE effect on the rectangular wing was performed in steady and unsteady case. In this chapter, only one AR 1.6 was explored. As a comparison, the vortex generator (VG) is given to make a clear understanding of the WLE effect. In a steady case, the VG wing has the same manner as the baseline wing. While the WLE wing is able to acquire the lift force after stall condition. The WLE wing has the best performance among three types of the wing. Therefore, in unsteady case only focused on the post-stall condition. Three reduced frequencies k = 0.09, 0.12, and 0.25 were given in this case to find out the WLE effect during unsteady motion. Clearly, differences between baseline and WLE wing was found in the fastest reduced frequency k = 0.25. Then, the streamlines distribution was explored around the WLE to find out the mechanism delaying the stall due to the WLE. The stream-wise vortical flow

around WLE is thought to contribute to the suppression of separation. In the present unsteady study, a similar stream-wise vortical flow is observed around the WLE during the upstroke and down-stroke motion. The twisted vortical flow observed at the upstroke motion is stronger than the down-stroke motion, which is thought to be related to the fact that the higher lift is obtained at the upstroke motion than the down-stroke motion.

To get maximum applications on the WLE effect, the various aspect ratio has been performed in this study in a rectangular wing and steady case only was discussed in Chapter IV. The best aspect ratio in this study is 7.9, which has the best lift coefficient in each angle compared to all aspect ratio. The WLE effect location also observed in this chapter. There are three sections to verify the WLE effect i.e. on the symmetry plane, mid-span, and area close to the wing tip. The WLE in the mid-span to the area close to the wing tip has the strongest effect to suppress the separation.

The WLE effect on the rectangular wing with three aspect ratios 3.9, 5.1, and 7.9 in the unsteady case has been observed in the Chapter V. In this case, consistent results were found in the aspect ratio (AR) 3.9 and 5.1 where the WLE wing has the better performance than the baseline wing in post-stall condition. Meanwhile, in the aspect ratio (AR) 7.9, there are no significant differences between baseline and WLE wing. A similar tendency was found with aspect ratio (AR) 1.6 was mentioned in the previous chapter, better performance of WLE wing was found during upstroke motion than downstroke motion.

A comparison of the rectangular and tapered wing with aspect ratio (AR) 7.9 was employed in Chapter VI in steady and unsteady case. The WLE effect also verifies based on its location close to the symmetry plane, mid-span, and close to the wing tip area. The WLE which is located on the mid-span section to the wing tip area has the strongest effect to suppress the stall. This result is similar to the WLE effect on the rectangular wing that already mentioned in the previous chapter. On the tapered wing, there are three types of taper ratios (TR) i.e. 0.1, 0.3, and 0.5. In steady case analysis, the taper wing with TR 0.3 has the best performance. Then, this taper ratio TR 0.3 has been used to compare with the rectangular wing at AR 7.9. Even though during unsteady motion on the rectangular wing with AR 7.9 there are no significant differences between baseline and WLE wing, the TR 0.3 wing has better performance among them. The streamlines distribution in turbulent intensity (TI) was used to see the separation phenomenon in this case. The streamlines on the wake area of the rectangular wing have

rotating motion along the wing-span. But, on the TR 0.3 wing, the straight streamlines were found in the mid-span to the wing tip direction. The separation area in the TR 0.3 wing was controlled compared to the rectangular wing.

It is interesting to explore the differences of rectangular and TR 0.3 wing such as the pressure losses in the wake area. Besides that, the author suggests it analysis could be applied in another wing profile to find out the best performance closest to the humpback whale shape.

REFERENCE:

[1] J. M. B. Frank E. Fish, “Hydrodynamics Design of The Humpback Whale Flipper.” Journal of Morphology 225 : 51 - 60 (1995), pp. 51–60, 1995.

[2] F. E. Fish, P. W. Weber, M. M. Murray, and L. E. Howle, “The Tubercles on Humpback Whales ’ Flippers : Application of Bio-Inspired Technology,” vol. 51, no. 1, pp. 203–213, 2011.

[3] F. E. Fish, “Biomimetics : Determining engineering opportunities from nature,” *Proc. SPIE*, vol. 7401, pp. 1–11, 2009.

[4] C. Bak, P. Fuglsang, and J. Johansen, *Wind Tunnel Tests of the NACA 63-415 and a Modified NACA 63-415 Airfoil*, vol. 1193, no. December. 2000.

[5] D. S. Miklosovic and M. M. Murray, “Experimental Evaluation of Sinusoidal Leading Edges,” *J. Aircr.*, vol. 44, no. 4, pp. 2–5, 2007.

[6] D. S. Miklosovic, M. M. Murray, L. E. Howle, and F. E. Fish, “Leading Edge Tubercles Delay Stall on Humpback Whale (Megaptera Novaeangliae) Flippers,” *Phys. Fluids*, vol. 16, no. 5, pp. 39–42, 2004.

[7] H. T. C. Pedro and M. H. Kobayashi, “Numerical Study of stall delay on humpback whale flippers,” no. January, pp. 7–10, 2008.

[8] M. L. Post, R. Decker, A. R. Sapell, and J. S. Hart, “Effect of bio-inspired sinusoidal leading-edges on wings,” *Aerosp. Sci. Technol.*, vol. 81, pp. 128–140, 2018.

[9] H. Johari, C. Henoch, D. Custodio, and A. Levshin, “Effects of Leading Edge Protuberances on Airfoil Performance,” *AIAA J.*, vol. 45, no. 11, pp. 2634–2642, 2007.

[10] K. Hansen, R. Kelso, and B. Dally, “An investigation of three-dimensional effects on the performance of tubercles at low reynolds numbers,” *17th Australas. Fluid Mech. Conf.*, no. December, pp. 1–4, 2010.

[11] K. L. H. N. Rostamzadeh, R. M. Keslo, B. B. Dally, “The Effect of Wavy Leading Edge Modifications on NACA 0021 Airfoil Characteristics,” *18th Aust. Fluid Mech. Conf.*, no. December, 2012.

[12] K. L. Hansen, R. M. Kelso, and B. B. Dally, “Performance Variations of Leading-Edge

Tubercles for Distinct Airfoil Pro fi les," *AIAA J.*, vol. 49, pp. 185–194, 2011.

[13] K. L. Hansen, N. Rostamzadeh, and R. M. Kelso, "Evolution of the streamwise vortices generated between leading edge tubercles," *J. Fluid Mech.*, vol. 788, pp. 730–766, 2016.

[14] H. Arai, Y. Doi, T. Nakashima, and H. Mutsuda, "Hydrodynamic Performance of Wing with Wavy Leading Edge," *Adv. Marit. Eng. Conf. 4th Pan Asian Assoc. Marit. Eng. Soc. Forum*, no. 2009, pp. 978–981, 2010.

[15] H. Arai, Y. Doi, T. Nakashima, and H. Mutsuda, "A Study on Stall Delay by Various Wavy Leading Edges," *J. Aero Aqua Bio-mechanisms*, vol. 1, no. 1, pp. 18–23, 2010.

[16] M. W. Lohry, D. Clifton, and L. Martinelli, "Characterization and Design of Tubercle Leading-Edge Wings," *7th Int. Coneference Comput. Fluid Dyn.*, pp. 1–11, 2012.

[17] Z. Wei, T. H. New, and Y. D. Cui, "An experimental study on flow separation control of hydrofoils with leading-edge tubercles at low Reynolds number," *Ocean Eng.*, vol. 108, pp. 336–349, 2015.

[18] D. Serson and J. R. Meneghini, "Numerical Study of Wings With Wavy Leading and Trailing Edges," *Procedia IUTAM*, vol. 14, no. 11, pp. 563–569, 2015.

[19] V. Maksoud, T. M. A and Ramsary, "THE EFFECT OF LEADING AND TRAILING EDGE PROTUBERANCES ON AEROFOIL," *HEFAT2014*, no. July, pp. 2214–2223, 2014.

[20] J. Favier, A. Pinelli, and U. Piomelli, "Control of the separated flow around an airfoil using a wavy leading edge inspired by humpback whale flippers," *Comptes Rendus Mec.*, vol. 340, no. 1–2, pp. 107–114, 2012.

[21] S. M. A. Aftab, N. A. Razak, A. S. M. Ra, and K. A. Ahmad, "Mimicking the humpback whale : An aerodynamic perspective," *Prog. Aerosp. Sci.*, vol. 84, pp. 48–69, 2016.

[22] A. Skillen, A. Revell, A. Universit, A. Pinelli, and U. Piomelli, "Investigation of Wing Stall Delay Effect Due to an Undulating Leading Edge : an LES Study," *Int. Symp. Turbul. Shear Flow Phenom.*, no. 2012, pp. 1–6, 2013.

[23] A. Skillen, A. Revell, A. Pinelli, and U. Piomelli, “Flow over a Wing with Leading-Edge Undulations,” no. October, 2014.

[24] G. Huang, Y. C. Shiah, C. Bai, and W. T. Chong, “Experimental study of the protuberance effect on the blade performance of a small horizontal axis wind turbine,” *J. Wind Eng. Ind. Aerodyn.*, vol. 147, pp. 202–211, 2015.

[25] R. P. Torro and J. W. Kim, “A large-eddy simulation on a deep-stalled aerofoil with a wavy leading edge,” *J. Fluid Mech.*, vol. 813, no. 1995, pp. 23–52, 2017.

[26] Z. Wei, J. W. A. Toh, I. H. Ibrahim, and Y. Zhang, “Aerodynamic characteristics and surface flow structures of moderate aspect-ratio leading-edge tubercled wings,” *Eur. J. Mech. / B Fluids*, vol. 75, pp. 143–152, 2019.

[27] M. Y. Javaid, M. Ovinis, F. B. M. Hashim, A. Maimun, Y. M. Ahmed, and B. Ullah, “Effect of wing form on the hydrodynamic characteristics and dynamic stability of an underwater glider,” *Int. J. Nav. Archit. Ocean Eng.*, vol. 9, no. 4, pp. 382–389, 2017.

[28] R. K. A. Choudry, M. Arjomandi, “Lift Curve Breakdown for Airfoil undergoing Dynamic Stall,” *19th Australas. Fluid Mech. Conf.*, no. December, 2014.

[29] T. A. Talay, “Introduction to the Aerodynamics of Flight,” *Sci. Tech. Inf. Off. NASA*, 1975.

[30] T. H. Go and A. Maqsood, “Effect of aspect ratio on wing rock at low Reynolds number,” *Aerosp. Sci. Technol.*, vol. 42, pp. 267–273, 2015.

[31] Z. Wei, T. H. New, L. Lian, and Y. Zhang, “Leading-edge tubercles delay fl ow separation for a tapered swept-back wing at very low Reynolds number,” *Ocean Eng.*, vol. 181, no. April, pp. 173–184, 2019.

[32] N. Ogura, “Applying Wavy Leading Edge to Tapered wing and Rudder,” *Undergrad. Final Report, Transp. Environ. Syst. Hiroshima Univ.*

[33] M. Nagaoka, “Stall Control by Wavy Leading Edge and its Application to Tapered Wing,” 2012.

[34] Y. Wang, W. Hu, and S. Zhang, “Performance of the bio-inspired leading edge protuberances on a static wing and a pitching wing,” *J. Hydrodyn.*, vol. 26, no. 6, pp.

912–920, 2014.

[35] R. P. Torro, “A Numerical Study on the Unsteady Aerodynamic Characteristics of Thick Aerofoils with Wavy Leading Edges,” 2016.

[36] G. Gaillarde, “Dynamic STall and Cavitation of Stabiliser Fins and Their Influence on the Ship Behaviour.”

[37] G. Gaillarde, “Dynamic Behaviour and Operational Limits of Stabiliser Fins,” 2002.

[38] S. Lin, Y. Lin, C. Bai, and W. Wang, “Performance analysis of vertical axis wind turbine blade with modified trailing edge through computational fl uid dynamics,” *Renew. Energy*, vol. 99, pp. 654–662, 2016.

[39] Z. Wang, Y. Wang, and M. Zhuang, “Improvement of the aerodynamic performance of vertical axis wind turbines with leading-edge serrations and helical blades using CFD and Taguchi method,” *Energy Convers. Manag.*, vol. 177, no. September, pp. 107–121, 2018.

[40] W. Shi, M. Atlar, R. Norman, S. Day, and B. Aktas, “Effect of waves on the leading-edge undulated tidal turbines,” *Renew. Energy*, vol. 131, pp. 435–447, 2019.

[41] Autodesk CFD, “Learning Guide of Autodesk CFD,” 2020. [Online]. Available: https://knowledge.autodesk.com/support/cfd/learn-e.

[42] S. Wang, D. B. Ingham, L. Ma, M. Pourkashanian, and Z. Tao, “Computers & Fluids Numerical investigations on dynamic stall of low Reynolds number flow around oscillating airfoils q,” *Comput. Fluids*, vol. 39, pp. 1529–1541, 2010.

[43] A. Buchner, M. W. Lohry, L. Martinelli, J. Soria, and A. J. Smits, “Dynamic stall in vertical axis wind turbines : Comparing experiments and computations,” *Jnl. Wind Eng. Ind. Aerodyn.*, vol. 146, pp. 163–171, 2015.

[44] A. Orlandi, M. Collu, S. Zanforlin, and A. Shires, “3D URANS analysis of a vertical axis wind turbine in skewed fl ows,” *Jnl. Wind Eng. Ind. Aerodyn.*, vol. 147, pp. 77–84, 2015.

[45] H. R. Karbasian and K. C. Kim, “Numerical investigations on flow structure and behavior of vortices in the dynamic stall of an oscillating pitching hydrofoil,” vol. 127,

no. February, pp. 200–211, 2016.

[46] S. Wang, L. Ma, D. B. Ingham, M. Pourkashanian, and Z. Tao, “Turbulence Modelling of Deep Dynamic Stall at Low Reynolds Number,” vol. II, 2010.

[47] K. Gharali and D. A. Johnson, “Dynamic stall simulation of a pitching airfoil under unsteady freestream velocity,” *J. Fluids Struct.*, vol. 42, pp. 228–244, 2013.

[48] H. Arai, Y. Doi, T. Nakashima, and H. Mutsuda, “A Study on Stall Delay by Various Wavy Leading Edges Research Fellow of the Japan Society for the Promotion of Science.”

[49] B. F. N. (editors) D. T. H. New, *Flow Control Through Bio-Inspired Leading Edge Tubercles*. 2020.

LIST OF FIGURES

Figure 1.1	Humpback Whale with tubercles on flipper leading edge	2
Figure 1.2	Benefits of vortex generator	3
Figure 1.3	Lift coefficient (*Cl*) and drag coefficient (*Cd*) for NACA 63-415 profile with VGs on the suction side measurements	4
Figure 1.4	Experimental model a) Full span model, b) Semi-span model	5
Figure 1.5	Aerodynamic characteristics of scallop flipper	6
Figure 1.6	Averaged shear stress streak-lines for $\alpha = 12.5°$	7
Figure 1.7	Vorticity magnitude distribution	7
Figure 1.8	Lift coefficient plotted against the angle of attack	10
Figure 1.9	Velocity magnitude distributions around the leading edge	11
Figure 1.10	Underwater glider of rectangular and tapered wings	16
Figure 1.11	Schematic illustration of (a) VGs, (b) EW and (c) cavity	17
Figure 1.12	Wavy leading edge on tapered wing models	18
Figure 1.13	Lift coefficient characteristics for tapered wing	19
Figure 1.14	Increase rate of lift coefficient on tapered wing	19
Figure 1.15	Schematic view of turbine blade	21
Figure 2.1	Coordinate system	25
Figure 2.2	Plane view of the rectangular wings: (a) Baseline; (b) WLE	26
Figure 2.3	Schematic view of wavy leading edge	26
Figure 2.4	Pitching motion on the wing	27
Figure 2.5	Schematic view of VG	28
Figure 2.6	Plane view of the tapered wings	29
Figure 2.7	Pivot point of rectangular wing AR 7.9 and tapered wing TR 0.3	29
Figure 2.8	Experimental set-up at AR 1.6	31
Figure 2.9	Layer thickness around the leading edge of the baseline wing	36
Figure 2.10	Meshing configuration for baseline wing	36
Figure 2.11	Layer thickness around the leading edge of the WLE wing	36
Figure 2.12	Meshing configuration for WLE wing	37
Figure 2.13	Domain simulations steady case and its boundary condition (AR 3.9)	37

Figure 2.14	Domain simulations unsteady case and its boundary condition (AR 3.9)	38
Figure 3.1	Comparison of Baseline, VG and WLE wing results at $k = 0.25$	42
Figure 3.2	Baseline and WLE wing results at $k = 0.09$	44
Figure 3.3	Baseline and WLE wing results at $k = 0.12$	45
Figure 3.4	Baseline and WLE wing results at k = 0.25	46
Figure 3.5	Comparison of *Cl* at 20° and 30° at three reduced frequencies	49
Figure 3.6	Comparison of *Cl* and *Cd* for differences meshes	52
Figure 3.7	Lift coefficient (*Cl*) of steady case at AR 1.6	52
Figure 3.8	Drag coefficient (Cd) of steady case at AR 1.6	53
Figure 3.9	Lift and drag coefficient results at $k = 0.09$	54
Figure 3.10	Lift and drag coefficient results at $k = 0.12$	55
Figure 3.11	Lift and drag coefficient results at $k = 0.25$	56
Figure 3.12	Lift and drag coefficient ratio analysis at 30°	57
Figure 3.13	Pressure coefficient (*Cp*) at α=30°, $k = 0.09$	58
Figure 3.14	Pressure coefficient (*Cp*) at α=30°, $k = 0.12$	59
Figure 3.15	Pressure coefficient (*Cp*) at α=30°, $k = 0.25$	59
Figure 3.16	Comparison of velocity distribution at $z = 0.29c$, $k = 0.09$	61
Figure 3.17	Comparison of velocity distribution at $z = 0.29$c, $k = 0.12$	62
Figure 3.18	Comparison of velocity distribution at $z = 0.29c$, $k = 0.25$	63
Figure 3.19	Comparison of velocity distribution at $z = 0.319c$, $k = 0.09$	64
Figure 3.20	Comparison of velocity distribution at $z = 0.319$c, $k = 0.12$	65
Figure 3.21	Comparison of velocity distribution at $z = 0.319c$, $k = 0.25$	66
Figure 3.22	Up-stroke streamline at 30°, $k = 0.09$	67
Figure 3.23	Down-stroke streamline at 30°, $k = 0.09$	68
Figure 3.24	Up-stroke streamline at 30°, $k = 0.12$	69
Figure 3.25	Down-stroke streamline at 30°, $k = 0.12$	70
Figure 3.26	Up-stroke streamlines at α=30°, $k = 0.25$	71
Figure 3.27	Down-stroke streamlines at α=30°, $k = 0.25$	72
Figure 4.1	Plane view of the wings	76
Figure 4.2	The ratio of L/D in AR 3.9 (experiment)	77
Figure 4.3	The ratio of L/D in AR 5.1 (experiment)	77

Figure 4.4	The ratio of L/D in AR 3.9	78
Figure 4.5	The ratio of L/D in AR 5.1	79
Figure 4.6	The ratio of L/D in AR 7.9	79
Figure 4.7	The ratio of L/D in AR 9.6	79
Figure 4.8	The ratio of L/D in both wings at $\alpha = 25°$	80
Figure 4.9	Velocity distribution of AR 3.9 at 25°	81
Figure 4.10	Streamline distribution of AR 3.9 at 25°	82
Figure 4.11	Velocity distribution of AR 5.1 at 25°	84
Figure 4.12	Streamline distribution of AR 5.1 at 25°	85
Figure 4.13	Velocity distribution of AR 7.9 at 25°	86
Figure 4.14	Streamline distribution of AR 7.9 at 25°	87
Figure 4.15	Pressure distribution, *Cp* on the upper surface of the wings	89
Figure 4.16	Comparison of *Cl* and *Cd* at the angle 20°	91
Figure 4.17	Comparison of *Cl* and *Cd* at the angle 25°	92
Figure 4.18	Comparison of *Cl* and *Cd* at the angle 30°	93
Figure 5.1	The *Cl* and *Cd* at AR 3.9 in steady and unsteady case	96
Figure 5.2	Pressure coefficient distribution of AR 3.9 in steady and unsteady case at 30°	97
Figure 5.3	Velocity Magnitude distribution of AR 3.9 in steady and unsteady case at 30°	97
Figure 5.4	The *Cl* and *Cd* at AR 5.1 in steady and unsteady case	99
Figure 5.5	Pressure coefficient distribution of AR 5.1 in steady and unsteady case at 30°	100
Figure 5.6	Velocity Magnitude distribution of AR 5.1 in steady and unsteady case at 30°	100
Figure 5.7	The *Cl* and *Cd* at AR 7.9 in steady and unsteady case	102
Figure 5.8	Pressure coefficient distribution of AR 7.9 in steady and unsteady case at 30°	103
Figure 5.9	Velocity Magnitude distribution of AR 7.9 in steady and unsteady case at 30°	103
Figure 6.1	Validation with Nagaoka Experimental	106
Figure 6.2	Lift coefficient each three taper ratio types	108

Figure 6.3	Comparison of pressure coefficient distribution at 20°	109
Figure 6.4	Numbering system of *XY*-plane	109
Figure 6.5	Pressure coefficient (*Cp*) distribution in each *XY*-plane section at 20°	110
Figure 6.6	The *Cl* and *Cd* result of unsteady case of TR 0.3 wing	111
Figure 6.7	A comparison of *Cl* and *Cd* in unsteady case of rectangular AR 7.9 wing and TR 0.3 wing	112
Figure 6.8	Instantaneous of *TI* distribution on the suction surface in rectangular and TR 0.3 wing	113
Figure 6.9	Instantaneous of *TI* as streamline distribution in rectangular and TR 0.3 wing	114